# Chemical Interactions of Air Pollutants:

# Air Pollutant Control and Sensing Applications

by

Tingting Gao

A Dissertation Presented in Partial Fulfillment
of the Requirements for the Degree
Doctor of Philosophy

Approved July 2012 by the
Graduate Supervisory Committee:

Jean Andino, Chair
Erica Forzani
Edward Kavazanjian

ARIZONA STATE UNIVERSITY

December 2012

ABSTRACT

Volatile Organic Compounds (VOCs) are central to atmospheric chemistry and have significant impacts on the environment. The reaction of oxygenated VOCs with OH radicals was first studied to understand the fate of oxygenated VOCs. The rate constants of the gas-phase reaction of OH radicals with *trans*-2-hexenal, *trans*-2-octenal, and *tran*-2 nonenal were determined using the relative rate technique. Then the interactions between VOCs and ionic liquid surfaces were studied. The goal was to find a material to selectively detect alcohol compounds. Computational chemistry calculations were performed to investigate the interactions of ionic liquids with different classes of VOCs. The thermodynamic data suggest that 1-butyl-3-methylimindazolium chloride ($C_4$mimCl) preferentially interacts with alcohols as compared to other classes of VOCs. Fourier transform infrared spectroscopy was used to probe the ionic liquid surface before and after exposure to the VOCs that were tested. New spectral features were detected after exposure of $C_4$mimCl to various alcohols and a VOC mixture with an alcohol in it. The new features are characteristic of the alcohols tested. No new IR features were detected after exposure of the $C_4$mimCl to the aldehyde, ketone, alkane, alkene, alkyne or aromatic compounds. The experimental results demonstrated that $C_4$mimCl is selective to alcohols, even in complex mixtures. The kinetic study of the association and dissociation of alcohols with $C_4$minCl surfaces was performed. The findings in this work provide information for future gas-phase alcohol sensor design.

$CO_2$ is a major contributor to global warming. An ionic liquid functionalized reduced graphite oxide (IL-RGO)/ $TiO_2$ nanocomposite was synthesized and used to reduce $CO_2$ to a hydrocarbon in the presence of $H_2O$ vapor. The SEM image revealed that IL-RGO/$TiO_2$ contained separated reduced graphite oxide flakes with $TiO_2$ nanoparticles. Diffuse Reflectance Infrared Fourier Transform Spectroscopy was used to study the conversion of $CO_2$ and $H_2O$ vapor over the IL-RGO/$TiO_2$ catalyst. Under UV-Vis irradiation, $CH_4$ was found to form after just 40 seconds of irradiation. The concentration of $CH_4$ continuously increased under longer irradiation time. This research is particularly important since it seems to suggest the direct, selective formation of $CH_4$ as opposed to CO.

ACKNOWLEDGEMENTS

First and foremost, I would like to acknowledge my advisor and committee chair, Dr. Jean M. Andino, for her guidance and mentorship. I would like to express my gratitude to her support on both a professional and a personal level. Next, I want to thank my committee members, Dr. Erica Forzani, and Dr. Edward Kavazanjian. I would like to thank past and present members of Dr. Andino research laboratory, including Eulalia Siu, Joel Francis, Monique Rodriguez, Selisa Rollins, Megan Moloney, and undergraduate students Alejandro Castañeda, Zachariah Berkson, Akezhi Samuel Jo-Madugu, and Carlos Rivera for their supports. I would also like to express my gratitude to Fred Pena, David Wright, Timothy Karcher, Emmanuel Soignard, Sisouk Phrasavath, and the faculty members from both Environmental and Chemical Engineering Programs at Arizona State University for their help in my research and course work over the years. I gratefully acknowledge access to the shared facilities at the LeRoy Eyring Center for Solid State Science at Arizona State University for some of the material characterizations. I also want to thank Dr. Raul Alvarez-Idaboy from Universidad Nacional Autonoma de Mexico for his help in part of the computational study. My deepest appreciation goes to my friends and family who have been extremely supportive through my PhD study. In particular, I would like to thank my parents, Liying Yang and Fuqiang Gao for their unconditional love and support.

TABLE OF CONTENTS

CHAPTER Page

CHAPTER Page

LIST OF TABLES

LIST OF FIGURES

Figure Page

Figure Page

Figure Page

# CHAPTER 1

# INTRODUCTION

The atmosphere consists of complex components. The major pollutants in the environment include volatile organic compounds (VOCs), carbon dioxide ($CO_2$), and nitrogen oxides ($NO_x$). In this dissertation, new materials for sensing VOCs and removal of $CO_2$ are studied.

## 1.1 Volatile Organic Compounds

### 1.1.1 Problem Statement

Volatile organic compounds (VOCs) are organic chemical compounds that have high enough vapor pressures under normal conditions to significantly vaporize and enter the atmosphere. VOCs are central to atmospheric chemistry from the urban to global scale, and they have significant impacts on the atmosphere and climate. The oxidation of VOCs in the presence of $NO_x$ (NO and $NO_2$) and sunlight can form ozone, which is toxic to human and plants[1]. Ozone is a major air quality problem in cities and larger areas [2 3].

Besides their contribution to ozone production, VOCs are strongly linked with atmospheric aerosol formation[4-6]. Blue hazes and reduced visibility over forests are the result of enhanced scattering of blue light by particles that are similar in size to the wavelength of light[7]. These particles can be produced from gaseous organic precursors that condense from the gas phase to form aerosols. Oxygenated VOCs with low vapor pressures are favored in aerosol formation. The photochemical products of biogenic emissions of VOCs are one important source of those oxygenated compounds. For example, methacrolein, methyl vinyl

ketone and formaldehyde are the products of isoprene[8], and pinic and norpinic acids are the products of terpene photoreactions[9, 10]. The aerosols from the condensation of low vapor pressure oxygenated species produced from the oxidation of VOCs may further serve as nuclei and grow in size via coagulation with other particles and later condensation of other organic species onto the surfaces[11, 12]. The hydrophilic and light scattering properties of particles can be affected by the condensation of organic compounds or through oxidation processes. In the polluted environment, the uptake of organic gases onto soot particles is found to change the reflectivity of particles, making light absorbing soot particle more reflective. On the other hand, the uptake of organic gas onto reflective ammonium sulfate particles makes the particles darker, and hence more light absorbing[13]. Therefore, VOCs play a critical role in the aerosol albedo, and have an important effect on global climate change.

In addition to the impact of VOCs on the atmosphere and climate, the VOCs present in indoor environments are very important to human health. The US Environmental Protection Agency (EPA) reports that the levels of several VOCs are, on average, 2 to 5 times higher indoors as compared to outdoors[14]. The key signs or symptoms associated with exposure to VOCs include nose and throat discomfort, headache, skin allergy, nausea, fatigue, and dizziness[14]. Therefore, the detection and control of indoor VOCs are critical for human health.

### 1.1.2 Sources of VOCs

Almost everything we do in daily life leads to the ambient release of organic compounds. Some examples include driving a car[15], making a fire[16], cooking[17], painting a house[18], and cutting the grass[19, 20]. These activities result in the emission of organic compounds such as alcohols, alkanes, alkenes, aromatics, carbonyls, esters, and ethers. VOCs that are emitted from human activities are called anthropogenic VOCs. The U.S. National Acid Precipitation Assessment Program (NAPAP) inventory of anthropogenic VOC emissions included about 600 different compounds[21]. The major sources of anthropogenic emissions of nonmethane VOCs are fuel production and distribution as well as fuel consumption[22]. The fuel production and distribution sources include the production of petroleum and natural gas, oil refining and gasoline distribution[22]. The fuel consumption source includes the combustion of materials (e.g. coal, wood, crop residues, and waste), road transport, fuel consumption from the chemical industry, and solvent usage[22]. The estimated global anthropogenic emission of nonmethane VOCs in 1992 was 110 Tg per year[22, 23].

Biogenic VOCs (BVOCs) are the VOCs emitted from woods, crops, shrub, ocean and other biological sources. The Earth's vegetation naturally releases huge amounts of organic gases into the air. Guenther *et al.*[24] estimated the total biogenic VOC emissions on the global scale to be 1150 Tg per year in 1995. The largest biogenic emission is thought to be isoprene, followed by monoterpenes and oxygenated compounds. Therefore, on a global scale, biogenic VOC emissions far exceed those of anthropogenic hydrocarbon. The natural

emissions of VOCs from trees or other vegetation could have a significant effect on the chemistry of the earth's atmosphere[25]. Numerous studies have been performed to investigate BVOCs. These studies include emission rate studies of BVOCs[19, 20, 24, 26-47], as well as kinetic[48-57] and product[48, 54, 58-65] studies of the reactions of BVOCs with species in the atmosphere.

### 1.1.3 The Fates of VOCs

After VOCs are emitted from either anthropogenic or biogenic sources into the atmosphere, they experience one or more removal processes, including gas-phase reaction with hydroxyl radicals (OH radicals), nitrate radicals ($NO_3$ radicals) and ozone, and wet or dry deposition. Among all the removal processes, the most important removal process is chemical oxidation in the gas phase by the OH radical[53, 66].

The importance of OH radicals derives from both its high reactivity and its relatively high concentration. The concentration of OH radicals is on the order of $10^6$ molecules/$cm^3$ during daylight hours[67]. If OH radicals simply react with other species without regeneration, its concentration is expected to be very low. However, OH radicals are generated in catalytic cycles when reacting with other species. The important OH production routes include photolysis of ozone, photolysis of nitrous acid, and reaction of $HO_2$ radicals with NO[67].

Hydroxyl radicals are able to react with most VOC species in the atmosphere. Hydroxyl radicals react with different kinds of VOCs, including alkanes, alkenes, aromatics, aldehydes, ketones, unsaturated carbonyls, ethers, alcohols and acids[67]. As mentioned previously, the OH reaction with VOCs may

lead to ozone formation and secondary organic aerosol formation. Therefore, it is essential to understand OH reactions with VOCs. The reaction between OH radicals with unsaturated aldehydes, which is studied in this work, mainly proceeds via H atom abstraction from the –CHO group and OH addition to the double bond[67].

Modeling is an excellent tool to help better understand and predict the transport and fate of organic compounds in the atmosphere. Due to the significant role of VOCs in the reaction cycles in the atmosphere, a variety of numerical models are available today to simulate the chemistry and transport of VOCs. The major inputs of air quality models include (a) emission inventories that describe the primary emissions of VOCs from each specific source, (b) the oxidation chemistry of VOCs including the kinetics and products, and (c) other significant loss processes such as dry deposition and wet deposition for certain species[68]. Therefore, to properly establish the models, it is very important to have accurate kinetic data and to understand the oxidation mechanisms of the VOCs. In the past, numerous studies have been performed to obtain the rate constants [48-51, 56, 57, 59, 69-110] and mechanisms[48, 52-54, 58, 63, 66, 75-78, 85-87, 90-94, 100, 101, 111-139] for OH radical reactions with various VOCs. In chapter 2, a study of the rate constants of the reaction of OH radicals with a series of biogenic unsaturated aldehydes is presented. These constants are valuable inputs for atmospheric chemistry models.

### 1.1.4 VOCs in the Indoor Environment

Indoor air quality is especially important since people today generally spend more than 80% of their time in an indoor environment such as a home,

office, car or shopping center[140]. Major indoor air pollutants include nitrogen oxides ($NO_x$), carbon oxides (CO and $CO_2$), VOCs, and particulates. The emission of VOCs from building materials has been recognized as the largest source of indoor air pollutants[140]. Many VOCs are known to be toxic and considered to be carcinogenic, mutagenic, or teratogenic[140]. These VOCs have a close relation with sick building syndrome, which is the term used by occupants to describe the symptoms of reduced comfort or health[140].

A number of studies have been carried out to measure the indoor air concentrations of VOCs [141]. The mean concentration of each VOC in established buildings generally ranges from 5 to 50 $\mu g/m^3$ [141]. There are a variety of indoor VOC sources. The VOC emission from building material is the largest indoor VOC source[142]. The contribution from the outdoors may be important via leakages and makeup air in ventilation systems[142]. Other indoor VOC sources include combustion by-products, cooking, office equipment, household cleaning products, etc[142].

Microbial VOCs (MVOCs) that are present in indoor air may be an additional factor that might contribute to sick building syndrome[143]. Allergies and asthma may be caused by the spores of molds[143]. MVOCs have attracted increased interest[143-159]. MVOCs are produced by microorganisms when the microorganisms are growing on building materials that have been subjected to moisture. Odorous MVOCs are often the first sign of a microbial attack on different materials[160]. Thus, MVOC detection has been used as a tool to diagnose the presence or absence of molds on different materials[161, 162]. A summary of the

MVOCs that were determined in previous studies to be released from mold that was grown on different building materials appears in Table 1.1. Bjurman *et al*[145] and Wilkins *et al*[163] suggested that MVOCs can be used as a tracer of suspected microbial contamination in buildings where the occupants complain of poor indoor air quality and building related symptoms.

There are many challenges in using MVOCs as an indicator of mold generation in buildings. First, there is no single specific MVOC that is commonly identified as emanating from all building materials. However, a series of alcohols were identified in MVOCs emissions from the surfaces of all building materials that were previously studied (see Table 1.1). In particular, 3-methyl-1-butanol, 1-pentanol, 1-hexanol, and 1-octen-3-ol were the main VOCs produced by mold that grew on the building materials. Therefore, identifying a series of alcohols may be an option for the specific detection of mold. Moreover, the MVOC emissions pattern is different during different mold growth phases. The alcohol compound, 3-methyl-1-butanol, was found to be emitted during the earliest growth phase of mold[145]. Thus, targeting 3-methyl-1-butanol may be useful as an indicator for early mold formation, thus enabling early detection and remediation of mold-infested indoor environments.

Despite being able to identify specific MVOCs emanating from mold-infested surfaces, other sources may exist for these compounds in indoor environments. Pasanen *et al*[153] studied the levels of MVOCs in a number of clean rooms and mold contaminated rooms. From their data, the concentrations of the alcohols identified as MVOCs, including 2-methyl-1-propanol, 3-methyl-1-

butanol, 3-methyl-2-butanol, 1-pentanol, 1-hexanol and 1-octen-3-ol, in the contaminated rooms were 8%-66% higher than those in the clean rooms. In addition, the total concentration of all alcohols in the contaminated rooms was 4%-42% higher than the concentration in rooms without mold. Thus, the change in alcohol concentration from the background may provide an opportunity to use alcohols as an indicator of mold.

The last challenge in using MVOCs as indicators of mold is the emission rate. A previous study determined that the amount (micrograms) of MVOC emitted per hour per square meter of surface growth medium is relatively low [143]. Therefore, in order to use MVOCs as an indicator of mold growth, highly sensitive and selective materials are needed for the detection.

Table 1.1. MVOCs Produced from Cultures Grown on Building Materials

| MVOCs | Pine wood [165] | Pine wood [143] | Particle board [165] | Gypsum Board [165] | Gypsum board [143] | Wallpaper-gypsum board-plastic film[164] | Clipboard-glass wool[164] | Ceramic tile[164] | Spruce wood [143] | Ingrained wall paper[143] |
|---|---|---|---|---|---|---|---|---|---|---|
| Hydrocarbons | | | | | | | | | | |
| 1-hexene | X | | X | | | | | | | |
| 1-methyl-4-(1--methylthyl) benzene | | | | X | | | | | | |
| 1-octene | | | X | | | | | | | |
| 1,2,4,4-tetramethylcyclopentene | | | X | | | | | | | |
| 2-methyl-1,3-butadiene (isoprene) | | | X | | | | | | | |
| Hexane | | | X | | | | | | | |
| Heptane | | | X | | | | | | | |
| Nonane | | | X | | | | | | | |
| Octane | | | X | | | | | | | |
| styrene | | | X | | | | | | | |
| Alcohols | | | | | | | | | | |
| 1-heptanol | X | | | | | | | | | |
| 1-hexanol | X | | X | | | X | X | X | | |
| 1-octen-3-ol | X | | | X | X | X | X | X | | X |
| 2-pentanol | | X | | | | | | | X | X |
| 1-pentanol | | | | X | | X | X | X | | |

Table 1.1. MVOCs Produced from Cultures Grown on Building Materials (Continued)

| MVOCs | Pine wood [165] | Pine wood [143] | Particle board [165] | Gypsum Board [165] | Gypsum board [143] | Wallpaper-gypsum board-plastic film[164] | Clipboard-glass wool[164] | Ceramic tile[164] | Spruce wood [143] | Ingrained wall paper[143] |
|---|---|---|---|---|---|---|---|---|---|---|
| 2-heptanol | X | | | | | | | | | |
| 2-methyl-1-butanol | X | X | | X | | | | | X | X |
| 2-methyl-1-propanol | X | | | X | | X | | | | |
| 2-methyl-3-buten-2-ol | X | | X | | | | | | | |
| 3-methyl-2-buten-1-ol | X | | | | | | | | | |
| 3-methyl-2-butanol | | | | | X | X | | X | | X |
| 3-methyl-1-butanol | X | | | X | X | X | X | X | | X |
| 3-octene-2-ol | | | | | X | | | | X | X |
| 3-octenol | X | | | | | | | | X | |
| 2-ethyl-1-hexanol | | X | | | X | | | | X | X |
| 4-methyl-1,3-cyclohexen-1-ol | X | | | X | | | | | X | X |
| Aldehyde | | | | | | | | | | |
| Formaldehyde | | | | | | | X | X | X | |
| Acetaldehyde | | | | | | | X | X | X | |
| Acrolein | | | | | | | X | X | | |
| Propana | | | | | | | X | X | | |
| Butanal | | | | | | | X | X | X | |

Table 1.1. MVOCs Produced from Cultures Grown on Building Materials (Continued)

| MVOCs | Pine wood [165] | Pine wood [143] | Particle board [165] | Gypsum Board [165] | Gypsum board [143] | Wallpaper-gypsum board-plastic film[164] | Clipboard-glass wool[164] | Ceramic tile[164] | Spruce wood [143] | Ingrained wall paper[143] |
|---|---|---|---|---|---|---|---|---|---|---|
| pentanal | | | | | | X | X | X | | |
| Hexanal | | | | | | X | X | X | | |
| Heptanal | | | | | | X | X | X | | |
| Octanal | | | | | | X | X | X | | |
| Nonanal | | | | | | X | X | X | | |
| decanal | | | | | | X | | | | |
| 2-butyl-2-octenal | | | | X | | | | | | |
| Ketones | | | | | | | | | | |
| 2-butanone | X | | X | | | X | X | X | | |
| 2-heptanone | X | | X | | | X | X | X | | |
| 2-hexanone | X | | X | | | | X | X | | |
| 2-methyl-1,5-cyclohexanone | X | | | | | | | | | |
| 2-nonanone | X | | | | | | | | | |
| 2-octanone | X | | | X | | | | | | |
| 2-pentanone | X | | X | | | | | | | |
| 2,6,6-trimethylbicycloheptan-3-one | | | X | | | | | | | |
| 3-methyl-2-pentanone | X | | | | | | X | X | | |

Table 1.1. MVOCs Produced from Cultures Grown on Building Materials (Continued)

| **MVOCs** | **Pine wood** [165] | **Pine wood** [143] | **Particle board** [165] | **Gypsum Board** [165] | **Gypsum board** [143] | **Wallpaper-gypsum board-plastic film**[164] | **Clipboard-glass wool**[164] | **Ceramic tile**[164] | **Spruce wood** [143] | **Ingrained wall paper**[143] |
|---|---|---|---|---|---|---|---|---|---|---|
| 3-octanone | X | | | | X | X | X | | | X |
| 4-methyl-2-hexanone | X | | | | | | | | | |
| Acetone | | | | X | | X | X | X | | |
| Cyclopentanone | X | | | | | | | | | |
| Pulegone | | | | X | | | | | | |
| Sulfur compounds | | | | | | | | | | |
| Dimethyl disfulfide | X | | X | X | | | | | | |
| Ethers | | | | | | | | | | |
| 2-pentylfuran | | | | | | | | | | X |
| 2,5-dimethylfuran | X | | X | | X | | | | X | X |
| 3-methylfuran | X | | | | | | | | | |
| Esters | | | | | | | | | | |
| Acetic acid, pentyl eser | X | | | | | | | | | |
| Proponioc acid ester (CAS: 74367-33-2) | | | | X | | | | | | |
| Proponioc acid ester (CAS: 74367-34-3) | | | | X | | | | | | |
| n-propyl acetate | X | | | X | | | | | | |
| Nitrogen compounds | | | | | | | | | | |

Table 1.1. MVOCs Produced from Cultures Grown on Building Materials (Continued)

| MVOCs | Pine wood [165] | Pine wood [143] | Particle board [165] | Gypsum Board [165] | Gypsum board [143] | Wallpaper-gypsum board-plastic film[164] | Clipboard-glass wool[164] | Ceramic tile[164] | Spruce wood [143] | Ingrained wall paper[143] |
|---|---|---|---|---|---|---|---|---|---|---|
| Ammonia | | | X | | | | | | | |
| Hexanenitrile | | | X | | | | | | | |
| 2-methylpyridine | | | X | | | | | | | |
| Nitromethane | | | X | | | | | | | |
| pyridine | | | X | | | | | | | |
| Terpenes | | | | | | | | | | |
| 1,3,3-trimethyltricyclohepane | | | | X | | | | | | |
| 3-carene | | | | X | | | | | | |
| 3-thujen-2-ol | | | | X | | | | | | |
| Borneol | | | | X | | | | | | |
| Camphene | | | | X | | | | | | |
| *S*(-)-limonene | | | | X | | | | | | |
| α-pinene | | | | X | | X | X | X | | |
| D-verbenone | | | | X | | X | X | X | | |
| **Acids** | | | | | | | | | | |
| Hexanoic acid | | | | X | | | | | | |

### 1.1.5 Materials Used for the Detection of Alcohols

As previously discussed, finding a material that is able to interact with alcohols and provide a signal when the interaction occurs may be useful for the detection of mold. Several kinds of gas-phase alcohol sensors have been developed, including sensors that employ oxide semiconducting materials[166] and polymers[167]. However, one major problem that exists with these materials is that they are not very selective to alcohol vapors, and they may also interact with other classes of VOCs in the air. Therefore, finding a new material which is selective towards alcohol vapors is very important for sensor development. In the following sections, the available literature on materials for alcohol sensing are reviewed.

#### 1.1.5.1 Inorganic Materials

Oxide sensors consist of an oxide semi-conducting film coated onto a substrate. The most often used oxides are $SnO_2$, $TiO_2$, ZnO, $Fe_2O_3$ and $ZrO_2$. Various oxides were synthesized by different methods and used as sensing materials for alcohol compounds. Nanocrystalline $Fe_2O_{3(0.9)}$ –$SnO_{2(0.1)}$ powders have been prepared using a hydrazine method. The subscript 0.9 or 0.1 refers to the molar percentage of each oxide. This material was found to be able to detect 1000 ppm ethanol vapor in the air[166]. $\gamma$-$Fe_2O_3$ was also prepared by the hydrazine method and showed high sensitivity to alcohols (1 ppm)[168]. A non-equilibrium nanostructured $xZrO_2$-(1-x)$\alpha$-$Fe_2O_3$ (x refers to the molar percentage of the oxide) solid solution system was tested to be highly sensitive to alcohol gas in the air[169]. A radio frequency (RF) sputtering deposition method was used for the fabrication of submicron triangular $TiO_2$ blocks on quartz substrates and was found to have

good alcohol sensing properties[170]. This system was able to detect ethanol to a low concentration of 10-50 ppm at 250-500 °C. $TiO_2$ thin films made by a sol-gel process were applied in methanol and ethanol sensing[171]. Nanostructured $TiO_2$ thin films prepared by a supersonic beam of cluster oxides showed quite good response to ethanol, methanol and propanol[172]. A sol-gel method was used to synthesize $\alpha$-$Fe_2O_3$ sol, which was then dip-coated on to a hydrophilic glass to form a monolayer and multilayers of nanoparticle films[173]. The 30-layer ferric oxide film was sensitive to methanol, ethanol and propanol (2 ppm) at room temperature. More sensitivity was obtained when the alcohol chain length increased. The response and recovery time was very quick (within 1 min). Other alcohol sensing materials studied included tin oxides[174-176], rare earth oxides[177], $xSnO_2$-(1-x)$\alpha$-$Fe_2O_3$[178], zinc oxide[179] and porous silicon[180]. In addition, various methods have been tried to increase the selectivity and sensitivity of oxide sensor by changing the particle size[174, 178] or the thickness of the semiconductor film[176]. Doped sensors show greater sensitivity to oxygenated volatile organic compounds such as alcohols, ketones, etc[181].

The nanoparticle-based chemiluminescence sensor relies on the strong chemiluminescence emission generated by the catalytic oxidation of organic molecules on the surface of nanoparticles. This kind of sensor was also applied in the detection of oxygenated compounds. A nanosized $SrCO_3$-based vapor sensor which was able to generate a chemiluminescence signal, was developed[182]. The sensor showed high selectivity to ethanol. The luminescence characteristics of ethanol and acetone vapors passing through the surface of $TiO_2$ were also

studied[183]. Additionally, a nanosized $ZrO_2$ surface was also shown to generate a chemiluminescence signal when ethanol vapor was introduced to the surface of the particles[184]. The $ZrO_2$ sensor showed high sensitivity to ethanol at a relatively low temperature of 195 °C. Additionally, based on the catalytic chemiluminescence of pinacolyl alcohol on $Al_2O_3$ nanowires, a cataluminescence sensor using $Al_2O_3$ nanowires as the sensing material was investigated to determine trace levels of pinacolyl alcohol in air samples[185]. Because the chemiluminescence sensor depends on a catalytic reaction, this kind of sensor can be reused and demonstrates good stability.

A micro gas sensor based on adsorption and combustion was developed to detect eight kinds of alcohols, including methanol, ethanol, 1-propanol, 2-propanol, 1-butanol, 2-butanol, isobutanol, and tert-butanol[186]. Pd supported γ-$Al_2O_3$ was used as the sensing material. A bridge circuit was used to obtain output signals from the catalytic combustion-type sensor. The sensor was operated with a mode of pulse-driven heating for 0.2s with a cycle of 10s[186]. During the heater-off period, the alcohols adsorb on the sensing and compensating materials. During the 0.2s pulse heating period, the molecules that were adsorbed onto the sensing material were burned and subsequently induced a temperature increase. Thus, response transients to various alcohols were recorded. Eight kinds of alcohols could be identified from the different shapes of the individual response transients. In addition, the shape and response peaks were dependent on the kind of VOC molecules such as acids, alcohols, and aromatics.

Electronic noses (e-noses) consist of an array of multiple sensors combined with pattern recognition methods and may be used in environmental monitoring to provide cost-effective alternatives for accurate, reliable, and speedy identification of environmental pollutants. Many kinds of sensors with different sensitivities and selectivities have so far been tested as sensor arrays. They include metal oxide semiconductors[187-189], organic conducting polymers[190, 191], surface acoustic wave devices[192, 193], and quartz resonators[194, 195]. An electronic nose system based on tin oxide gas-sensors array and artificial neural network for identification of some oxygenated VOCs such as propan-2-ol, methanol, acetone and ethyl methyl ketone was developed[196].

The electrochemical detection of formaldehyde and ethanol (2-40 ppm) was accomplished by combining the $BiCuVO_x$ [197] solid electrolyte with the perovskite-type oxide electrode. The sensor response towards organic gases resulted from the simultaneous electrochemical reactions of oxygen reduction and organic oxidation occurring at the solid electrolyte/oxide electrode interface.

**1.1.5.2 Organic Materials**

Conducting organic polymers have been used previously to detect alcohol compounds. These polymers are made of semiconducting aromatic or heteroaromatic materials deposited onto a substrate and between two electrodes[167]. Upon interacting with organic vapors, a reversible change of electrical conductivity of the device was observed[167]. Bearzotti *et al.*[198] developed an alcohol vapor sensor based on nanobeads of conjugated polymers, namely polyphenylacetylene, and copolymer poly[phenylacetylene-(co-2-

hydroxyethyl methacrylate)]. The sensors are sensitive to aliphatic chain primary alcohol vapors, including methanol, ethanol, n-propanol and n-butanol. Other polymers such as poly-2,5-furylene-vinylene (PFV) derivatives[199] were also studied and the sensors based on those polymers were sensitive to alcohols.

Plastic optical fiber sensors for detecting alcohol vapor have been studied[200]. A polymer such as Novolac resin, $C_6H_4OH(CH_2C_6H_3OH)_m(CH_2OH)_n$, causes swelling when it is exposed to alcohol vapor[200]. The light intensity passing through the sensor head changed remarkably depending on the vapor pressure. The response of this kind of sensor is fast, stable and reproducible. Spin-coated thin films of metal porphyrin-phthalocyanine blend were used as optical chemically interacting materials to detect methanol, ethanol and isopropanol vapors in the UV-Vis spectral range[201].

Silicate-encapsulated yeast alcohol dehydrogenase (ADH) was also employed as a sensor for alcohols and aldehydes in gas-phase environment[202]. The sensing scheme was based on encapsulated ADH/NAD+ or ADH/NADH and utilized a change in fluorescence from the soluble, reduced cofactor nicotinamide adenine dinucleotide (NADH) upon exposure to alcohols or aldehydes.

Quartz crystal microbalance (QCM) sensors consist of a piezoelectric quartz crystal coated with polymer membrane, which is used to absorb the alcohol vapor[203]. The absorption of vapor onto the membrane increases the mass of the sensor and results in a change in its resonance frequency. Polymer-coated quartz crystal microbalance sensors and polymer/carbon black-coated micro-resistance sensor arrays were used as an "electronic nose" to discriminate different primary

alcohol vapors, including methanol, ethanol, propanol, butanol, pentanol, heptanol, octanol and decanol[203]. Different kinds of polymers were coated on eight QCMs or eight micro resistors (μRs). The detection patterns were characterized to each alcohol. Polypyrrole films have the ability to detect and discriminate alcohols (methanol and ethanol) from ketones (acetone, 2-butanone, 2-pentanone)[204]. There are also studies on polymer coated microcantilever-based alcohol vapor sensor[205]. Resistors that were sensitive to stress changes were integrated onto the flexible cantilevers; this made it possible to monitor the cantilever deflection electrically.

Most currently developed materials, including oxides and polymers, have good sensitivities for alcohol vapor or some other oxygenated compound detection. Table 1.2 shows the detection limit or detection range of the sensing materials investigated in the literature. However, their selectivities towards alcohol compounds are relatively low. The e-nose sensor, which is based on a sensing material array, may be able to selectively detect alcohols. However, a series of materials and analysis of complicated sensing patterns from different materials is required for the e-nose to operate. Finding a single material that is able to selectively detect alcohols in a simple way is still a challenge.

Table 1.2. Detection Limit/Range for the Materials Investigated in the Literature

| Material | Detection Limit/Range at Room Temperature | Reference |
|---|---|---|
| Nanocrystalline $Fe_2O_{3(0.9)}$-$SnO_{2(0.1)}$ | 1000 ppm ethanol | 166 |
| $\gamma$-$Fe_2O_3$ | 1-1000 ppm ethanol | 168 |
| Non-equilibrium nanostructured $xZrO_2$-(1-x)$\alpha$-$Fe_2O_3$ solid solution | 10-2000 ppm ethanol | 169 |
| Submicron triangular $TiO_2$ | 20-50 ppm ethanol | 170 |
| $TiO_2$ thin film by sol-gel processing | 3 and 0.1 ppm of ethanol at working temperature of 400 ℃ and 500 ℃, respectively; 6 and 0.3 ppm of methanol for the two working temperatures | 171 |
| Nanostructured $TiO_2$ thin films prepared by supersonic beams | 400 ppm methanol, 400 ppm ethanol and 400 ppm propanol | 172 |
| $\alpha$-$Fe_2O_3$ thin film | 2 ppm propanol | 173 |
| $SnO_2$ thin film | 250 ppm ethanol | 176 |
| $xSnO_2$-(1-x)$\alpha$-$Fe_2O_3$ | 10 ppm ethanol | 178 |
| $ZnO_2$ | 100 ppm ethanol | 179 |
| Porous silicon | 0-0.5% alcohol in the air | 180 |
| Nanosized SrCO3-based chemiluminescence sensor | 2.1 ppm ethanol | 182 |
| Nanosized $TiO_2$ chemiluminescence sensor | 10.5 μg/mL of ethanol and 6.7 μg/mL of acetone dissolved in water | 183 |
| Nanosized $ZrO_2$ chemiluminescence sensor | 0.6 μg/mL of ethanol dissolved in water | 184 |
| Alumina nanowire cataluminescence sensor | 0.0053 μg/mL of pinacolyl alcohol | 185 |
| $SnO_2$ thin film | The gases tested in this paper are 2000-30000 ppm propan-2-ol, 4000-55000 ppm methanol, 2300-31500 ppm acetone, and 1800-24000 ppm ethyl methyl ketone | 196 |
| BiCuVOx solid electrolyte | 2-40 ppm formaldehyde and ethanol | 197 |
| Polyphenylacetylene | aliphatic chain primary alcohols (methanol, ethanol, n-propanol, and n-butanol), 0-$10^4$ ppm | 198 |
| Poly[phenylacetylene-(co-2-hydroxyethyl methacrylate)] (P(PA/HEMA)) | aliphatic chain primary alcohols, (methanol, ethanol, n-propanol, and n-butanol), 1-$10^4$ ppm | 198 |
| Sol-gel-encapsulated alcohol dehydrogenase | 10-1000 mM of ethanol in aqueous phase and 0.1-10 mM of propionaldehyde in aqueous phase | 202 |
| Electronic nose by polymer-coated QCM sensors and polymer/carbon black-coated micro-resistance sensors | Ethanol tested in this paper are around 158 and 316 ppm | 203 |
| Plypyrrole film | The response to methanol vapour in the range of 1000-20000 ppm is reported | 204 |

## 1.2 $CO_2$ and Energy

Besides VOCs, carbon dioxide ($CO_2$) as one of the major contributors to global warming also has significant impact on the climate change. Therefore, to reduce the amount of $CO_2$ is also important and it is the other focus of this dissertation.

### 1.2.1 Problem Statement

Global warming and energy problems are prevalent challenges in the 21st century[206, 207]. In particular, carbon dioxide ($CO_2$) emissions are now considered to be one of the major pollutants contributing to global warming. The last 50 years has provided the strongest evidence that anthropogenic $CO_2$ leads to significant effects on climate[208]. It is critical to find methods to remove this compound from the atmosphere. Although capture and transportation of $CO_2$ is feasible and technically proven, the reliability and safety of long-term storage remains a concern[208].

Photocatalytic materials are drawing significant attention because of their potential for solving environmental and energy problems at the same time. Photocatalytic materials have been used to convert $CO_2$ to fuels. So far, the most studied photocatalytic material is titanium dioxide ($TiO_2$) because it has provided the most efficient photocatalytic activity, high stability, low cost as well as low toxicity[209, 210]. The utility of a semiconductor photocatalyst such as $TiO_2$ lies in its ability to convert photons into chemical energy.

In the photocatalytic reaction to reduce $CO_2$ in the presence of water vapor, $TiO_2$ is excited by UV irradiation. The absorption of energy promotes an

electron to jump from the valance band to the conduction band, leaving a positively charged hole in the valance band. The electrons subsequently move to the surface and react with adsorbed $CO_2$, while water is oxidized by the holes. The reaction mechanism of $TiO_2$ is presented in Figure 1.1. One of the major challenges in using $TiO_2$ as a photocatalyst is electron and hole recombination. The charge recombination impacts photocatalytic efficiency and product formation[211]. The goal is therefore to minimize electron-hole recombination and maximize charge transfer to the catalyst surface.

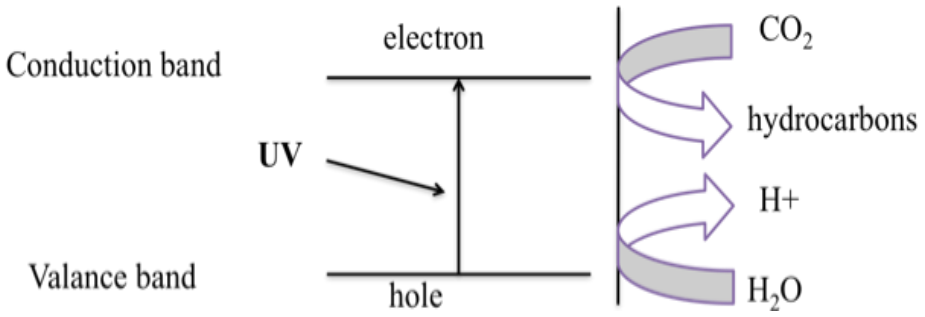


Figure 1.1. The $CO_2$ photoreduction mechanism of $TiO_2$.

### 1.2.2 Literature Review of the Strategies for $TiO_2$ Modification to Enhance Charge Separation

Several strategies have been reported to modify $TiO_2$ based on different principles to enhance its electron-hole separation, and thus increase the photocatalytic activity of $TiO_2$. The major methods to enhance charge separation

include using mixed-phase $TiO_2$, metal modified $TiO_2$, and carbon-$TiO_2$ nanocomposite material.

#### 1.2.2.1 Mixed-Phase $TiO_2$

$TiO_2$ naturally occurs in three polymorphs: anatase, rutile and brookite. The crystal structure for anatase and rutile is tetragonal while the crystal structure for brookite is orthorhombic. Anatase and rutile are the most studied phases of $TiO_2$. Anatase has a band gap of 3.2 eV, which corresponds to a UV wavelength of 385 nm[212]. Anatase exhibits lower rates of electron-hole recombination in comparison to rutile because the hole trapping of anatase is 10 fold greater than that of rutile[212]. In contrast, rutile has a smaller band gap of 3.0 eV with excitation wavelengths that extend to the visible light range at 410 nm[212]. Generally, anatase has much higher activity than rutile[213]. However, mixed-phase $TiO_2$ materials consisting of anatase and rutile phases are found to be better photocatalysts than pure-phase photocatalysts[214, 215]. It is because of the synergic effect that an enhancement of spatial charge separation is usually invoked[216]. The charge transfer between the anatase and rutile particles of anatase-rutile mixture was confirmed by a photoluminescence study[217].

Currently there are two explanations for the interfacial charge transfer between anatase and rutile in the mixed-phase $TiO_2$[212]. The first explanation assumed that when anatase interweaves with rutile, anatase was activated by UV irradiation. Photogenerated electrons flow from anatase to rutile, while the holes transfer from rutile to anatase. This proposed charge movement is due to the position of the conduction band edge of anatase being positioned above that of

rutile[212]. Therefore, an anatase-rutile mixed phase could hinder electron-hole recombination by locating the electron and hole in different crystalline phases [211, 218]. The charge separation model of P25 (75% anatase and 25% rutile in weight) for this explanation is presented in Figure 1.2 (1). However, this model did not take into account the significantly lower energies of the lattice or surface trapping sites. It was reported that the anatase trapping site is 0.8 eV lower in energy than the anatase conduction band and it is below the rutile conduction band as well[219]. Recent reports also suggests the possibility of electron "spillover" from rutile in high-temperature treated materials[220].

A second explanation for improvements in electron-hole separation in mixed-phase $TiO_2$ is also the synergism between the rutile and anatase phases. However, the electron is proposed to transfer from rutile to anatase[212]. Ohno and co-workers studied anatase rutile mixed-phase $TiO_2$ for naphthalene photo-oxidation and found that naphthalene is mainly oxidized on rutile particles while oxygen is mainly reduced on anatase particles[221]. Past work shows that the electron and hole are separated and locate at different phases of $TiO_2$. It indicates that electrons mainly transfer to the anatase phase, while the majority of holes are at rutile phase.

The electron paramagnetic resonance spectroscopy (EPR) study of P25 indicates that the presence of rutile crystallites creates a structure where rapid electron transfer from rutile to lower energy anatase lattice trapping sites under visible illumination leads to a more stable charge separation[212]. Electrons subsequently move to surface trapping sites and react with the adsorbed

compounds[212]. The model for the second explanation of charge transfer of P25 is shown in Figure 1.2 (2). The explanation that the electron is proposed to transfer from rutile to anatase is more convincing since it has been supported by evidence and also considers the lower energies of lattice and surface trapping sites.

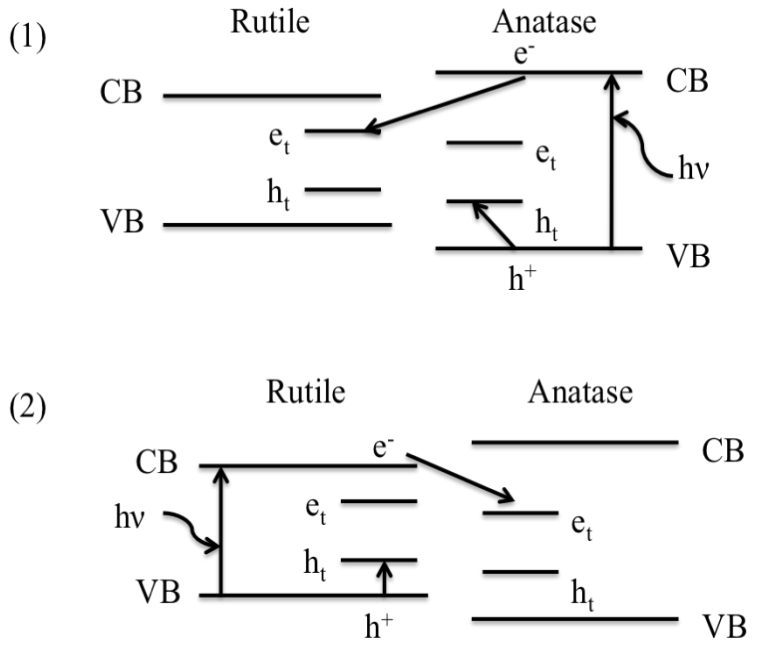


Figure 1.2. Charge separation model of P25[212], $e_t$ and $h_t$ represent electron trapping site and hole trapping site, respectively.

So far, most publications used mixed phase $TiO_2$ for photo-oxidation of organic pollutants. There are only a few papers studying mixed-phase (anatase/rutile) $TiO_2$ for the photoreduction of $CO_2$. $TiO_2$ pellets extruded from P25 after heating and vacuum treatment was studied by Tan *et al*[222]. $CH_4$ was the major product under continuous UV irradiation. CO and $H_2$ were also detectable. Pyrex glass pellets pre-immobilized with P25 were used for $CO_2$ photoreduction

in the presence of $H_2O$ and $H_2$. $CH_4$, a small amount of CO and $C_2H_6$ were the products[223]. Mixed phase $TiO_2$ films were synthesized by direct current magnetron sputtering and used for $CO_2$ photoreduction. $CH_4$ was found to be the product. Gray and co-workers studied synthesized mixed phase $TiO_2$ for $CO_2$ photoreduction in the aqueous phase with sodium bicarbonate and isopropanol[216]. Methane and ethane were found to be the products. Both the synthesized mixed-phase $TiO_2$ and P25 had higher activities than pure anatase.

#### 1.2.2.2 Metal Modified $TiO_2$

Metals can modify a semiconductor by changing the distribution of electrons[224]. Metal and n-type semiconductor (e.g. $TiO_2$) have different Fermi level positions. When the two materials are connected, electron migrates from the semiconductor to the metal until the two Fermi levels are aligned[224]. The electrical contact has formed a space charge layer. The surface of the metal acquires an excess negative charge while the semiconductor exhibits an excess positive charge because of the electron migration away from the barrier region. The barrier formed at the metal-semiconductor interface is called the Schottky barrier[224].

For the metal modified semiconductor materials, after excitation the electron migrates from the semiconductor to the metal where it becomes trapped and the electron-hole recombination is suppressed. The hole is then free to diffuse to the semiconductor surface where a reaction can occur[224]. The metal can enhance the yield of a particular product or the rate of the photocatalytic reaction.

The addition of a metal to a semiconductor surface can also change the major reaction products[224].

Platinum and/or copper loaded nitrogen-doped titania nanotube arrays were used for $CO_2$ photoreduction with water vapor under sunlight. The metal loaded titania nanotube has significantly enhanced production rate of methane as compared to non-metal modified titania nanotube. CO and $H_2$ were also found to be the products[225]. Copper (Cu) loaded $TiO_2$ in $CO_2$ photoreduction was studied by Tseng and co-workers and they found that the yield of methanol for Cu loaded $TiO_2$ is much higher than those of sol-gel synthesized $TiO_2$ and Degussa P25 because of the lower possibility for electron-hole pair recombination contributed from Cu[226]. Zhang *et al.* investigated the Cu and Iodine co-modified $TiO_2$ nanoparticles for $CO_2$ photoreduction with water vapor[227]. The production rate of CO for Cu modified $TiO_2$ was significantly higher than that of the bare $TiO_2$ nanoparticles[227].

Li *et al.* studied silica supported Cu/$TiO_2$ nanoparticles for $CO_2$ photoreduction with $H_2O$ vapor[228]. Without Cu loading, CO was the primary product. However, the addition of Cu species in the form of $Cu_2O$ markedly increased the overall $CO_2$ conversion efficiency as well as the selectivity towards $CH_4$. Cu suppressed electron hole recombination and enhanced multi-electron reactions[228].

One challenge with using metal modified $TiO_2$ is that the metal may also act as new recombination centers for electrons and holes and hence lead to a decrease in the photocatalytic activity[229]. In the case of deep doping of the metal,

metal ions likely behave as recombination centers since electron-hole transfer to the interface is more difficult. Moreover, an optimum concentration of doped metal ion exists. The photocatalytic activity decreases when the metal doping is above a certain level due to an increase in charge recombination[209].

#### 1.2.2.3 Carbon-$TiO_2$ Nanocomposite Material

In the past decade, the interests in carbonaceous nanomaterials and $TiO_2$ photocatalysts have come together. The role of carbonaceous nanomaterials in photocatalytic processes has drawn significant attention because of their unique properties and the potential to control their structural and electrical properties[230].

The major structures and modes of using carbonaceous nanomaterials in conjunction with $TiO_2$ as photocatalyst investigated in the literature are activated carbon, carbon doping, carbon nanotubes (CNTs) and [60]-fullerene and graphene. The current difficulties to obtain high photocatalytic efficiency of $TiO_2$ may be overcome by a) tuning band-gap or extending wavelength through photosensitization that $TiO_2$ could work in visible light range b) reducing electron-hole recombination and c) providing high surface area for adsorption of reactants and providing more active sites[230]. Nanocarbon-$TiO_2$ has potential in all three perspectives. Indeed, the nanocarbon-$TiO_2$ composites, CNTs and graphene in particular, have shown enhanced photocatalytic activity over $TiO_2$ in various applications[231-234].

Graphene may have an even better photocatalytic performance as compared to other nanocarbon materials. Graphene is an atomic sheet of $sp^2$-bonded carbon atoms that are arranged into a honeycomb structure[235]. Electrons

can travel without scattering at mobility exceeding ~15,000 $m^2V^{-1}s^{-1}$ at room temperature[236-240]. The high electron mobility of graphene makes them potentially ideal electron sinks or electron transfer bridges[236-240]. Nearly 90% enhancement in the photocurrent is seen in the graphene-$TiO_2$ as compared to bare $TiO_2$ where graphene serves as electron collector and transporter[234]. Compared to cylindrical CNTs, planar graphene may have smaller electron transfer barrier, thus the electron-hole recombination is less[241]. In addition, graphene has better conductivity and larger surface area[236, 242]. The better conductivity will lead to a faster transport of electrons, thus better preventing them from recombining with holes. A significant enhancement in reaction rate of degradation of mehylene blue is observed with P25-graphene, compared to the bare P25 and P25-CNTs with the same carbon content[232]. A decrease in charge transfer resistance of P25-graphene sample was observed compared to P25[232]. Furthermore, compared to carbon nanotube or nanowire, graphene is easier to produce from natural graphite through chemical oxidation-dispersion-reduction process at a low cost.

For other nanocarbon materials, such as activated carbon and carbon doping, the adsorptivity of reactants decreases markedly during photoreaction. The presence of carbon weakens the light intensity arriving at catalysts' surface. Exfoliated graphene sheets have a theoretical surface area of ~2600 $m^2g^{-1}$[243]. In addition, graphene has one-atom-thick structure which provides high transparency[244]. Graphene has great adsorptivity of reactants and better transparency of light compared to other nanocarbon materials.

$TiO_2$ graphene composite has the potential to be activated by visible light. Zhang *et al*. reported that there is an obvious red shift of 30-40 nm in the absorption edge of $TiO_2$-graphene sample as compared to bare $TiO_2$ nanoparticles[232]. This may be attributed to the formation of a Ti-O-C bond through chemical bonding between the $TiO_2$ and graphene, thus resulting in an extended photo responding range of 430-440 nm and more efficient utilization of the solar spectrum. Past research has shown that $TiO_2$-graphene shows significant improvement in the photodegradation of methylene blue over bare $TiO_2$ nanoparticles, especially under visible light irradiation[232].

The combination of $TiO_2$ and carbonaceous materials as photocatalyst has been applied to different fields. The most extensively investigated application is the treatment or degradation of environmental pollutants, i.e. phenol, humic substances, metallic ions, or dyes such as methylene blue and methyl orange[245, 246]. $TiO_2$ and carbonaceous material also gain increasing attention in fuel cells[247]. Another important application is to produce sustainable solar fuel by water splitting to form hydrogen[209, 248-251]. The research on photocatalytic degradation of gaseous pollutant species is much lesser (i.e. NOx)[252].

There are only a few studies that utilize $TiO_2$ nanocarbon composite materials for the reduction of carbon dioxide ($CO_2$) in the presence of $H_2O$ vapor; these are summarized in Table 1.3. Xia *et al*. synthesized multi-walled carbon nanotube (MWCNT) supported $TiO_2$ and investigated its photocatalytic activity in the reduction of $CO_2$ with $H_2O$[253]. Different methods were used to synthesize the MWCNTs-$TiO_2$ composite. Both syntheses methods led to the production of

$C_2H_5OH$, HCOOH and $CH_4$. However, the sol-gel method led mainly to the formation of $C_2H_5OH$, while HCOOH was found to be the major product of $CO_2$ photoreduction on the same sample prepared using the hydrothermal method. The total production rates of the products were much higher than those reported in other literature, which focused on other methods to modify $TiO_2$ (i.e. Cu doping, Cu-Fe co-doping $TiO_2$/porous silica, $TiO_2$ nanotube)[254-261] under UV light. The results may indicate that carbon modification of $TiO_2$ is better than other materials in terms of enhancing efficiency.

Liang *et al* reported photoreduction of $CO_2$ and $H_2O$ vapor to fuel using graphene-$TiO_2$ films[262]. So far, this is the only paper found to apply graphene-$TiO_2$ to convert $CO_2$ to fuel. Two kinds of graphene were produced with different extents of defect. A graphite flake oxidation followed thermal reduction in solvent (solvothermal reduction) method was used to produce reduced graphite oxide (RGO). A solvent exfoliation of graphite flake without oxidation method was used to produce less defective solvent-exfoliated graphene (SEG). The product of photoreduction for both materials was $CH_4$.

Table 1.3. Overview of Literature Data of $TiO_2$-Nanocarbon Materials on Photoreduction of $CO_2$ with $H_2O$ (g)

| **Material** | **Synthesis Method** | **Light Source** | **Products/Production rate** | **Reference** |
|---|---|---|---|---|
| MWCNTs-anatase $TiO_2$ | Sol-gel | UV | $C_2H_5OH$ (major)=23.2, HCOOH=6.0, $CH_4$=3.7 ($\mu$mol/g$TiO_2$-hr) | Xia *et al.* [253] |
| MWCNTs-rutile $TiO_2$ | Hydrothermal | UV | HCOOH (major)=25.0, $C_2H_5OH$=6.9, $CH_4$=12.7 ($\mu$mol/g$TiO_2$-hr) | Xia *et al.* [253] |
| SEG-P25 film | Solvent exfoliation | UV<br>Visible | $CH_4$=8.1 ($\mu$mol/$m^2$ –hr)<br>$CH_4$=3.6 ($\mu$mol/$m^2$ –hr) | Liang *et al.* [262] |
| RGO-P25 film | Oxidization followed solvothermal reduction | UV<br>Visible | $CH_4$=1.8 ($\mu$mol/$m^2$ –hr)<br>$CH_4$=1.2 ($\mu$mol/$m^2$ –hr) | Liang *et al.* [262] |

### 1.2.3 The Product Selectivity of $TiO_2$ in $CO_2$ Photoreduction

So far, various products were reported for $CO_2$ photoreduction by $TiO_2$. These products include CO, $CH_4$, $CH_3OH$, formaldehyde (HCHO), formic acid (HCOOH), ethanol ($C_2H_5OH$), $C_2H_4$ and $C_2H_6$. Table 1.4 summarizes the products for each $TiO_2$ based catalyst for $CO_2$ photoreduction. The selectivity of products for $CO_2$ photoreduction is not conclusive in the literature. There is only an indication that Cu loading favors the production of methane[228] or methanol[256]. Some papers have proposed the reaction mechanisms of $TiO_2$ based catalysts for $CO_2$ photoreduction[227 253].

For CO formation, Zhang *et al* has proposed the following reaction mechanism for Cu-iodine co-modified $TiO_2$ (Reaction 1.1-1.6)[227]. The formation of CO is the first step and CO is the first product in the photoreaction followed the production of $CH_4$. However, CO is the major product.

$$TiO_2 + h\nu \rightarrow e^- + h^+ \quad \text{(Reaction 1.1)}$$

$$2H_2O + 4h^+ \rightarrow 4H^+ + O_2 \quad \text{(Reaction 1.2)}$$

$$CO_2 + 2H^+ + 2e^- \rightarrow CO + H_2O \quad \text{(Reaction 1.3)}$$

$$H_2O + e^- \rightarrow H\bullet + OH^- \quad \text{(Reaction 1.4)}$$

$$CO + e^- \rightarrow C\bullet \quad \text{(Reaction 1.5)}$$

$$C\bullet + H\bullet \rightarrow \{CH\bullet, CH_2\bullet\} \rightarrow CH_3\bullet \rightarrow CH_4 \quad \text{(Reaction 1.6)}$$

For $CH_4$, HCOOH and $C_2H_5OH$ formations, Xia *et al* proposed the following $CO_2$ photoreduction reaction mechanism for multi-walled carbon nanotube supported $TiO_2$ (Reaction 1.7-1.13)[253]. The formation of $CO_2^-$ is the critical step for this reaction mechanism.

$$TiO_2 + h\nu \rightarrow e^- + h^+ \quad \text{(Reaction 1.7)}$$

$$4h^+ + 2H_2O \rightarrow 4H^+ + O_2 \quad \text{(Reaction 1.8)}$$

$$H^+ + e^- \rightarrow H\cdot \quad \text{(Reaction 1.9)}$$

$$e^- + CO_2 \rightarrow CO_2^- \quad \text{(Reaction 1.10)}$$

$CH_4$ formation: $8H\cdot + CO_2^- + h^+ \rightarrow CH_4 + 2H_2O$ (Reaction 1.11)

HCOOH formation: $2H\cdot + CO_2^- + h^+ \rightarrow HCOOH$ (Reaction 1.12)

$C_2H_5OH$ formation: $12H\cdot + 2CO_2^- + 2h^+ \rightarrow C_2H_5OH + 3H_2O$ (Reaction 1.13)

The number of electrons that are separated from holes and involved in the surface reaction might be the reason for different product selection. For example, four electrons are needed in CO formation (Reaction 1.1-1.3) while eight electrons are required for $CH_4$ formation in both reaction mechanisms for $CH_4$ formation above (Reaction1.1-1.6 & Reaction 1.7-1.11). More electrons are needed to form HCOOH or $C_2H_5OH$. So far, many papers reported the formation

of CO as the major product. However, CO, as a synthesis gas, cannot be used as a fuel directly while $CH_4$ is an energy-rich fuel. Therefore, the selective production of $CH_4$ may be more beneficial. To selectively produce $CH_4$, more electrons may need to be transferred to the catalyst surface. Therefore, electron-hole pair separation may not only be critical for the efficiency of the catalyst in $CO_2$ photoreduction, but also essential for enhancing product selectivity. More studies regarding the selectivity of products for $TiO_2$ based photocatalysts in $CO_2$ photoreduction in the presence of water vapor are needed.

Table 1.4. Overview of the Products of $TiO_2$ and Modified $TiO_2$ in Photoreduction of $CO_2$

| Material | Reactants | Light Source | Products | Reference |
|---|---|---|---|---|
| $TiO_2$ pellet | $H_2O$ vapor | UV | $CH_4$, CO, and $H_2$ | 222 |
| Pyrex glass pellets pre-immobilized with P25 | $H_2O$ vapor and/or $H_2$ | UV | $CH_4$, CO and $C_2H_6$ | 223 |
| Mixed phase $TiO_2$ film | $H_2O$ vapor | UV | $CH_4$ | 263 |
| Pt and/Cu loaded N-$TiO_2$ nanotube | $H_2O$ vapor | Sunlight | $CH_4$ , CO and $H_2$ | 225 |
| Synthesized mixed phase $TiO_2$ at 773 K | with sodium bicarbonate and isopropanol | UV/Vis | $CH_4$ and ethane | 216 |
| $Cu/TiO_2$ | 0.2M NaOH | UV | $CH_3OH$ | 226 |
| silica supported $TiO_2$ nanoparticles | $H_2O$ vapor | UV | CO | 228 |
| silica supported $Cu/TiO_2$ nanoparticles | $H_2O$ vapor | UV | CO and $CH_4$ | 228 |
| $Cu/TiO_2$ | $H_2O$ vapor | UV/Vis | CO, $CH_3Cl$ when $CuCl_2$ as Cu precursor, trace $CH_4$ | 227 |
| Cu-I/$TiO_2$ | $H_2O$ vapor | UV/Vis | CO, $CH_3Cl$ when $CuCl_2$ as Cu precursor, trace $CH_4$ | 227 |
| Ru doped $TiO_2$/Silica | water | UV | $CH_3OH$, HCHO, $CH_4$, trace $H_2$ | 264 |
| $Cu/TiO_2$.optical fiber | $H_2O$ vapor | UV | $CH_3OH$ | 259 |
| $TiO_2$/porous Vycor glass | $H_2O$ vapor | UV | $CH_4$, trace CO, $CH_3OH$, $C_2H_4$, $C_2H_6$ | 256 |
| MWCNTs-anatase $TiO_2$ | | UV | $C_2H_5OH$ (major), HCOOH, and $CH_4$ | 253 |
| MWCNTs-rutile $TiO_2$ | | UV | HCOOH (major), $C_2H_5OH$, and $CH_4$ | 253 |
| RGO-P25 film | $H_2O$ vapor | UV/ Visible | $CH_4$ | 262 |
| SEG-P25 film | $H_2O$ vapor | UV/ Visible | $CH_4$ | 262 |

## 1.3 Objectives and Overview of Document

There are three major goals for this work:

(1) To better understand the fate of oxygenated VOCs in air.

(2) To develop a material for indoor VOC sensing and control by (a) employing closely coupled computational and experimental work to investigate sorption and (b) by determining association and dissociation constants.

(3) To develop and study a novel $TiO_2$ photocatalyst material to reduce $CO_2$ and produce fuels.

The first objective, which is detailed in Chapter 2, was achieved by undertaking a kinetic study of the gas-phase reactions of a series of unsaturated biogenic aldehydes with OH radicals. Specifically, the $^{\cdot}$OH- initiated transformations of *trans*-hexenal, *trans*-octenal and *trans*-nonenal were investigated, and kinetic rate constants as well as atmospheric lifetimes (with respect to OH radical reaction) were determined. Most of the VOCs studied in this work have not been investigated in previous studies. The rate constants obtained in this study were compared to the rate constants that were predicted using the Structure Activity Relationship (SAR) for gas-phase OH radical reactions with VOCs[96]. A recommended rate constant for larger unsaturated aldehydes, i.e. those with carbon numbers larger than 5, was determined. The information obtained in this work is useful input for air quality models, and has already been published in a high impact peer-reviewed journal[88].

The second objective of this work is detailed in Chapters 3 and 4. This objective was achieved by studying the interactions between novel materials and different classes of VOCs and ultimately determining the material which was best able to selectively interact with the target classes of VOCs. Both mechanistic and

kinetic studies were performed to investigate the interactions between the novel materials and VOCs.

In Chapter 3, the interactions between a series of classes of VOCs and an ionic liquid thin film surface are presented. This chapter is adapted from work that now appears in the published peer-reviewed literature[265]. The objective of looking at the interaction between material surfaces and different classes of VOCs is to find the material which selectively interacts with alcohols. Here, the selectivity of the material towards the VOCs of interest is very important since air has complex components. Both computational and experimental tools were applied to investigate those interactions. The Gaussian computational chemistry package was initially applied to screen different materials and ultimately predict the likelihood of the interaction between different materials and VOCs. The computational tool was useful in guiding the experimental design, since it could effectively minimize the cost and time for the following experiment.

The ultimate goal for VOC detection is to develop a sensor which is selective to alcohols. The reversibility of the sensor is very important for its application, and thus, target VOCs should be able to associate and dissociate from the sensor surface in order to allow for repeated use. In Chapter 4, the association and dissociation between ionic liquid surfaces and either gas-phase alcohols or an organic acid were investigated. Association and dissociation rate constants were determined, and could be used to characterize the strengths of the interactions between the thin film surface and the volatile species studied. In addition, at the

end of Chapter 4, the future work and consideration for design of a mold sensor is illustrated.

Chapter 5 illustrates the research on air pollutant removal, and utilizes the previously established general understanding of the reactions of gaseous species, ionic liquids, and interactions with surfaces. Chapter 5 addresses the work of developing a novel $TiO_2$-carbon nanocomposite material and applying it for $CO_2$ photoreduction in the presence of water vapor. The product of $CO_2$ photoreduction using the newly designed catalyst material was investigated.

Chapter 6 proposes the future work to further modify $TiO_2$ to extend its light absorption to visible range.

# CHAPTER 2

# THE INTERACTION BETWEEN VOCS AND HYDROXYL RADICALS: A KINETIC STUDY

## 2.1 Introduction

Biogenic volatile organic compounds (BVOCs) play an important role in atmospheric chemistry. It is well known that BVOCs will react with hydroxyl radicals (OH radicals), ozone and $NO_3$ radicals [66, 266]. They may form secondary organic aerosols which are harmful to human health and degrade air quality and visibility. In addition, the reaction of BVOCs will produce ozone, which is a nationally regulated pollutant. Therefore, it is crucial to understand how these compounds react in the atmosphere.

This work is aimed at investigating the gas-phase reactions of OH radicals with three aldehydes: *trans*-2-hexenal, *trans*-2-octenal and *trans*-2-nonenal. *Trans*-2-hexenal, *trans*-2-octenal and *trans*-2-nonenal are unsaturated aldehydes with similar structures, as seen in Figure 2.1. Aldehydes play a critical role in atmospheric chemistry, primarily because of their formation as secondary products[54, 58]. However, certain aldehydes also emanate directly from biogenic sources. *Trans*-2-hexenal can be emitted from various sources, such as grass crops[34] and leaves [19, 267, 268]; there is an especially enhanced emission of trans-2-hexenal from wounded leaves[19, 20]. *Trans*-2-octenal is emitted from black tea leaves[269]. *Trans*-2-nonenal has been identified as an odor of mushrooms[270].

*trans*-2-hexenal 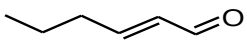

*trans*-2-octenal 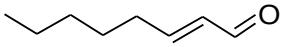

*trans*-2-nonenal 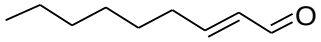

Figure 2.1. Structures of *trans*-2-hexenal, *trans*-2-octenal and *trans*-2-nonenal.

The rate constant of OH radicals with *trans*-2-hexenal has been studied previously [51, 69, 83, 271]. Atkinson *et al.*[10] used the relative rate technique with *trans*-2-butene as the reference compound, and other researchers used an absolute rate technique to determine $k_{OH + trans\text{-}2\text{-}hexenal}$. In this work, the rate constant is determined using the relative rate technique, with comparison against two different reference compounds. This is the first study of the rate constant of OH radicals with *trans*-2-octenal and *trans*-2-nonenal.

According to the Structure Activity Relationship (SAR) [96], the OH radical reactions with unsaturated aldehydes such as *trans*-2-hexenal, *trans*-2-octenal or *trans*-2-nonenal will proceed by hydrogen abstraction from the –CHO group, OH radical addition to the double bond and hydrogen abstraction from the $–CH_3$ and $–CH_2$- groups. At room temperature, H atom abstraction from the –CHO group and OH addition to the double bond are predicted to account for more than 95% of the overall OH radical reaction. Based on the SAR, the rate constants of OH radicals with a series of *trans*-2-aldehydes should increase with increasing carbon number. Davis *et al.*[83] recently measured the rate constant for the reaction of OH with *trans*-2-pentenal, *trans*-2-hexenal and *trans*-2-heptenal. The rate constants

obtained at 297 K were, respectively, $(4.3 \pm 0.6) \times 10^{-11}$, $(4.4 \pm 0.5) \times 10^{-11}$, and $(4.4 \pm 0.7) \times 10^{-11}$ $cm^3 molecule^{-1} s^{-1}$. These data do not show an increasing trend, as might be expected from the SAR. Thus, the question is whether there is indeed a trend of increasing rate constants with the addition of $-CH_2-$ groups in this series of unsaturated oxygenated organic compounds. The goal of this work is therefore to add additional information to the current database by measuring the hydroxyl radical rate constants of *trans*-2-hexenal, *trans*-2-octenal and *trans*-2-nonenal and test the performance of the SAR against this series of unsaturated aldehydes.

## 2.2 Experimental Section

### 2.2.1 Experimental Method

The relative rate method was applied to determine the rate constant of the gas-phase reactions of *trans*-2-hexenal, *trans*-2-octenal and *trans*-2-nonenal with OH radicals. The unknown rate constant of a compound can be determined by using a known rate constant of a reference compound. The equation associated with the relative rate method is:

$$\ln \frac{[\text{target compound}]_0}{[\text{target compound}]_t} = \frac{k_1}{k_2} \ln \frac{[\text{reference}]_0}{[\text{reference}]_t} \qquad \text{(Equation 2.1)}$$

given that

$$\text{Target compound} + {}^{\cdot}OH \rightarrow \text{Products} \qquad \text{(Reaction 2.1)}$$

$$\text{Reference} + {}^{\cdot}OH \rightarrow \text{Products} \qquad \text{(Reaction 2.2)}$$

In Equation 2.1, $[\text{target compound}]_0$ and $[\text{reference}]_0$ are the concentrations of the target compound (i.e. *trans*-2-hexenal, *trans*-2-octenal or *trans*-2-nonenal) and reference compound, respectively, at time zero. The symbols, $[\text{target compound}]_t$

and $[reference]_t$ are the concentrations of the target and reference compounds at time t, and $k_1$ and $k_2$ are the rate constants for reactions 2.1 and 2.2, respectively. When the values of the logarithmic terms on the left and right sides of Equation 2.1 are plotted, the slope of the linear trend line is $k_1/k_2$, or the relative rate. Therefore, when the OH rate constant of the reference compound ($k_2$) is known, then $k_1$ can be calculated. For the reaction rate constant of *trans*-2-hexenal with OH radicals, 2-methyl-2-butene and β-pinene were used as reference compounds. The OH rate constants of methyl-2-butene and β -pinene are 86.9 $\times 10^{-12}$ $cm^3molecule^{-1}s^{-1}$ and 74.3 $\times 10^{-12}$ $cm^3molecule^{-1}s^{-1}$, respectively [53]. For the *trans*-2-octenal experiment, butanal and β–pinene were used as references. For the *trans*-2-nonenal experiment, butanal and *trans*-2-hexenal were used as references. The reaction rate constant of butanal with OH is 24.7 $\times 10^{-12}$ $cm^3molecule^{-1}s^{-1}$ [57], and the reaction rate constant of *trans*-2-hexenal with OH was determined in this research. It is important to note that initially β-pinene and 2-methyl-2-butene were used as references for *trans*-2-nonenal. However, interferences occurred in the analyses, hence *trans*-2-hexenal was used as a reference compound since it was studied in this work as well as in other laboratories.

### 2.2.2 Apparatus and Experimental Procedure

The experiment was performed in an indoor photochemical chamber composed of 2 mil Tedlar® film (SKC Inc.), with a volume of approximately 100 L. The chamber was suspended in a wood cabinet containing twelve fluorescent black lamps (Sylvania, F40T12/BL) in two banks of six surrounding the chamber. In the experiment, only four lamps with two in each bank were used. The lamps

were used to initiate the chemistry. The inside surface of the cabinet was covered with a highly reflective material to provide uniform irradiation, and a fan was installed to ensure an even temperature distribution around the chamber.

Methyl nitrite was used as the hydroxyl radical precursor. Methyl nitrite was synthesized according to Taylor *et al* [272] and stored in a high pressure gas cylinder to prevent explosions. Hydroxyl radicals were produced by photolysis of the methyl nitrite in air through the following reaction mechanism:

$$CH_3ONO + h\nu \rightarrow CH_3O^{\cdot} + NO, \qquad \text{(Reaction 2.3)}$$

$$CH_3O^{\cdot} + O_2 \rightarrow HCHO + HO_2^{\cdot}, \qquad \text{(Reaction 2.4)}$$

$$HO_2^{\cdot} + NO \rightarrow {}^{\cdot}OH + NO_2. \qquad \text{(Reaction 2.5)}$$

Nitric oxide (Aldrich Chemical Company, 98.5%) was added into the chamber to minimize ozone accumulation and maximize the conversion of hydroperoxy radicals to hydroxyl radicals.

The target and reference compounds were purchased from Aldrich Chemical company, with the following stated purities: ≥95%, 94+%, 97%, ≥99.5%, 99% and ≥99.0% for *trans*-2-hexenal, *trans*-2-octenal, *trans*-2-nonenal, 2-methyl-2-butene, β-pinene, and butanal, respectively. The reactants were introduced into the chamber by two methods: direct syringe injection and via an evacuable glass manifold system and using direct syringe liquid injection accompanied by vaporization. Methyl nitrite and nitric oxide were introduced into the chamber using a custom designed evacuable glass manifold system and flushed into the chamber with zero air. Liquid samples of the unsaturated oxygenated organic compounds and references were injected using a 10 μL

syringe (Hamilton, Inc) into a stream of zero air (Air Liquide America Corp., 99.999% purity) flowing to the chamber. The flow rate of zero air was monitored and controlled by a mass flow controller (Omega, Inc). The chamber was filled with approximately a 78-80 L mixture of zero air and reactants. Since the volume of reactant injected, the density and molecular weight of reactant, and the final volume of the chamber were known, the final concentrations of each reactant could be calculated. Typical initial concentrations of each compound in the chamber were 2-6 $ppm_v$ of *trans*-2-hexenal, *trans*-2-octenal, *trans*-2-nonenal, 2-methyl-2- butene, β-pinene, and butanal, respectively; 40-70 $ppm_v$ methyl nitrite; and 10-40 $ppm_v$ nitric oxide.

The reaction chamber was interfaced to a gas chromatograph with a mass spectral detector (Varian, Model CP 3800). The GC-MS was used to both positively identify and quantify compounds. The air sample was trapped at liquid nitrogen temperatures in the front trap containing nickel tubing packed with a multi-bed of carbon adsorbents followed by rapid desorption into the middle cryo-focus trap containing empty nickel tubing. The sample was rapidly heated and passed onto the column head. The column used was a highly inert non-polar low bleed GC column (Varian VF-1ms) of the following dimensions: 30m $\times$0.25mm $\times$0.99μm. The column temperature started from 50°C, was held at 50°C for 3 minutes, then ramped at a rate of 20°C/min to 200°C, and subsequently held at 200°C for 3 minutes.

After the mixture of methyl nitrite, NO, reference compounds, and the target compound in air were added to the chamber, the UV lights were turned on

in 10-20 s intervals for a maximum total of 2 minutes. The GC/MS was used to measure the concentrations of the target and reference compounds. The experiments for the OH reactions with *trans*-2-hexenal, *trans*-2-octenal and *trans*-2-nonenal were conducted separately. Thus, for each experiment, only one target compound with one or two reference compounds were admitted to the bag. Each relative rate experiment was repeated 2 or 3 times.

Prior to beginning all relative rate experiments, background experiments were also performed to characterize the losses and potential interferences in the analyses. Initial tests were conducted to see whether there was a loss of compounds to the wall of chamber over the time scales typical of those used in the rate constant experiment (about 6 hours, including analyses times) and whether there was a loss of compounds due to photolysis over the total photolysis time applied in the experiment (about 2 min). For the loss to the wall test, the compounds of interest and reference compounds were added to the bag and equilibrated in the dark for 6 hours. For the test of loss due to photolysis, all the target and reference compounds were irradiated by UV light for 2 minutes. The target and reference compound concentrations before and after these tests were determined by GC/MS. In addition, experiments were performed to determine whether the peaks from the products of OH radical reactions with the target and reference compounds interfered with the GC analysis of the target and reference compounds. In this test, only one target or reference compound, methyl nitrite and nitric oxide were added to the bag. The sample was irradiated by UV light for 2 minutes. The retention times of the products were compared to those of the target

and reference compounds to determine whether the products interfered with the analyses.

### 2.3 Results and Discussion

#### 2.3.1 Rate Constant

The data show that the combined losses of the target and reference compounds to the walls or to photolysis are within 8%, i.e. within the range of uncertainty of the GC-MS. Therefore, decreases in concentrations of the target and reference compounds to the chamber walls and photolysis were essentially negligible. The gas chromatograms indicated that the products eluted from the GC at different times than the target and reference compounds. Thus, there was no interference with the analyses. The retention times for 2-methyl-2-butene, butanal, *trans*-2-hexenal, β-pinene, *trans*-2-octenal, and *trans*-2-nonenal are 2.3, 3.1, 7.0, 8.7, 9.3 and 10.2 min, respectively.

The experimental data for *trans*-2-hexenal, *trans*-2-octenal, and *trans*-2-nonenal are plotted according to Equation 2.1 in Figures 2.2, 2.3, and 2.4, respectively. The lines are linear least-squares fits of the data. The relative rate constant ratios, $k_1/k_2$, and the calculated rate constants of reaction of OH radicals with *trans*-2-hexenal, *trans*-2-octenal and *trans*-2-nonenal are summarized in Table 2.1.

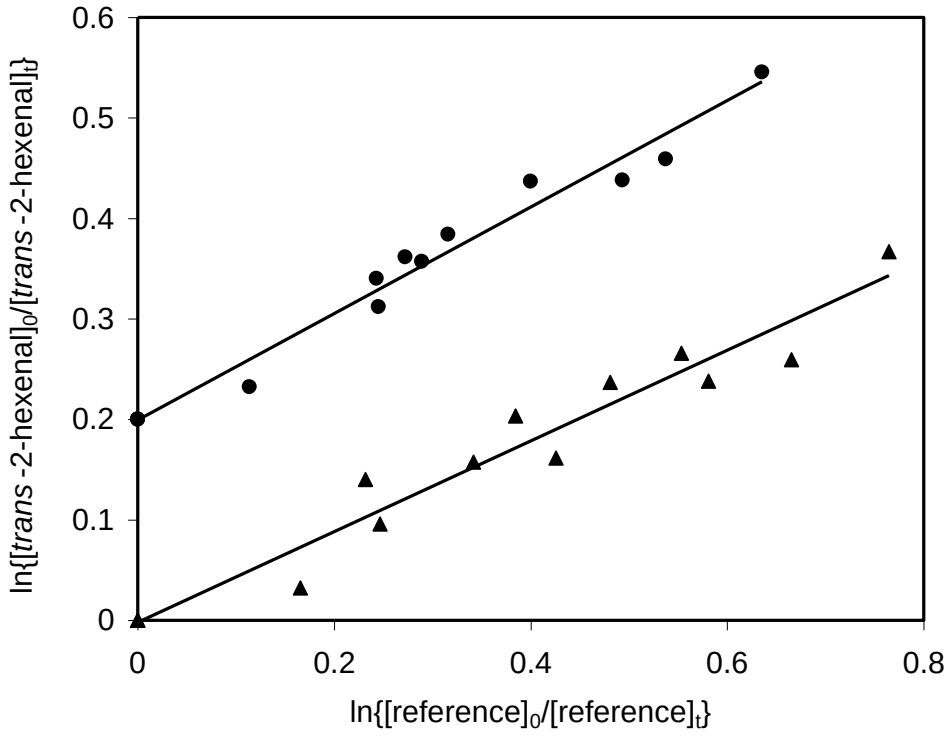


Figure 2.2. Plot of Equation 2.1 for the gas-phase reaction of OH radicals with *trans*-2-hexenal, with 2-methyl-2-butene (▲) and β-pinene (●) as the reference compounds. For clarity in presentation, the plot of β-pinene has been shifted up by 0.2 units.

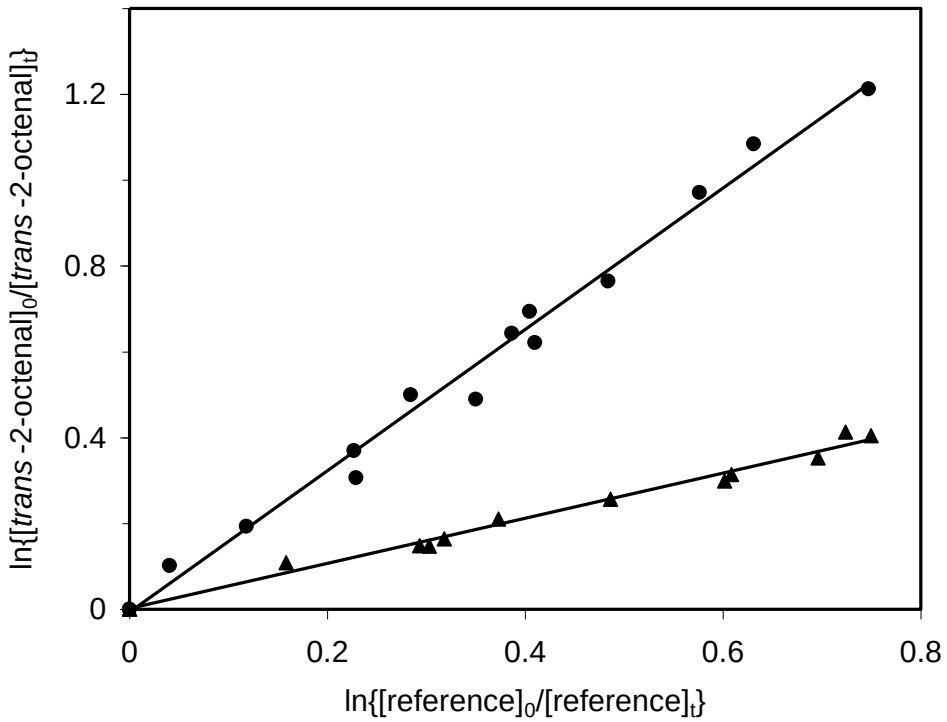


Figure 2.3. Plot of Equation 2.1 for the gas-phase reaction of OH radicals with *trans*-2-octenal, with β-pinene (▲) and butanal (●) as the reference compounds.

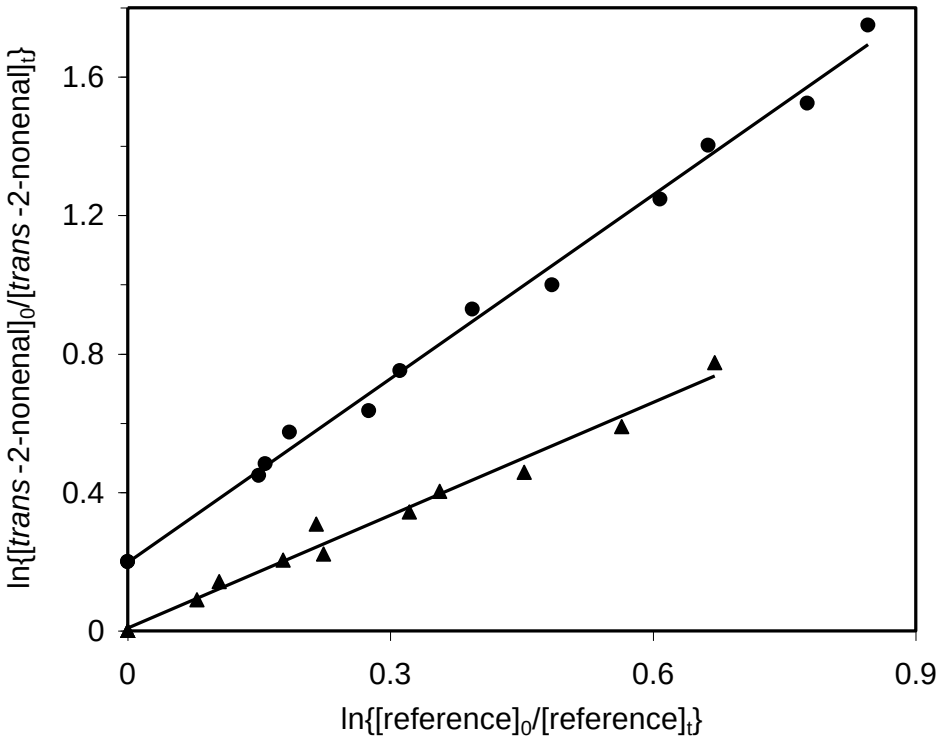


Figure 2.4. Plot of Equation 2.1 for the gas-phase reaction of OH radicals with *trans*-2-nonenal, with *trans*-2-hexenal (▲) and butanal (●) as the reference compounds. For clarity in presentation, the plot of *trans*-2-hexenal has been shifted up by 0.2 units.

Table 2.1. Rate Constant Ratio, $k_1/k_2$, and Rate Constant of Reaction of OH with *trans*-2-hexenal, *trans*-2-octenal and *trans*-2-nonenal

| **Target compound** | **reference** | **$k_1/k_2$[A]** | **Calculated Rate Constant[A,B] $k_1 \times 10^{12}$ $cm^3molecule^{-1}s^{-1}$** | **Calculated Recommended Rate Constant[A,C] $k_1 \times 10^{12}$ $cm^3molecule^{-1}s^{-1}$** |
|---|---|---|---|---|
| *trans*-2-hexenal | 2-methyl-2-butene | 0.452 ±0.054 | 39.3 ± 2.1 | 39.3 ±1.7 |
| | β-pinene | 0.530 ±0.036 | 39.4 ± 1.4 | |
| *trans*-2-octenal | butanal | 1.65 ±0.08 | 40.8 ± 3.3 | 40.5 ±2.5 |
| | β-pinene | 0.527 ±0.032 | 39.2 ± 1.3 | |
| *trans*-2-nonenal | butanal | 1.77 ±0.08 | 43.7 ± 3.5 | 43.5 ±3.0 |
| | *trans*-2-hexenal | 1.09 ±0.06 | 42.9 ± 2.6 | |

[A] The errors represent 2σ.

[B] The reference rate constants at 298 ±2 K are $k_{OH+2\text{-methyl-2-butene}} = 86.9 \times 10^{-12}$ $cm^3molecule^{-1}s^{-1}$, $k_{OH+beta\text{-pinene}} = 74.3 \times 10^{-12}$ $cm^3molecule^{-1}s^{-1}$, $k_{OH+butanal} = 24.7 \times 10^{-12}$ $cm^3molecule^{-1}s^{-1}$, $k_{OH+trans\text{-2-hexenal}}$ is determined in this work, the value of $39.4 \times 10^{-12}$ $cm^3molecule^{-1}s^{-1}$ was used here.

[C] The recommended value is determined by scaling all of the data for both references by the reference rate constant, and combining the data for all references on one graph.

For *trans*-2-hexenal, the rate constants determined by applying different reference compounds are in good agreement with each other. In addition, as can be seen in Table 2.2, if considering the errors associated with previous literature data, the value calculated in this work also agrees with previous work. In addition, the value presented here has a lower error than the work reported previously. Only the rate constant reported in Albaladejo *et al.*[69] is much lower than our result and the rate constants determined by other researchers. The potential reasons for the lower rate constant of Albaladejo *et al*. were discussed in Davis *et al.*[83].

This work presents the first published rate constants for *trans*-2-octenal and *trans*-2-nonenal. The rate constants determined in this work using different references for each of the two compounds are in good agreement with each other.

It is generally recognized that the OH radical reaction with unsaturated aldehydes will proceed via H atom abstraction from the –CHO functional group, OH addition to the double bond and H atom abstraction from the $–CH_2-$ and $–CH_3$ groups. Therefore, an increase in the rate constant is expected with an increase in carbon number for our three compounds of interest. An increase in the rate constants is observed in the data obtained in this work. However, the increase is small, particularly when considering the results of *trans*-2-hexenal as compared to those of *trans*-2-octenal. This provides additional evidence to support the conclusion that the $-CH_2-$ group in longer chain unsaturated oxygenated hydrocarbons does not significantly affect the rate constant, and the major reaction sites for this series of compounds are OH addition to the double bond and H atom abstraction from the –CHO functional group. This result is similar to the incremental increases in the OH rate constant of approximately $(1\text{-}3) \times 10^{-12}$ $cm^3$ $molecule^{-1}$ $s^{-1}$ for C8-C10 n-alkanes and C7-C10 1-alkenes that is due to the effects of added $-CH_2-$ groups[56, 72]. Further support arises when considering the product studies of some unsaturated aldehydes[60, 273].

Table 2.2. Summary of OH Rate Constant of C4-C10 *trans*-2-Unsaturated Aldehydes.

| **Unsaturated Aldehyde** | **$k_{OH+aldehyde}$ $\times 10^{12}$ $cm^3 molecule^{-1} s^{-1}$ [A]** | **Method[B,C]** | **Source** |
|---|---|---|---|
| *trans*-2-butenal | 33.5 ±3.0 | PLP-LIF | [60] |
| | 35.1 ±7.1 | PLP-LIF | [69] |
| | 35.0 ±4.0 | RR | [50] |
| | 33.0 ±6.0 | RR | [55] |
| | 38.8 | | Estimated[D] |
| *trans*-2-pentenal | 23.5 ±3.2 | PLF-LIF | [69] |
| | 43 ±6 | PLP-LIF | [83] |
| | 39.7 | | Estimated[D] |
| *trans*-2-hexenal | 39.3 ± 2.1 | RR | This work |
| | 39.4 ± 1.4 | RR | This work |
| | 29.5 ±4.5 | PLF-LIF | [69] |
| | 44.1 ±9.4 | RR | [51] |
| | 44 ± 5 | PLP-LIF | [83] |
| | 46.8 ± 10.0 | PLP-LIF | [271] |
| | 41.1 | | Estimated[D] |
| *trans*-2-heptenal | 24.5 ±3.0 | PLF-LIF | [69] |
| | 44 ±7 | PLF-LIF | [83] |
| | 42.5 | | Estimated[D] |
| *trans*-2-octenal | 40.8 ± 3.3 | RR | This work |
| | 39.2 ± 1.3 | RR | This work |
| | 44.0 | | Estimated[D] |
| *trans*-2-nonenal | 43.7 ± 3.5 | RR | This work |
| | 42.9 ± 2.6 | RR | This work |
| | 45.3 | | Estimated[D] |

[A] The rate constant is at 298 ±2K. [B] Pulsed laser photolysis coupled with laser induced fluorescence. [C] Relative rate constant technique. [D] The rate constant that is estimated using the structure activity relationship[96].

### 2.3.2 Comparison with the Rate Constant Estimated by SAR

In comparing the calculated rate constants of *trans*-2-hexenal, *trans*-2-octenal and *trans*-2-nonenal with the experimental rate constants determined in this work, it appears as if the rate constants estimated by SAR are slightly larger than the experimental rate constants. This can be clearly seen in Figure 2.5, where the dash line is the linear trend of the OH rate constants estimated using the SAR. The deviation between the SAR-estimated and the experimentally determined rate constants of these series of organic compounds is within 15%. If the errors of the experimentally determined rate constant are considered, most error bars cross the dashed line. Therefore, the SAR estimation of this series of unsaturated aldehydes is reasonably good. If one does an average of the data in Figure 2.5 including only C5 and higher rate constant values (since the points do not change much), an approximate rate constant can be obtained of $42.5 \times 10^{-12} cm^3 molecule^{-1} s^{-1}$ for these larger unsaturated aldehydes. This may be useful in mechanism development for air quality modeling efforts.

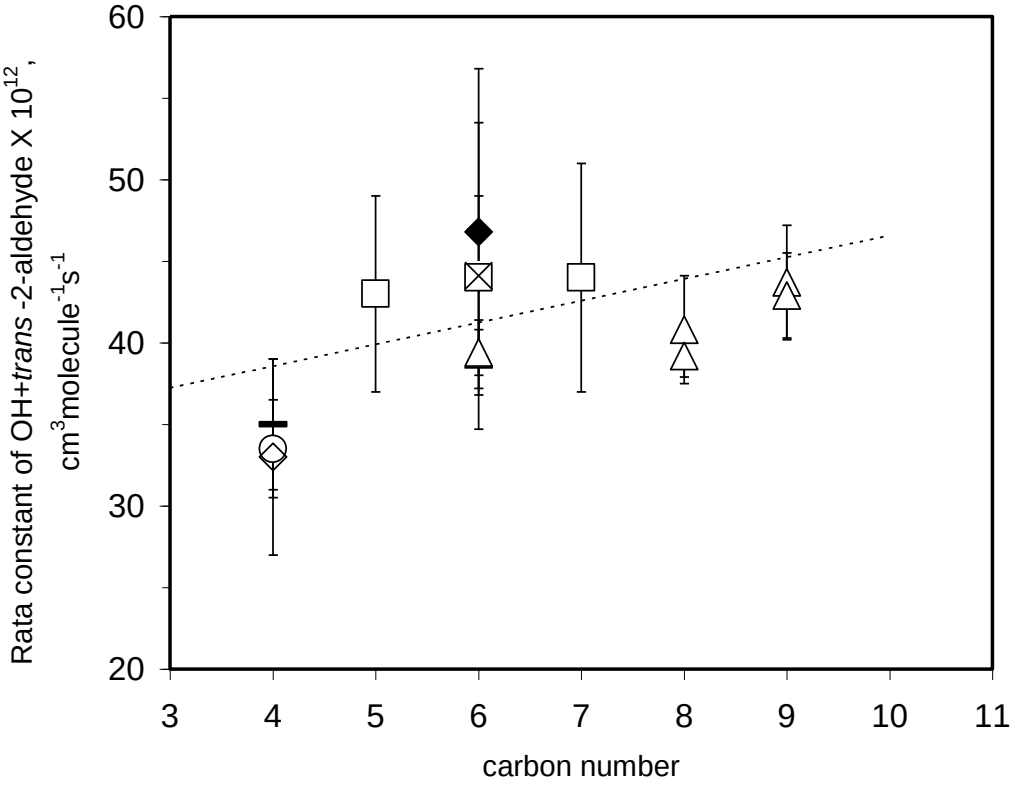


Figure 2.5. Plot of OH rate constants of C4-C10 *trans*-2-unsaturated aldehyde against the carbon number. The experimental values are from this work and previous literature (summarized in Table 2.2). The dotted line represents the values predicted by the SAR[14]. The points are as follows: ○, Reference [60]; —, Reference [50]; ◊, Reference [55]; □, Reference [83];◆ , Reference [271]; ×, Reference [51]; Δ, this work. The data of Albaladejo *et al*.[69] are not included here.

### 2.3.3 Recommended Rate Constants and Lifetimes

By averaging the values obtained using the different rate constants, the following recommendations are made for the OH reactions with *trans*-2-hexenal, *trans*-2-octenal and *trans*-2-nonenal: $(39.3 \pm 1.7) \times 10^{-12}$ $cm^3molecule^{-1}s^{-1}$, $(40.5 \pm 2.5) \times 10^{-12}$ $cm^3molecule^{-1}s^{-1}$, and $(43.5 \pm 3.0) \times 10^{-12}$ $cm^3molecule^{-1}s^{-1}$, respectively. Using the daytime average ambient tropospheric concentrations of OH radicals of $1.6 \times 10^6$ molecule $cm^{-3}$ [274], and the recommended rate constants

determined using the two different references for each target compound studied in this work, the calculated tropospheric lifetimes with respect to OH radical reaction are: 4.4 hours for *trans*-2-hexenal, 4.3 hours for *trans*-2-octenal and 4.0 hours for *trans*-2-nonenal. Using the average rate constant for the reactions of OH radicals with C5 or higher *trans*-2-aldehydes, i.e. $42.5 \times 10^{-12} cm^3 molecule^{-1} s^{-1}$, the atmospheric lifetime with respect to OH radical reaction for these species is 4.1 hours. Since the aldehydes studied are unsaturated, they may also react with ozone and the nitrate radical, thus decreasing the overall atmospheric lifetimes of the compounds.

# CHAPTER 3

# THE INTERACTIONS BETWEEN VOCS AND IONIC LIQUID SURFACES: A COMPUTATIONAL AND EXPERIMENTAL STUDY

## 3.1 Introduction

Sensors have been widely used in many aspects of environmental monitoring[275, 276], as well as in industry[277], medical monitoring[278] and traffic[279]. Gas-phase sensors for the detection of alcohols are very important since these classes of compounds are widely used in people's life, including in the workplace, medicine, the food industry, and the automotive fuel industry[173, 280, 281]. Alcohols are volatile organic compounds that may have an adverse impact on human health. Many diseases, such as eyesight disturbance and even nerve diseases are caused by long-time exposure to alcohols[282]. Therefore, it is extremely important to develop sensors to detect alcohol vapors and protect our environment and human health. Currently, many kinds of gas-phase alcohol sensors have been developed, including metal oxide nanoparticle based gas sensors[170, 173, 182-186] and polymer based gas sensors[203]. One of the drawbacks of the sensors that currently exist is that they are not very selective to alcohol vapors since the materials that are used also interact with various other types of gases in the environment.

Ionic liquids are a class of relatively novel solvents[283, 284]. They are attracting increased attention in many areas because of their unique properties[283]. The applications of ionic liquids include organic synthesis[285, 286], electronic devices[287-292] and analytical chemistry[293-297]. Ionic liquids and their modifications have also been applied as sensing materials[282, 298-301]. Ionic liquids have good

stability, negligible vapor pressure and tunable viscosity[284, 298, 302, 303]. These properties make ionic liquids environmental-friendly solvents. In addition, ionic liquids are also good supports for many kinds of solvent-solute interactions[282, 304]. When considering the reversibility (cleaning) of a sensor, a quartz crystal microbalance sensor with ionic liquid coatings have been shown to have a faster response time as compared to polymers or other solid coatings[304]. These properties make ionic liquids good candidates for novel sensor platforms.

In this work, the interactions between ionic liquids and different kinds of volatile organic compounds (VOCs) were investigated through closely coupled computational chemistry and experimental techniques. The three ionic liquids studied in this work are halogen anion containing imidazolium ionic liquids. Their molecular structures are shown in Figure 3.1. It has been suggested, using computational tools, that the Cl-containing imidazolium ionic liquid is selective to methanol as compared to dimethyl ether and propane[305-307]. Thus, the goal was to examine the behavior of other VOCs using computations and to experimentally verify these results. The types of VOCs tested include alcohols, aldehydes, a ketone, alkanes, alkenes, an alkyne, and an aromatic hydrocarbon. To our knowledge, this is the first combined computational and experimental study of the interactions between ionic liquids and these various classes of VOCs. The information that is obtained through this combined computational and experimental study will help researchers choose the best ionic liquid to serve as a thin film layer in the development of a novel alcohol vapor sensor.

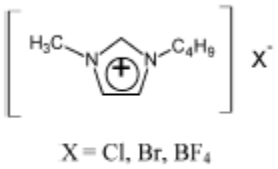


Figure 3.1. Molecule structure of the ionic liquids studied in this work.

### 3.2 Computational Details

The initial set of calculations was performed with the Gaussian 03 package of programs. First, the geometries of each ionic liquid and each representative volatile organic compound were individually optimized using a Hartree-Fock method and a 6-31G (d) basis set. Subsequently, the geometries of the ionic liquid – VOC pairs were optimized. Additional calculations were then performed to determine the thermodynamic parameters. The ionic liquids studied in this work included 1-butyl-3-methylimidazolium chloride ($C_4$mimCl), 1-butyl-3-methylimidazolium bromine ($C_4$mimBr) and 1-butyl-3-methylimidazolium tetrafluoroborate ($C_4$mim$BF_4$). The classes of VOCs studied were alcohol, aldehyde, ketone, alkane, alkene, alkyne and aromatic hydrocarbon. The test compounds, listed according to their VOC class, appear in Table 3.1.

Table 3.1. VOCs Studied in the Computational Work

| **Class of VOC** | **Compounds Studied** |
|---|---|
| alcohol | methanol, ethanol, 2-methyl-1-propanol, 3-methyl-1-butanol |
| aldehyde | formaldehyde, acetaldehyde, butanal |
| ketone | acetone |
| alkane | ethane, propane |
| alkene | ethylene, *cis*-2-butene |
| alkyne | acetylene |
| aromatic hydrocarbon | toluene |

To verify the computational technique that was used in this study, an initial computation was conducted as a comparison with literature data. Xu *et al*[282] studied the interaction between $C_4$mimCl and ethanol using a Hartree-Fock method and 6-31G (d) basis set. A computational study of the interaction between $C_4$mimCl and ethanol was also carried out within our group using the same method and basis set, and results were compared with the results of Xu *et al*[282].

Different initial positions of the VOC in relation to the ionic liquid were tested in the computational studies in order to examine whether the initial placements of the molecules affected the results.

In addition to the Hartree-Fock (HF) calculations, calculations using density functional theory (DFT) were also performed on the ionic liquid/VOC combination to examine whether choosing a different computational method would alter the predictions. Two types of calculations were performed, one using M05-2X/6-311++G(d,p) and the other using CBS-QB3// M05-2X/6-311++G(d,p). CBS-QB3 is assumed to give chemical accuracy ($\pm$ 1 kcal/mol). M05-2X is one of

the newest DFT methods that is assumed to correctly reproduce weak interactions[308].

The initial computational work that was carried out considered only a single VOC interaction with a single ionic liquid molecule. However, in order to provide more information about the influence of multiple ionic liquid molecules on the thermochemical data, additional computational studies were carried out with methanol, acetaldehyde and acetylene interacting with two ionic liquid species. Two configurations for the ionic liquid molecules were tested: sequential and stacked, as detailed subsequently. These DFT computations were performed using M05-2X and the 6-31+g(d,p) basis set.

In all cases, full geometry optimizations and frequency calculations were performed. The local minima were identified by the number of imaginary frequencies (NIMAG = 0).

**3.3 Experimental Details**

A cylindrical chamber of 2 Liters in volume was used as the exposure chamber. A zinc selenide crystal trough with a thin film of the ionic liquid was placed in the exposure chamber and exposed to a flow of VOC vapor originating from a Teflon bag. Known amounts of either an individual VOC or VOC mixtures were prepared in an 80 L Teflon bag through the vaporization of the liquid VOCs. Microliter quantities of the liquid VOCs were injected using a syringe (Hamilton Company, Reno, NV) into a small vaporization chamber containing a stream of purified air that was generated using a zero air generator (Perma Pure LLC., Toms River, NJ). The flow rate of zero air through the vaporization chamber and into

the bag was controlled by a mass flow controller (Omega Engineering, Inc., Stamford, CT) that was placed upstream of the vaporization chamber. Two of the compounds, propane and *cis*-2- butane were introduced into the bag via a custom designed evacuable glass manifold system and flushed into the Teflon bag with zero air. Concentrations of organics were at the ppm level. (Note that lower concentrations were not used since this was a proof of concept experiment.)

The bag containing the VOC(s) was connected to the exposure chamber containing the ionic liquid surface inside. A pump was used to pull the gas into the chamber. The valves were closed after introduction of the gas to the chamber (in order to form a closed environment), and the gas was allow to remain in the exposure chamber for 10 minutes.

The ionic liquid used in the experiments was $C_4$mimCl (Sigma Aldrich, ≥ 99.0%, dry) and was used in a thin film configuration. To generate the thin film, a solution of the ionic liquid was made by dissolving 0.01g of $C_4$mimCl dry powder in chloroform. The solution was placed onto a zinc selenide crystal trough, and the chloroform was subsequently evaporated. The thickness of the $C_4$mimCl film is about 50 μm.

All compounds were purchased from Sigma-Aldrich with the following stated purities: ethanol (99.5+%), 2-methyl-1-propanol (99.5%), 3-methyl-1-butanol (≥ 99%), acetaldehyde (≥ 99%), butanal (≥ 99.0%),acetone (99.5+%), propane (98%), *cis*-2-butene (99+%), acetylene (99.5%) and toluene (99.8%), chloroform (≥ 99 %), and $C_4$mimCl (≥ 99.0%) .

The interactions between $C_4$mimCl and either an individual VOC or a mixture of VOCs were investigated using Fourier-transform infrared spectroscopy (Thermo Nicolet FTIR 6700) with attenuated total reflectance (ATR). The ionic liquid thin film in the trough was analyzed before and after exposure to the VOC using ATR-FTIR employing a mercury cadmium telluride (MCT) detector and OMNIC® software set to collect 16 scans at 0.5 $cm^{-1}$resolution. A Teflon cap was placed on the trough to minimize loss of the sample when transferring the trough with the ionic liquid between the FTIR and the exposure chamber. Background experiments were carried out to determine whether air had any influence on the system by exposing the ionic liquid thin film to a flow of zero air without VOC. The samples prior and subsequent to zero air exposure were also analyzed by ATR-FTIR.

### 3.4 Results and Discussion

#### 3.4.1 Computational Results

The optimized structure of $C_4$mimCl is presented in Figure 3.2. The geometry optimization results of the interactions between $C_4$mimCl with methanol, ethanol, formaldehyde, ethane, and ethylene are presented in the appendix, Figure A-1, as examples of the calculations between $C_4$mimCl and selected VOCs studied in this work. The interaction length is defined and used in this paper to indicate the distance between an atom in the ionic liquid and an atom in the target VOC. Values of the calculated interaction lengths are presented in the appendix, Table A-1. The interaction between $C_4$mimCl and ethanol was initially studied as a comparison to literature[282]. The most likely interactions between

$C_4$mimCl and alcohols, because of calculated interaction lengths, are the H•••Cl and O•••H, where the first atom is from the alcohol and the second atom is from the ionic liquid. These interaction lengths are shorter than the distances between other atoms in $C_4$mimCl and atoms in the alcohol. The results obtained in this study for the $C_4$mimCl / ethanol system for the H•••Cl and O•••H interaction lengths are within 5% of the interaction lengths reported by Xu *et al*[282]. Therefore, our computational calculations are in good agreement with the only other published computational study found for the $C_4$mimCl / ethanol system.

The shortest distances between atoms in $C_4$mimCl and atoms in the other VOCs studied were determined and are also listed in the Appendix, Table A-1. The interaction lengths between $C_4$mimCl and the alcohols studied are the shortest amongst all classes of VOCs examined. This suggests that $C_4$mimCl is potentially more likely to interact with alcohols as compared to aldehydes, ketones, alkanes, alkenes, alkynes or aromatic hydrocarbons. Here we correlate a shorter interaction length (and hence a higher likelihood of $C_4$mimCl of interacting with a compound) to a higher selectivity of the ionic liquid to that compound. Examination of the interaction lengths thus suggests that $C_4$mimCl is more selective towards alcohols than aldehydes, ketones, alkanes, alkenes, alkynes or aromatic hydrocarbons.

Different initial positions of the VOC in relation to the ionic liquid were tested in the computational studies. The interaction lengths are slightly different. However, the observed trends were identical.

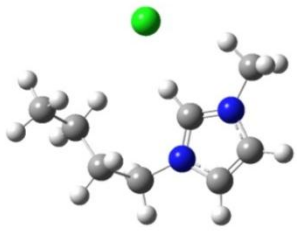

Figure 3.2. Optimized geometry of $C_4$mimCl.

The interactions of methanol with $C_4$mimBr and $C_4$mim$BF_4$ ionic liquids were also studied in addition to $C_4$mimCl. Geometry optimizations were performed with methanol in the presence of either $C_4$mimBr or $C_4$mim$BF_4$. The interaction positions and lengths are presented in the appendix, Figures A-2, A-3 and Table A-2. The interaction lengths (where the first atom is from the alcohol and the second atom is from the ionic liquid) of H•••Br and O•••H for methanol and $C_4$mimBr are longer than the interaction lengths of H•••Cl and O•••H in the case of methanol and $C_4$mimCl. This suggests that there is a higher possibility for methanol to interact with $C_4$mimCl as compared to $C_4$mimBr. The interaction length data calculated for methanol and $C_4$mim$BF_4$ make it challenging to make a prediction (based only on interaction lengths) of whether methanol is more or less likely to interact with $C_4$mim$BF_4$ as compared to the other two ionic liquids. This arises since the H•••F distance is relatively small and the O•••H distance is relatively large.

In addition to performing a geometry optimization calculation, thermochemical data were also obtained. Calculated enthalpies and Gibbs

energies for the interactions are listed in Table 3.2. The energy data for interactions of $C_4$mimCl with the alcohols are the most exothermic of all of the data obtained. These results indicate that the interactions of $C_4$mimCl with alcohol compounds are more energetically favorable as compared to the interactions with other VOCs, and suggest a higher potential for $C_4$mimCl to interact with methanol (and other alcohols). These results are consistent with the interaction length data (Appendix Table A-1). It is also important to note that the data in Table 3.2 obtained using the DFT calculations support the observed trends. Thus, although the absolute numbers are different, the predicted trends are similar to those produced using the HF calculations, i.e. that interaction of the alcohol with the ionic liquid is more thermodynamically favored.

Given the relatively large negative data (in terms of Gibbs energies) obtained for the aldehydes/ketone, one might also expect an interaction to occur between these VOCs and the ionic liquid. To further test this hypothesis, VOC (i.e. methanol, acetaldehyde, and acetylene) interaction data were obtained using two ionic liquid molecules. Two different configuration models, as seen in Figure 3.3, were tested: sequential and stacked. The two $C_4$mimCl sequential model resulted in a Gibbs energy of interaction for the two ionic liquids of -5.25 kcal/mol, as calculated with M05-2X / 6-31+g(d,p), while the two $C_4$mimCl stacked model resulted in a Gibbs energy of interaction of -14.4 kcal/mol. The two $C_4$mimCl stacked model suggests that a cavity is formed. Previously published work has suggested that ionic liquids form cavities that are of a sufficient size to accommodate the interacting analyte[309]. The energy data

reported in Table 3.2 suggest that the inclusion of more ionic liquid molecules in the computational system increases the values of the calculated thermodynamic parameters. However, the values obtained or the aldehydes/ketones are still negative but very small and within the expected errors in quantum chemical calculations. The two ionic liquid model results are further discussed in the experimental section.

The calculated energy of interaction between methanol and $C_4$mimCl is more exothermic as compared to the methanol / $C_4$mimBr or and methanol / $C_4$mim$BF_4$ systems, thus suggesting that methanol is more likely to interact with $C_4$mimCl than $C_4$mimBr or $C_4$mim$BF_4$. The interaction between methanol and $C_4$mim$BF_4$ is not as exothermic and exergonic. Thus, although the short interaction lengths reported in Table A-2 (Appendix) for the H-F interaction suggest an interaction, the thermochemical calculations suggest that $C_4$mim$BF_4$ is less likely to interact with methanol. The shorter H-F length as compared to H-Cl may simply be explained by the smaller radius of the fluoride anion in C4mim$BF_4$ as compared to the chlorine anion in $C_4$mimCl.

Table 3.2. Thermochemical Data of the Interactions between Ionic Liquids and VOCs Using Different Computational Techniques

| **Interacting Compounds** | **ΔH [a, b], kcal/mol** | **ΔG [a, b], kcal/mol** |
|---|---|---|
| $C_4$mimCl + methanol | -14.71 | -7.56 |
| | -14.90 [c] | -5.80 [c] |
| | -14.36 [d] | -5.25 [d] |
| 2$C_4$mimCl + methanol | -13.39[e] | -4.34[e] |
| $C_4$mimCl + ethanol | -14.44 | -7.41 |
| $C_4$mimCl + isopropanol | -15.12 | -8.04 |
| $C_4$mimCl + 2-methyl-1-propanol | -14.45 | -6.98 |
| $C_4$mimCl + 3-methyl-1-butanol | -14.85 | -7.40 |
| $C_4$mimCl + formaldehyde | -11.88 | -4.24 |
| $C_4$mimCl + acetaldehyde | -11.83 | -4.39 |
| 2$C_4$mimCl + acetaldehyde | -10.77[e] | -0.21[e] |
| $C_4$mimCl + butanal | -11.80 | -5.98 |
| $C_4$mimCl + acetone | -12.31 | -3.84 |
| $C_4$mimCl + ethane | -2.51 | -0.22 |
| $C_4$mimCl + propane | -2.90 | 0.01 |
| $C_4$mimCl + ethylene | -4.09 | 0.37 |
| | -4.51 [c] | 0.17 [c] |
| $C_4$mimCl +*cis*-2-butene | -3.75 | 1.81 |
| $C_4$mimCl + acetylene | -8.21 | -2.64 |
| | -6.60 [c] | 0.09 [c] |
| 2$C_4$mimCl + acetylene | -5.89[e] | -0.17[e] |
| $C_4$mimCl + toluene | -6.93 | 1.73 |
| $C_4$mimBr + methanol | -13.51 | -4.30 |
| $C_4$mim$BF_4$ + methanol | -7.88 | 1.55 |

a. One molecule of the target compound interacting with one molecule of the ionic liquid was used to calculate the energy of the interaction using the HF technique, unless otherwise stated.

b. The thermochemical data are at 1 atmosphere and 298.15K.

c. DFT calculation using M05-2X/6-311++G(d,p)

d. DFT calculation using CBS-QB3// M05-2X/6-311++G(d,p)

e. DFT calculation using M05-2X / 6-31+g(d,p) and two ionic liquids in the stacked configuration.

(A)

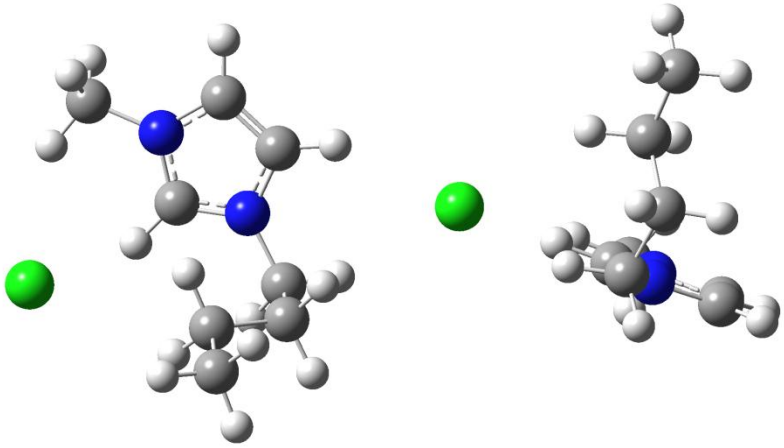

(B)

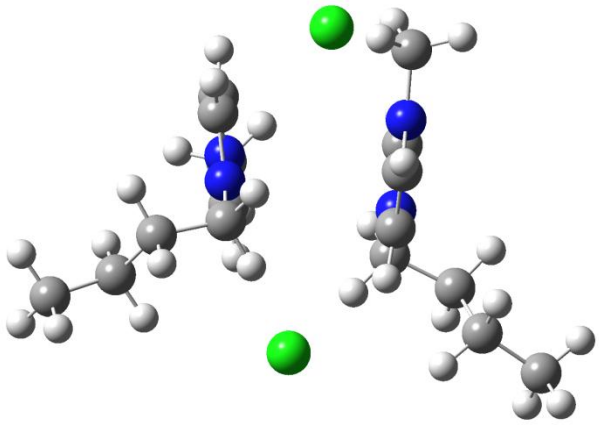

Figure 3.3. Two ionic liquid models: (A) Sequential $C_4$mimCl, (B) Stacked $C_4$mimCl.

The interactions between ionic liquids and VOCs can also be explained by considering the electronic structures. The charge distributions within different VOC molecules are presented in Figure 3.4. The oxygen atoms in the molecules of the ethanol, acetaldehyde, and acetone have negative charges. These negative charge centers will approach the positively charged hydrogen atoms of $C_4$mimCl. Because the oxygen atom of the ethanol is more negatively charged than the oxygen atom of either the acetaldehyde or the acetone, the oxygen atom of the

ethanol is more likely to be attracted to the positively charged hydrogen atom of $C_4$mimCl. Thus, the O•••H interaction length for the ethanol system is expected to be shorter than that in the acetaldehyde/ $C_4$mimCl or the acetone / $C_4$mimCl, and indeed, as seen in Table A-1 (Appendix), it is. In addition, the hydrogen in the –OH group of the ethanol molecule is more positively charged than the hydrogen atoms of acetaldehyde or acetone. The highly positively charged hydrogen in ethanol is more likely to interact with the chlorine atom in the $C_4$mimCl molecule, as can be seen by the shorter H•••Cl interaction length for the ethanol / $C_4$mimCl system. The alkanes, alkenes, alkynes and aromatic hydrocarbons studied contain positively charged hydrogens (see the electronic structure of propane as an example). These hydrogen atoms have a less positive charge as compared to the charge of hydrogen in the –OH group of ethanol (or other alcohols). Therefore, the hydrogen atoms of alkanes, alkenes, alkynes, or aromatic hydrocarbons are not expected to have good interactions with the chlorine atom of $C_4$mimCl. This result is supported by the relatively longer H•••Cl interaction lengths, as seen in Table A-1 (Appendix).

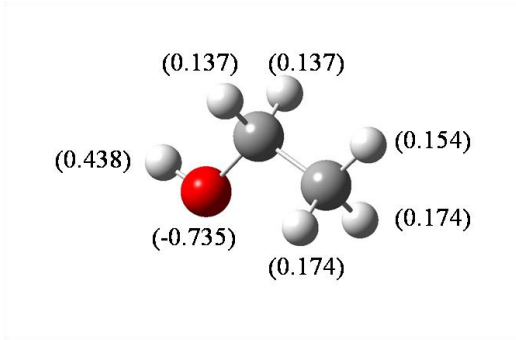


ethanol

(a)

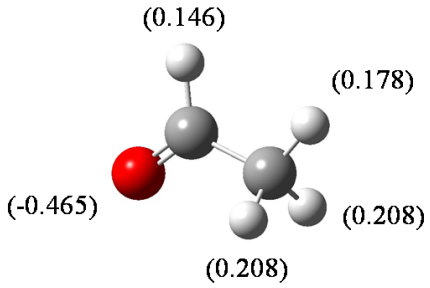


acetaldehyde

(b)

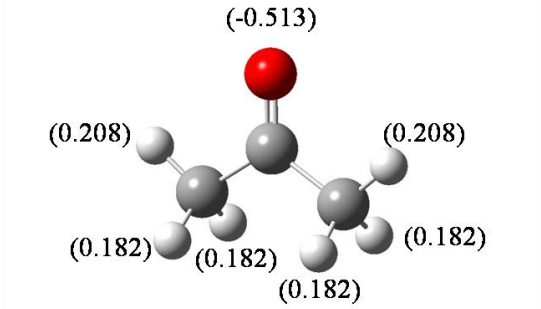


acetone

(c)

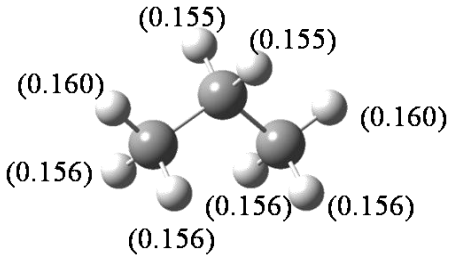


propane

(d)

Figure 3.4. Elementary charge distributions within selected VOCs studied. (a) Methanol, where the charge on the oxygen is -0.735 and the charge on the hydrogen in the –OH grounp is +0.438. (b) Acetaldehyde, where the charge on oxygen is -0.465 and the charges on the hydrogen range from +0.146 to +0.208. (c) Acetone, where the charge on the oxygen is -0.513 and the charges on the hydrogen range from +0.182 to +0.208. (d) Propane, where the charges on the hydrogen range from +0.155 to +0.160.

### 3.4.2 Experimental Results

The background experiments showed that there were no differences in the infrared spectra prior or subsequent to the exposure of $C_4$mimCl to zero air.

The infrared spectra of the interactions between $C_4$mimCl and ethanol, 2-methyl-1-propanol, and 3-methyl-1-butanol are shown in Figures 3.5, 3.6, and 3.7, respectively. In Figure 3.5, the interaction of ethanol with $C_4$mimCl led to new peak formation centered at 1050 $cm^{-1}$. In Figure 3.6, the interaction of 2-methyl-1-propanol with $C_4$mimCl led to the new peak formations centered at 1006 $cm^{-1}$ and 1048 $cm^{-1}$. In Figure 3.7, the interaction of 3-methyl-1-butanol with $C_4$mimCl led to new peak formations centered at 1010 $cm^{-1}$ and 1060 $cm^{-1}$. Comparing the spectra obtained in this work to the infrared spectra from our internal library of gas-phase standards as well as the National Institute of Standards and Technology (NIST) reference database[44] for gas-phase compounds, the new peaks formed in Figures 3.5-3.7 are characteristic of ethanol, 2-methyl-1-propanol and 3-methyl-1-butanol, respectively, and do not appear to be shifted from the gas-phase spectra. The new peak formations in the infrared spectra after exposure to the gas-phase alcohols demonstrate that ethanol, 2-methyl-1-propanol and 3-methyl-1-butanol interact with $C_4$mimCl.

If hydrogen bonding occurs, a shift in the infrared spectra between the VOC in the gas-phase and the VOC interaction with the ionic liquid would be expected at higher frequencies. This result has been seen in previously published work[304, 310]. However, since ATR-FTIR only probes surfaces, we could only perform a direct comparison between the ionic liquid surface before and after

exposure to the gas. For the case of methanol, the spectra show formation of a new spectral feature at 3250 $cm^{-1}$. Based on the literature data, this new spectral feature corresponds to the –OH stretch of condensed phase methanol[310]. The corresponding –OH stretch of methanol in the gas-phase is centered at approximately 3700 $cm^{-1}$ [46]. Thus, interaction of the methanol with the ionic liquid surface results in a red shift of approximately 450 $cm^{-1}$. Other alcohols studied in the laboratory exhibited this same red shift. The red shift is proportional to the strength of the H bonding. For simple condensation of methanol, a shift of 350 $cm^{-1}$ is observed [310]. In the case of methanol interacting with the ionic liquid surface, the shift is 100 $cm^{-1}$ larger, thus suggesting stronger H bonding because of the presence of the ionic liquid. This laboratory result is supported by the computational data for the methanol interaction with the stacked two $C_4$mimCl model as compared to gas-phase methanol. Specifically, the stacked two ionic liquid/methanol model predicts an –OH stretch feature at 3266.1 $cm^{-1}$ and the gas-phase methanol model predicts a feature at 3700.4 $cm^{-1}$, resulting in a red shift of 434.3 $cm^{-1}$ upon condensation. These frequencies have been adjusted by the scale factor of 0.9386, a factor that is specific to the method and basis set used[311] .The frequency shift determined computationally (i.e. 434.3 $cm^{-1}$) is within 3.5% of the frequency shift that was detected in the laboratory.

The interactions between $C_4$mimCl and aldehydes, a ketone, an alkane, an alkene, an alkyne or an aromatic hydrocarbon were also studied by ATR-FTIR by taking the IR spectra before and after exposure of the $C_4$mimCl thin film to the VOC. No changes in the spectra were noticed after exposure of the ionic liquid to

these classes of compounds. The infrared data for toluene exposure to $C_4$mimCl is presented in Figure 3.8 as an example. For simplicity, only two spectral regions where peaks for toluene might be expected to arise are shown. However, it is important to note that the entire infrared spectral range analyzed using ATR-FTIR and the MCT detector used in this work was examined for changes, and no changes were detected. This same result applied to the ketone, aldehydes, alkanes, alkenes and alkyne studied.

As seen in Figure 3.9, new peaks were detected after exposing the $C_4$mimCl to a VOC mixture that was comprised of gas-phase 2-methyl-1-propanol, acetaldehyde, acetone and toluene. The new peaks are only characteristic of the alcohol, i.e. the 2-methyl-1-propanol. In addition, the remainder of the spectrum was examined for changes. However, no additional peaks corresponding to the other compounds appeared in the IR spectrum. Therefore, in the infrared region, $C_4$mimCl is able to selectively respond to alcohols as compared to other classes of VOCs studied in this work.

Table 3.3 summarizes all of the experimental results. This table demonstrates that there are only new peak formations in the IR spectra for exposure of $C_4$mimCl to alcohols or a VOC mixture containing an alcohol. The spectral changes observed by exposing $C_4$mimCl to the VOC mixture are identical to those observed when exposing $C_4$mimCl to only 2-methyl-1-propanol. Therefore, in the IR region, $C_4$mimCl is not only able to respond to single alcohol exposure, but is also able to respond to the alcohol in a complicated VOC

mixture. This result strongly suggests that $C_4$mimCl is a highly selective material for the development of infrared-based optical sensors for alcohols.

Based on the thermochemical data of the one ionic liquid computational model, we might have expected carbonyl containing compounds to interact with the ionic liquids in the experimental studies. However, this was not detected in the ATR-FTIR studies. Reasons for this phenomenon are likely due to the nature of the interaction and the concentrations used. Figure 3.10 shows the interactions of acetaldehyde and methanol with the stacked two $C_4$mimCl model. The computational results in Figure 3.10 show that the hydrogen atom in the –OH group of methanol is much closer to the cavity region containing the Cl groups of the ionic liquids. The interaction length is 2.12 Angstroms, a very short distance considering the large ionic radius of chlorine, and the Gibbs energy change (reported in Table 3.2) that is strongly negative. In addition, the frequency shifts reported for the alcohols suggest that there is an interaction with the –OH group for the alcohols. On the other hand, the results depicted in Figure 3.10 indicate that a similar kind of interaction is missing in the complex between acetaldehyde and the ionic liquid since the distance between the chlorine anion and the a hydrogen is much larger at 2.8 Angstroms. This is supported by the near zero Gibbs energy change reported in Table 3.2 for the two ionic liquid system. These results suggest that the two ionic liquid model is more representative of actual experimental conditions. An additional explanation comes when considering the calculated Gibbs energies of interaction for methanol and acetaldehyde for the two ionic liquid systems. The fact that both of the calculated DG values are

negative suggests that both processes are spontaneous under standard conditions. Using the DG data we can calculate the equilibrium constant based on concentration, i.e. $Kc = \frac{[VOC/C_4\text{mimCl complex}]}{[VOC][C_4\text{mimCl}]}$, for both processes, assuming the following reversible interaction:

$$\text{VOC} + \text{C}_4\text{mimCl} \leftrightarrow \text{VOC/C}_4\text{mimCl complex}$$

The values of $K_c$ (in L/mol) for the methanol/$C_4$mimCl and acetaldehyde/ $C_4$mimCl interaction were calculated to be $3.72*10^4$ and 34.9, respectively. These results also imply that both processes are thermodynamically favored. However, given the ppm levels of VOC ($2.0 \times 10^{-5}$ mol/L) used in the experiments, the ratio of $\frac{[\text{methanol}/C_4\text{mimCl complex}]}{[C_4\text{mimCl}]}$ is expected to be on the order of 1, whereas the ratio of $\frac{[\text{acetaldehyde}/C_4\text{mimCl complex}]}{[C_4\text{mimCl}]}$ will be on the order of $10^{-2}$. These results suggest that complexation is favored for methanol (and the alcohols in general), and not favored for the acetaldehyde under the experimental conditions used. Indeed, the laboratory work shows no evidence for the interactions of the aldehydes with the $C_4$mimCl. Therefore there is good agreement between the experiments and calculations, particularly the calculations that involve the double ionic liquid model.

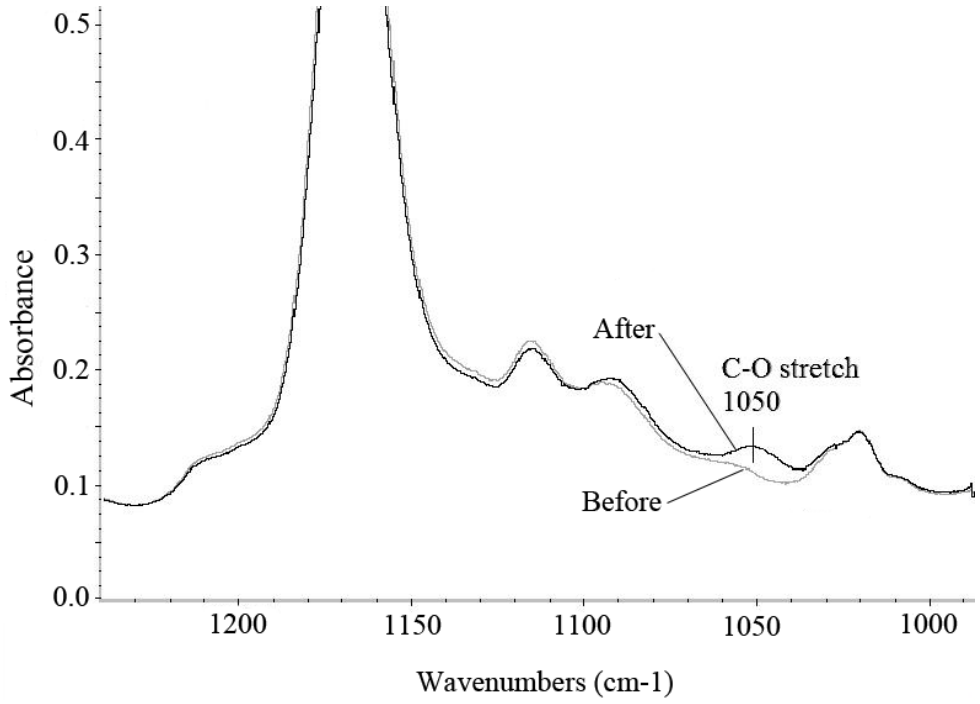


Figure 3.5. ATR-FTIR spectra of $C_4$mimCl prior to and subsequent to gas-phase ethanol exposure in the region of 980 $cm^{-1}$ to 1240 $cm^{-1}$.

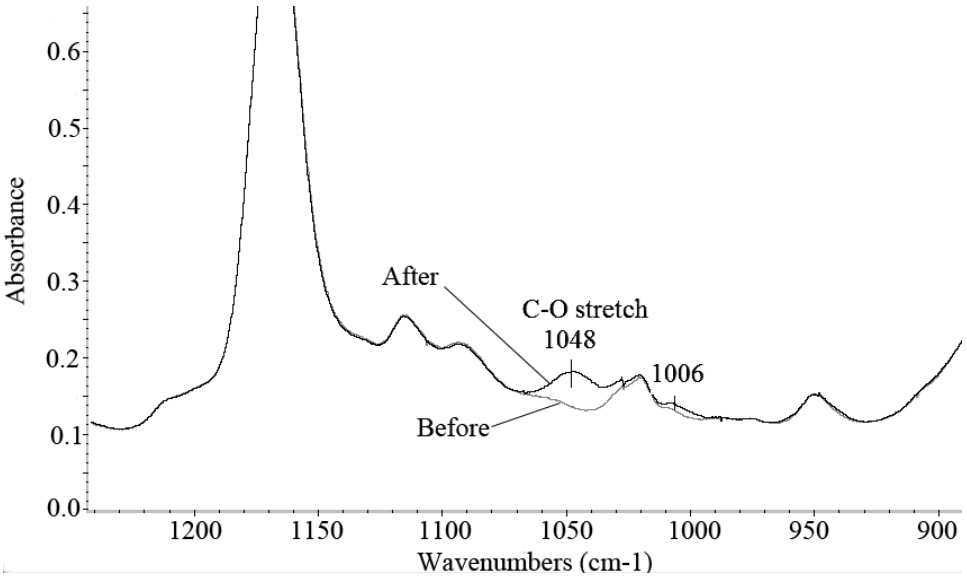


Figure 3.6. ATR-FTIR spectra of $C_4$mimCl prior to and subsequent to gas-phase 2-methyl-1-propanol exposure in the region of 900 $cm^{-1}$ to 1240 $cm^{-1}$.

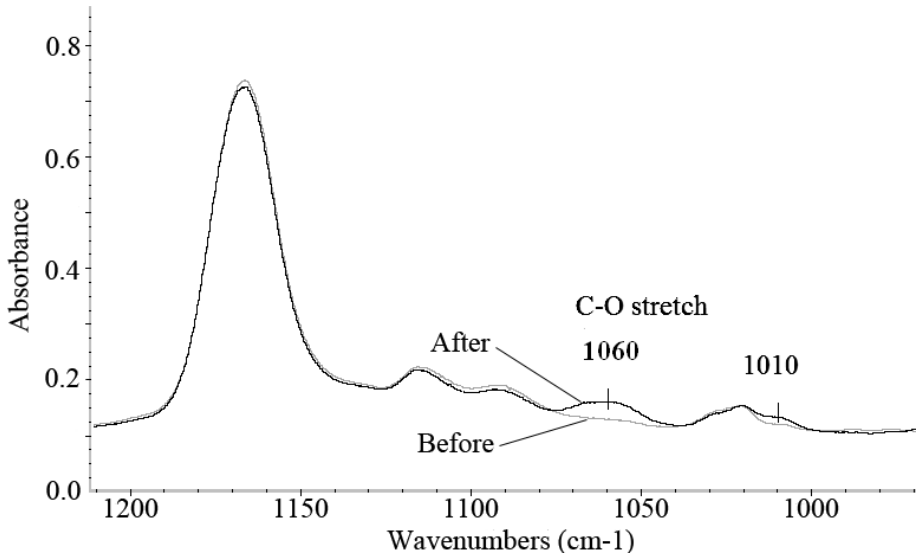


Figure 3.7. ATR-FTIR spectra of $C_4$mimCl prior to and subsequent to gas-phase 3-methyl-1-butanol exposure in the region of 960 $cm^{-1}$ to 1210 $cm^{-1}$.

Table 3.3. Summary of the New ATR-FTIR Spectral Features Detected upon Exposure of $C_4$mimCl to Gas-Phase VOCs

| **Tested VOCs** | **New Feature(s) Detected, $cm^{-1}$** | **O-H Stretch Feature, $cm^{-1}$** | **Calculated Shift from Gas-Phase [a], $cm^{-1}$** |
|---|---|---|---|
| methanol | 1030 | 3250 | 450 |
| ethanol | 1050 | 3195 | 485 |
| 2-methyl-1-propanol | 1006, 1048 | 3200 | 470 |
| 3-methyl-1-butanol | 1010, 1060 | 3191 | 469 |
| acetaldehyde | None | - | - |
| butanal | None | - | - |
| acetone | None | - | - |
| propane | None | - | - |
| *cis*-2-butene | None | - | - |
| acetylene | None | - | - |
| toluene | None | - | - [b] |
| 2-methyl-1-propanol, acetaldehyde, acetone and toluene | 1006, 1048 | 3200 | |

[a,] The gas-phase O-H stretch features for methanol, ethanol, 2-methyl-1-propanol, and 3-methyl-1-butanol are centered at 3700 $cm^{-1}$ [46], 3680 $cm^{-1}$, 3670 $cm^{-1}$, 3660 $cm^{-1}$, respectively [44].

[b,] The IR spectrum of the gas-phase VOC mixture is not available for comparison.

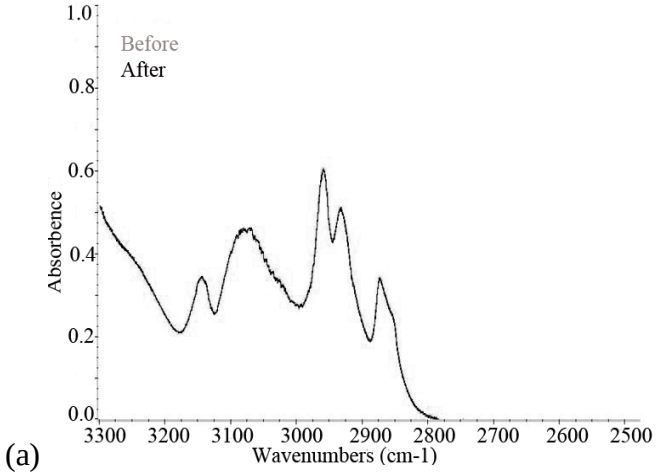


(a)

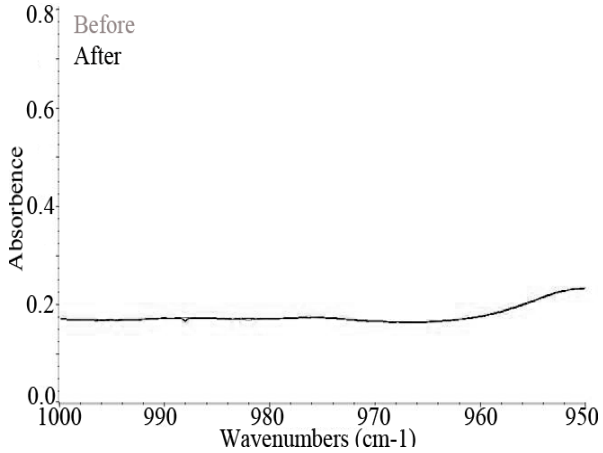


(b)

Figure 3.8. ATR-FTIR spectra of $C_4$mimCl prior to and subsequent to gas-phase toluene exposure in wavenumber regions of (a) 2500 $cm^{-1}$ to 3300 $cm^{-1}$; (b) 950 $cm^{-1}$ to 1000 $cm^{-1}$ where gas-phase toluene features would normally be detected upon absorption in the infrared. Note that there are no differences in the spectra (the lines overlap each other). No other features were detected in the entire IR region analyzed.

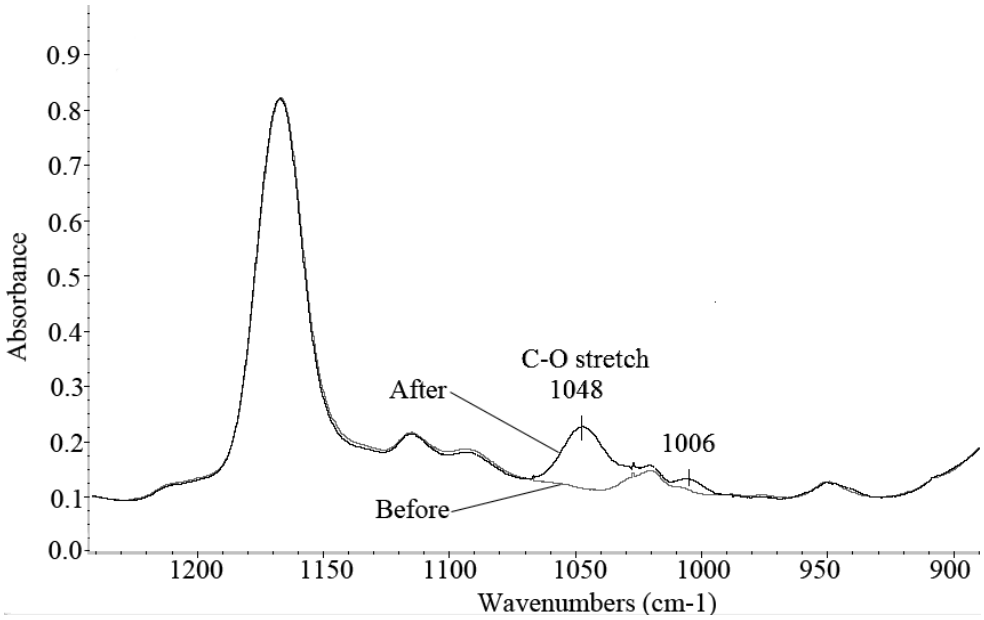


Figure 3.9. ATR-FTIR spectra of $C_4$mimCl prior and subsequent to exposure to a gas mixture containing 2-methyl-1-propanol, acetaldehyde, acetone and toluene. The new features are characteristic of only the 2-methyl-1-propanol. No other new features from other VOCs were detected.

### 3.4 Conclusion

Computational chemistry was used as a tool to investigate the interactions between the ionic liquid, $C_4$mimCl, and a variety of VOCs, including alcohols, aldehydes, a ketone, alkanes, alkenes, an alkyne and an aromatic hydrocarbon. The computational results suggest that $C_4$mimCl is more likely to interact with alcohols as compared to other classes of VOCs. This information is useful in helping to provide a preliminarily screening of selective materials for the eventual development of highly selective sensors for alcohols.

The interactions of methanol and different kinds of ionic liquids were also studied. Methanol is more likely to interact with $C_4$mimCl as compared to $C_4$mimBr and $C_4$mim$BF_4$.

(A)

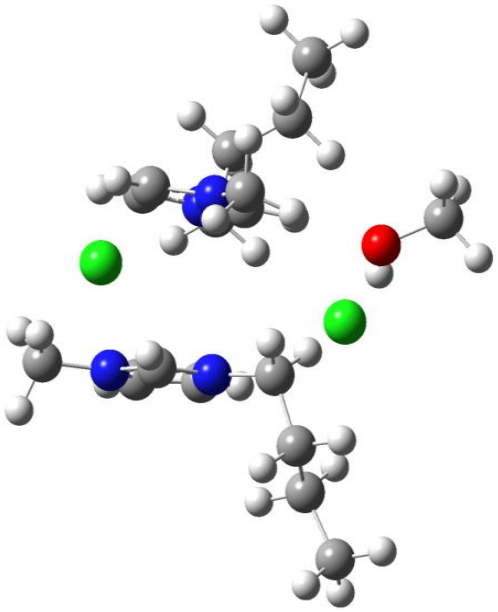

(B)

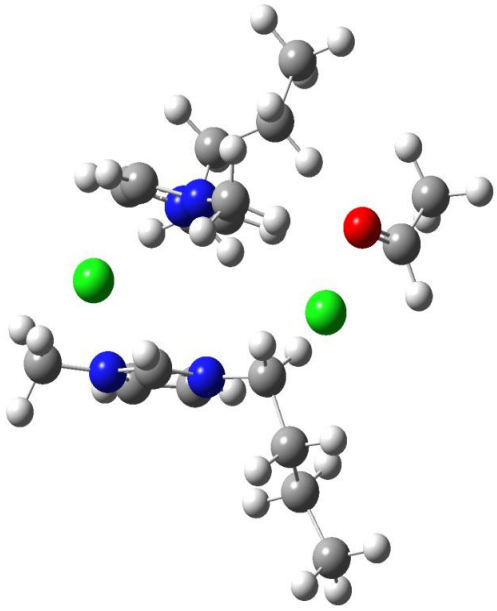

Figure 3.10. Stacked two $C_4$mimCl model with (A) Methanol and (B) Acetaldehyde.

Experiments were also performed to provide further support for the preliminary screening accomplished with the aid of the computational tools.

Infrared spectral changes were observed when $C_4$mimCl was exposed to alcohols, either individually or in a complicated mixture. New peaks were formed in the spectra after exposure of the ionic liquid to the alcohols, and the features are characteristic of the gas-phase alcohol tested. The experimental results illustrate that there are interactions between $C_4$mimCl and alcohols. No new peaks were detected in the IR spectra after exposure of the $C_4$mimCl to aldehydes, a ketone, an alkane, an alkene, an alkyne or an aromatic hydrocarbon. Therefore, in the IR region, $C_4$mimCl is able to selectively respond to alcohols.

The experimental data that were obtained support the results of the computational work. Although the aldehydes/ketones may have been expected to also interact strongly with the ionic liquid because of the large negative thermochemical data obtained using the single ionic liquid model, this was not evident in the experiments conducted. This information suggests that although a single ionic liquid modeling system is a reasonable model for predicting relative trends (and useful as an initial screening tool), the inclusion of a second ionic liquid molecule improves the predictions made and is therefore better. Further inclusion of thermal corrections to the entropy and enthalpy to obtain the variations in the free energies are needed to obtain good predictions. The experimental and computational data obtained in this work indicate that $C_4$mimCl may be an ideal substrate for the development of selective gas-phase alcohol sensors, especially given the relatively low concentrations of alcohols that sensors may be employed to detect.

# CHAPTER 4

# KINETIC CONSTANTS FOR THE INTERACTIONS OF 2-METHYL-1-PROPANOL, 3-METHYL-1-BUTANOL, AND ACETIC ACID VAPORS WITH $C_4$mimCl IONIC LIQUID SURFACES

## 4.1 Introduction

Organic acids, formic and acetic acid in particular, are important ubiquitous constituents of the global troposphere. They are also common constituents of global precipitation[312]. Formic and acetic acids contribute between 16% and 35% of the free acidity in North American precipitation and between 25% and 98% of the free acidity of precipitation in remote areas[313]. There are various sources of gas-phase organic acid, including direct anthropogenic emissions, such as motor exhaust and engine oil[314]. Biogenic emissions are also one of the major sources of organic acid[315]. The diurnal measurement of gas-phase organic acids in the canopy in central Amazonia suggest that acetic acid may be emitted directly by vegetation[316]. In addition, secondary sources like in situ production from precursors in the troposphere have also been suggested as a major source of acids in the atmosphere[313, 317]. Various mechanisms have been proposed as important sources of tropospheric formic and acetic acids. Photochemical decomposition of natural hydrocarbons, isoprene in particular, may be an important source of formic acid[317]. Oxidation of gas-phase formaldehyde by gas-phase $HO_2$ is another possible source of formic acid[321].

Sensors have been widely used in many aspects of environmental monitoring[275, 276], as well as in industry[318], medical monitoring[278] and traffic[319].

One potential application of a sensor is in the detection of gas-phase compounds that are generated from mold, i.e. mold volatile organic compounds, or MVOCs. The metabolites of fungi detected in households and in work places are considered to be potential health hazards[146, 147, 156]. Gas-phase alcohols, including 2-methyl-1-propanol and 3-methyl-1-butanol, were found to be representative volatile organic compounds (VOCs) that were generated by molds [143, 157, 320]. Organic acids, such as acetic acid, were also found in the emissions of molds in buildings[146, 320]. Therefore, the simultaneous detection of organic acids and alcohols may be an effective indicator of mold formation.

In the previous work[265], the interaction of ionic liquids and several classes of VOCs were investigated through closely coupled computational chemistry and experimental techniques. The FTIR results showed that the ionic liquid, $C_4$mimCl was selective towards alcohols in a mixture of different types of VOCs that included alcohols, aldehydes, ketones, alkanes, alkenes, alkynes and aromatic compounds [265]. In this work, we extended our investigations to a gas-phase organic acid. Acetic acid is used as an example of an organic acid. The interaction between $C_4$mimCl and acetic acid was studied in this work using both computational tools and laboratory experiments.

The reversibility of a sensor is very important for sensor development. In this work, the reversibility of the interaction between $C_4$mimCl and gas-phase acetic acid was studied experimentally by a series of association and dissociation processes. The association and dissociation rate constants ($k_a$ and $k_d$, respectively,

in Reaction 4.1 and Equation 4.1 through 4.3) of acetic acid and the two alcohols with the ionic liquid thin film of $C_4$mimCl were also determined.

The association and dissociation process between the ionic liquid thin film surface and VOCs can be described mathematically[321-323]. The interaction between VOC and $C_4$mimCl is described by a bimolecular model (Reaction 4.1).

$$A + B \underset{k_d}{\overset{k_a}{\Leftrightarrow}} C \qquad \text{(Reaction 4.1)}$$

where A is the VOC, B is $C_4$mimCl and C is the VOC-$C_4$mimCl complex that is formed upon interaction of the reactants. The parameters $k_a$ and $k_d$ are, respectively, the association and dissociation rate constants. Using Reaction 4.1, the overall mass balance may be represented according to Equation 4.1:

$$\frac{\partial C}{\partial t} = k_a[A][B] - k_d[C] \qquad \text{(Equation 4.1)}$$

where, [A]= the concentration of the VOC

[B]= the concentration of $C_4$mimCl

[C]= the concentration of the VOC-$C_4$mimCl complex

t= time

Assuming that the initial concentration of A, i.e. $[A_0]$, is much greater than the concentration of the complex that is formed (i.e. [C]), when steady state is achieved (i.e. $\frac{\partial C}{\partial t} \to 0$), the concentration of the VOC-$C_4$mimCl complex can be represented according to Equation 4.2, where $[C_{max}]$ is the maximum concentration of theVOC-$C_4$mimCl complex.

$$[C] = [C_{\max}](1 - e^{-(k_a[A_0] + k_d)t}) \qquad \text{(Equation 4.2)}$$

Equation 4.2 describes the association process for the VOC and $C_4$mimCl interaction. The dissociation process is described in Equation 4.3.

$$[C] = [C_{\max}] \times e^{-k_d t} \qquad \text{(Equation 4.3)}$$

**4.2 Computational Details**

Initially the interaction between $C_4$mimCl and acetic acid was investigated using the Gaussian 03 package [324]. First, the geometries of the ionic liquid and acetic acid were individually optimized using a Hartree-Fock method and a 6-31 G (d) basis set. Subsequently, the geometry of the $C_4$mimCl – acetic acid pair was optimized using the same computational method. Additional calculations were then performed to determine the thermodynamic parameters.

**4.3 Experimental Details**

The interaction between $C_4$mimCl and acetic acid was also investigated through experiments. A cylindrical chamber of 2 Liters in volume was used as the exposure chamber. A zinc selenide crystal trough with a thin film of the $C_4$mimCl (~50 μm thickness) was placed in the exposure chamber and exposed to a flow of acetic acid gas originating from a Teflon bag. The thin film surface before and after exposure to the gas was analyzed using Fourier-transform infrared spectroscopy (Thermo Nicolet FTIR 6700) with attenuated total reflectance (ATR). A Teflon cap was placed on the trough to minimize the loss of the sample when transferring the trough with the ionic liquid between the exposure chamber and the FTIR.

The association and dissociation rate constants for $C_4$mimCl with acetic acid, 2-methyl-1-propanol and 3-methyl-1-butanol were determined using a custom designed cylindrical chamber of 0.2 Liters in volume as the exposure chamber. The chamber was seated on the ATR attachment of the FTIR so that an *in-situ* experiment was possible. An o-ring was used to connect the chamber with the ATR-attachment to make sure that the chamber was airtight. A zinc selenide crystal trough with a thin film of $C_4$mimCl was placed in the exposure chamber and exposed to a flow of either each VOC or zero air originating from a Teflon bag. A pump was attached to the outlet of the chamber and was used to pull the gas from the Teflon bag through the chamber and to the exhaust. A mass flow controller (Omega Engineering, Inc., Stamford, CT) was used to control the flow rate of the gas. A valve was used to switch between the flow of VOC and zero air. When the VOC was introduced into the chamber, the association process between $C_4$mimCl and the VOC started. When the flow was switched to zero air, the dissociation process was initiated. The association and dissociation processes were repeated at least 3 times for each bag of VOC.

A known amount of each VOC compound was prepared in an 80 L Teflon bag through the vaporization of the pure component liquid compound. Microliter quantities of the liquid compound were injected using a syringe (Hamilton Company, Reno, NV) into a small vaporization chamber containing a stream of purified air that was generated using a zero air generator (Perma Pure LLC., Toms River, NJ). The flow rate of zero air through the vaporization chamber and into the bag was controlled by a mass flow controller that was placed upstream of the

vaporization chamber. For the association and dissociation rate constant experiments, the concentrations of acetic acid used were 300, 500 and 800 $ppm_v$. The concentrations of 2-methyl-1-propanol were 500, 600 and 700 $ppm_v$. The concentrations of 3- methyl-1-butanol were 500, 600 and 700 $ppm_v$. Relatively high concentrations of VOCs were chosen for the association and dissociation rate constant determination experiment to ensure that the VOC molecules were in excess as compared to the $C_4$mimCl. The excess VOCs thus allowed the rate constants to be determined by the ability of the gas to interact with the $C_4$mimCl surface, as opposed to being limited by the availability of the gas molecules.

The ionic liquid used in the experiments was $C_4$mimCl (Sigma Aldrich, ≥ 99.0%, dry) and was used in a thin film configuration. To generate the thin film, a solution of the ionic liquid was made by dissolving 0.01 g of $C_4$mimCl dry powder in chloroform. The solution was placed onto a zinc selenide crystal trough, and the chloroform was subsequently evaporated. The thickness of the $C_4$mimCl film is about 50 nm.

All compounds were purchased from Sigma-Aldrich with the following stated purities: 2-methyl-1-propanol (99.5%), 3-methyl-1-butnaol (≥ 99%), acetic acid (≥ 99.7%), chloroform (≥ 99%) and $C_4$mimCl (≥ 99.0%).

Both the interactions between $C_4$mimCl and acetic acid and the association and dissociation experiment for $C_4$mimCl and the three VOCs were investigated using ATR-FTIR. For the interaction experiment between $C_4$mimCl and acetic acid, the ionic liquid thin film was analyzed before and after exposure to the VOC using ATR-FTIR employing a mercury cadmium telluride (MCT) detector and

OMNIC® software set to collect 16 scans at 0.5 $cm^{-1}$ resolution. For the association and dissociation experiments, the data were collected using 4 scans at 0.5 $cm^{-1}$ resolution. The change in the number of scans was undertaken because the association and dissociation between $C_4$mimCl and the VOCs investigated in this work are relatively fast. Thus, faster data collection was needed. All of the association and dissociation rate constant data were collected at room temperature. The absolute peak height was used as absorbance in IR spectra. The association and dissociation rate constants were determined using Scrubber 2[325], a program which is designed to rapidly format association and dissociation data for analyses.

Several background experiments were performed prior to the actual association/dissociation studies. Background experiments were carried out to determine whether air had any influence on the system by exposing the ionic liquid to a flow of zero air without the VOC. Background experiments were also carried out to determine whether the VOC was lost to the surface of the trough. This was performed by placing the trough without $C_4$mimCl in the chamber and flowing the VOC into the chamber and analyzing the trough's surface by FTIR before and after exposure to the VOCs.

**4.4 Results and Discussion**

The optimized geometries of $C_4$mimCl and acetic acid are presented in Figure 4.1. The computational study of the interaction between $C_4$mimCl and acetic acid resulted in an enthalpy of -19.7 kcal/mol and Gibbs energy of -9.0 kcal/mol. The negative enthalpy and Gibbs energy indicate that $C_4$mimCl is likely

to interact with acetic acid. In addition, the interaction length, which is defined in this work as the shortest distance between an atom of the $C_4$mimCl and an atom of the target VOC, indicates that the possible interaction positions between $C_4$mimCl and acetic acid are the hydrogen from the –OH group of the acetic acid with Cl from the $C_4$mimCl, and oxygen from the –OH group of acetic acid with hydrogen from the $C_4$mimCl. The possible interaction positions are presented in Figure 4.1. The dashed lines indicate the possible interaction between those atoms.

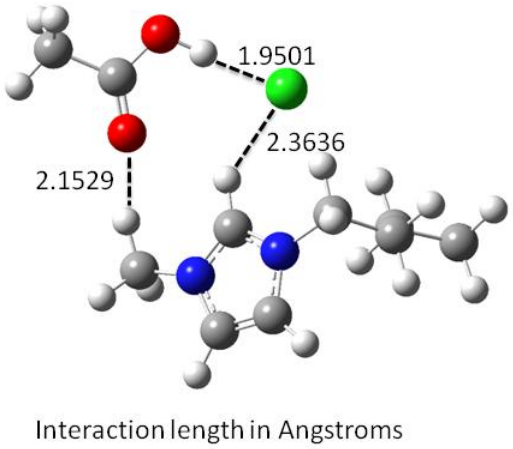


Figure 4.1. Optimized structure of $C_4$mimCl and acetic acid. The dashed lines indicate the possible interaction positions between the two molecules.

The background experimental results showed that neither zero air nor the trough had any measurable influence on the acetic acid levels. The IR spectra of the $C_4$mimCl thin film before and after exposure to the gas-phase acetic acid were obtained by ATR-FTIR. The IR spectrum of the $C_4$mimCl thin film before and

after exposure to the acetic acid is presented in Figure 4.2. Before interaction with acetic acid, $C_4$mimCl itself has IR features at 1300, 1337, 1382 and 1429 $cm^{-1}$. The peak at 1300 $cm^{-1}$ may be assigned to $–CH_2$-halogen (Cl) interaction from the $C_4$mimCl, while the peaks at 1337, 1382 and 1429 $cm^{-1}$ may be assigned to $–CH_3$ from the $C_4$mimCl[326]. The IR spectrum after exposure to acetic acid was compared to the IR spectrum of gas-phase acetic acid from the NIST Webbook[326], and contained similar features. The peak at 1720 $cm^{-1}$ is from the C=O stretch of acetic acid, while the peaks at 1233 $cm^{-1}$ is from the OC-OH stretch of the acetic acid. The increase of peaks at 1337, 1382 and 1429 $cm^{-1}$ is from the $–CH_3$ group from the acetic acid. Therefore, the experimental results confirmed the computational results that strongly suggest that acetic acid interacts with $C_4$mimCl.

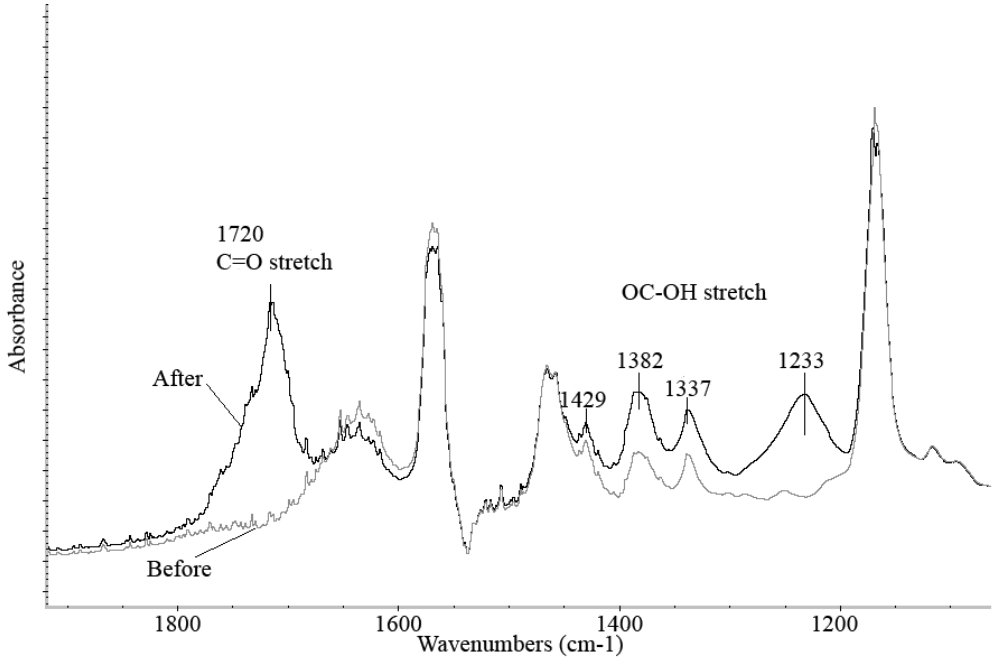


Figure 4.2. The IR spectrum for the interaction between $C_4$mimCl and acetic acid.

A frequency shift is observed in the IR spectrum. The IR spectrum of gas-phase acetic acid from the NIST Webbook has a peak at 3550 $cm^{-1}$ which corresponds to the COO-H stretch. A peak at 2550 $cm^{-1}$ is observed in our IR spectrum, and likely corresponds to the COO-H stretch. Therefore, there is a shift of 1000 $cm^{-1}$ from the gas-phase COO-H stretch. The shift suggests that the interaction between acetic acid and $C_4$mimCl may happen between the O atom from the –OH group of acetic acid and an atom from $C_4$mimCl, or/and between the H atom of the –OH group of the acetic acid and an atom from $C_4$mimCl. In addition, the corresponding COO-H stretch of acetic acid in the liquid-phase is centered at about 3000 $cm^{-1}$[1326]. Thus, the condensed acetic acid has a shift of about 550 $cm^{-1}$ from gas-phase acetic acid. Therefore, the shift of the interaction of acetic acid with the ionic liquid is 450 $cm^{-1}$ larger, suggesting that stronger H bonding occurs in the presence of ionic liquid.

Figures 4.3, 4.4 and 4.5 represent the results of the association and dissociation of the VOCs onto the ionic liquid thin film as an example. The results for only one concentration of the VOCs are presented here as examples.

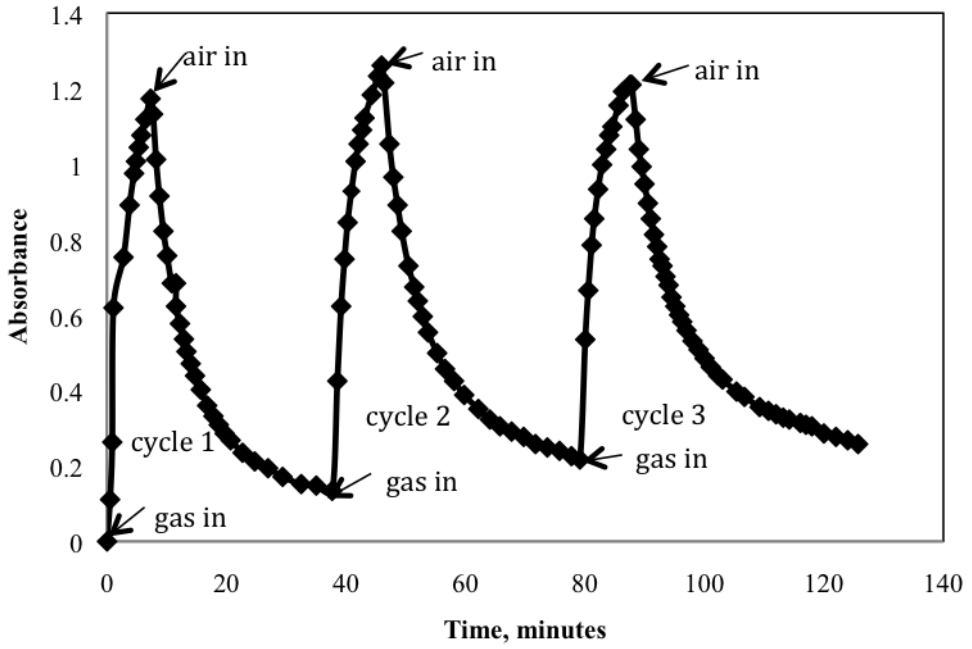


Figure 4.3. The association and dissociation of 800 $ppm_v$ acetic acid and $C_4$mimCl.

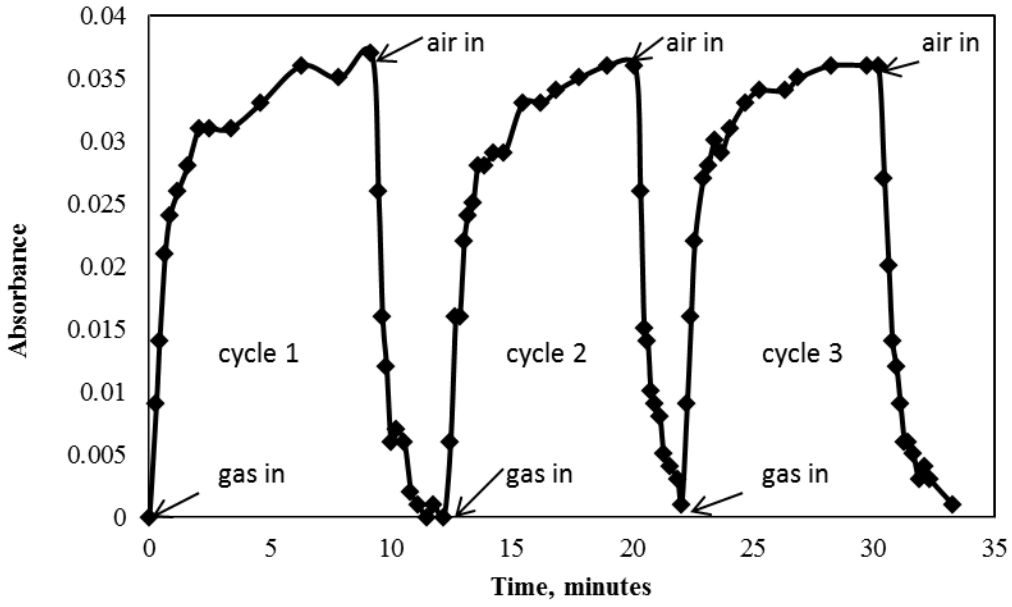


Figure 4.4. The association and dissociation of 700 $ppm_v$ 2-methyl-1-propanol and $C_4$mimCl.

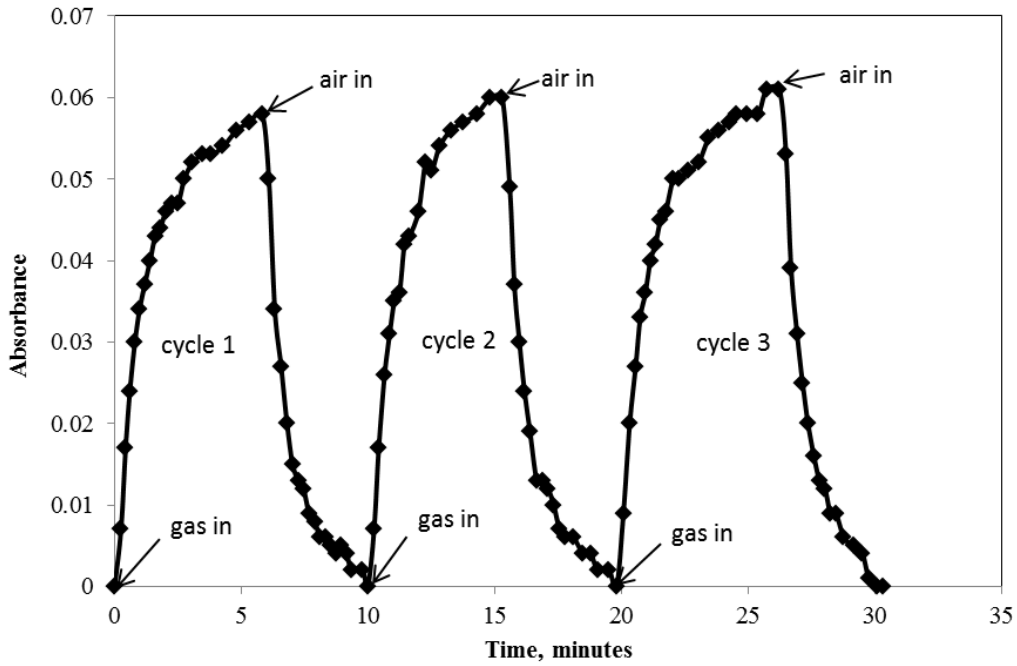


Figure 4.5. The association and dissociation of 600 $ppm_v$ 3-methyl-1-butanol and $C_4$mimCl.

Figures 4.3-4.5 demonstrate that after one cycle of association and dissociation of acetic acid, 2-methyl-1-propanol or 3-methyl-1-butanol from the $C_4$mimCl thin film surface, the response in absorbance is able to achieve the same level if the gases are re-introduced to the chamber. Note that the dissociations of acetic acid in 3 cycles were not completed (Figure 4.3). The last point in each dissociation cycle does not reduce to zero (the baseline) because the interaction between $C_4$mimCl and acetic acid is relatively strong. Thus, the dissociation between these two compounds requires a much longer time. The results of several cycles of association and dissociation illustrate that the absorbance of these VOCs to the $C_4$mimCl surface is repeatable over several cycles. This is exceptionally important if $C_4$mimCl is used as a sensor material. The repeatability of the

interaction between the material and the target compounds are significant for sensor development. Therefore, the results show that a $C_4$mimCl thin film is a good candidate material for detecting gas-phase acetic acid and two alcohols in terms of repeatability. In addition, combined with our previous work, $C_4$mimCl selectively interacts with alcohols and acetic acid from a series of classes of VOCs in the IR region. Therefore, $C_4$mimCl is also a good candidate sensor material in terms of selectivity.

The association and dissociation rate constants for $C_4$mimCl with three VOCs were determined using the software Scrubber 2. A simulation of the experimental data for each concentration of each compound was performed. Figure 4.6 presents the simulation results for one cycle of one concentration of acetic acid as the example. The association and dissociation rate constants for each cycle of the interaction between $C_4$mimCl and each concentration of VOC were calculated. The rate constants obtained for different cycles are similar. This similarity demonstrates that at least at the beginning of 3 or 5 cycles, $C_4$mimCl has the ability to interact with or dissociate each VOC at the same rate. In addition, since the VOCs are in excess in the interactions, the association and dissociation rates only depend on the absorptive ability of $C_4$mimCl with each VOC. Therefore, average values are calculated for different concentrations of VOC and different cycles of VOC-$C_4$mimCl interaction. These average values are reported as the association and dissociation rate constants in Table 4.1. The equilibrium constant, $K_D$, which is $k_d/k_a$, was also calculated for each $C_4$mimCl-

VOC interaction, and is presented in Table 4.1. The errors in the data of Table 4.1 represent $\pm 1\sigma$.

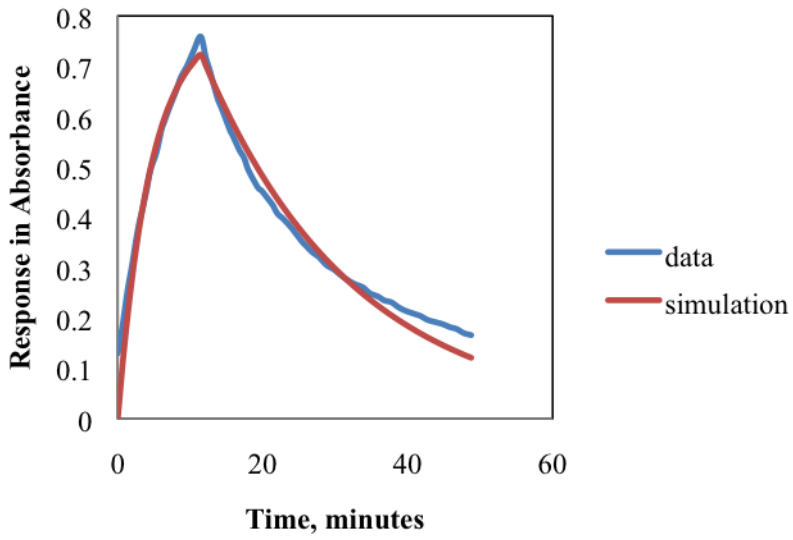


Figure 4.6. Simulation results for the interaction between $C_4$mimCl and VOCs. The third cycle of interaction between 300 $ppm_v$ acetic acid and $C_4$mimCl is used as an example.

Table 4.1. Association and Dissociation Rate Constants and ΔG of $C_4$mimCl-VOCs Interactions

| **Compounds** | **$C_4$mimCl+ Acetic Acid** | **$C_4$mimCl + 2-methyl-1-propanol** | **$C_4$mimCl + 3-methyl-1-butanol** |
|---|---|---|---|
| $k_a$, L/(mol ×min) | $(1.23 \pm 0.44) \times 10^4$ | $(6.73 \pm 2.13) \times 10^3$ | $(7.37 \pm 0.36) \times 10^3$ |
| $k_d$, 1/min | $0.06 \pm 0.02$ | $1.07 \pm 0.25$ | $1.11 \pm 0.30$ |
| $K_D$, μM | $6.26 \pm 3.02$ | $(1.64 \pm 0.24) \times 10^2$ | $(1.51 \pm 0.42) \times 10^2$ |
| ΔG, Kcal/mol | $-(7.2 \pm 0.3)$ | $-(5.2 \pm 0.1)$ | $-(5.2 \pm 0.2)$ |

$k_a$: Association rate constant
$k_d$: Dissociation rate constant
$K_D$: Dissociation equilibrium constant
ΔG: Calculated Gibbs energy at room temperature, 298K.

As compared to the two alcohols, acetic acid has a smaller dissociation rate constant ($k_d$) and a larger association rate constant ($k_a$). This demonstrates that acetic acid has a stronger interaction with $C_4$mimCl as compared to the two alcohols. The experimentally determined results are consistent with the current and previous[265] computational study that yielded the thermochemical data associated with the interactions between $C_4$mimCl and the VOCs. The enthalpy and Gibbs energy for the interaction between $C_4$mimCl and 2-methyl-1-propanol are -14.5 and -7.0 Kcal/mol, respectively[265]. The enthalpy and Gibbs energy for the interaction between $C_4$mimCl and 3-methyl-1-butanol are -14.8 and -7.4 Kcal/mol, respectively[265]. According to the computational study, the energies corresponding to the interaction between $C_4$mimCl and two alcohols are similar. The values of the association and dissociation rate constants from the experiments for these two alcohols are also similar. The enthalpy and Gibbs energy for the interaction between $C_4$mimCl and acetic acid are -19.7 and -9.0 Kcal/mol, respectively. These energies are more negative than the energies for the two alcohols, which indicates that the interaction between acetic acid is more energetically favorable. The association and dissociation rate constants obtained from the experiments are consistent with the computational results.

The dissociation equilibrium constant, $K_D$, can be related to the Gibbs energy $\Delta G$ by the relation $\Delta G = RT \times \ln(K_D)$. Therefore, the Gibbs energies can also be obtained experimentally and are presented in Table 4.1. The error represents $\pm 1\sigma$. Comparing the $\Delta G$ values of three different VOC-$C_4$mimCl interactions that were calculated using the experiments to the $\Delta G$ values obtained

from the computational study, it is clear that the ΔG values calculated from the experimental data have the same trend. Moreover, the absolute differences between the computational and experimentally derived Gibbs energies are within 2 kcal/mol, a value that is within the computational and experimental errors[265]. The interactions of 2-methyl-1-propanol-$C_4$mimCl and 2-methyl-1-butanol-$C_4$mimCl have similar ΔG values while the interaction between acetic acid and $C_4$mimCl has a more negative ΔG.

The dissociation equilibrium constant $K_D$, which is $k_d/k_a$, is characteristic of the interaction strength of the two compounds. The smaller the $K_D$ value is, the stronger the interaction is. The $K_D$ value for acetic acid and $C_4$mimCl is around 1/20 of those for $C_4$mimCl and the two alcohols. Therefore, the interaction between $C_4$mimCl and acetic acid is stronger than that between $C_4$mimCl and the two alcohols.

**4.5 Conclusion**

The ionic liquid thin film of $C_4$mimCl was found to be able to selectively detect gas-phase alcohols from a series of different VOCs, including alcohols, aldehydes, ketones, alkanes, alkenes, alkynes and aromatic compounds, in the IR region in our previous work[265]. In this work, the investigation of the interaction between $C_4$mimCl thin films and VOCs was extended to another class of VOCs, the organic acid. The computational studies suggest that acetic acid is likely to interact with $C_4$mimCl. The interaction length and the shift in the IR spectral frequencies in the computational study suggest that the possible interaction

positions between acetic acid and $C_4$mimCl are the O atom of –OH group or/and the H atom of the –OH group of acetic acid with atoms of $C_4$mimCl.

A laboratory study of the interaction between $C_4$mimCl and acetic acid confirmed the computational study. Multiple new peaks were identified in the IR spectrum of $C_4$mimCl after exposure to the gas-phase acetic acid. The new peaks are characteristic of acetic acid. In addition, a shift was also identified in the IR spectra that corresponded to a change in the COO-H stretch of acetic acid. Therefore, the interaction between acetic acid and $C_4$mimCl may occur between the O atom from the –OH group of acetic acid and an atom from $C_4$mimCl, or/and between the H atom of the –OH group of the acetic acid and an atom from $C_4$mimCl. This confirmed the prediction made in the computational study.

The association and dissociation reactions of $C_4$mimCl with acetic acid and the two alcohols were also studied experimentally. Gas-phase acetic acid, 2-methyl-1-propanol and 3-methyl-1-butanol are able to dissociate from the $C_4$mimCl surface if they are not present in the gas-phase above the surface of $C_4$mimCl. In addition, $C_4$mimCl thin film is able to interact with acetic acid, 2-methyl-1-proponal and 3-methyl-1-butanol and gives a response in absorbance without the loss of signal after several association and dissociation cycles if the gas-phase organic acid or alcohols are re-re-introduced above the $C_4$mimCl thin film surface. This characteristic illustrates that a $C_4$mimCl thin film is a very good candidate for a repeatable, non-destructive sensor material.

The association and dissociation rate constants of gas-phase acetic acid, 2-methyl-1-propanol and 3-methyl-1-butanol from the $C_4$mimCl surface were

calculated. The dissociation equilibrium rate and ΔG were also calculated for the three interactions. A smaller dissociation equilibrium constant and more negative ΔG for the $C_4$mimCl-acetic acid pair demonstrate that acetic acid has stronger interaction with $C_4$mimCl as compared to 2-methyl-1-propanol and 3-methyl-1-butanol.

### 4.6 Considerations for the Design of a Mold Sensor

The ionic liquid of $C_4$mimCl has demonstrated its selectivity towards alcohols and organic acid. As illustrated in Chapter 1, 3-methyl-1-butanol, 1-pentanol, 1-hexanol, and 1-octen-3-ol were the main VOCs produced by mold that grew on building materials. In addition, the total concentration of all alcohols in the contaminated rooms was 4%-42% higher than the concentration in rooms without mold[153]. Thus, a change in alcohol concentration from the background may provide an opportunity to use alcohols as an indicator of mold growth. Organic acids, such as acetic acid, were also found in the emissions of molds in buildings[146, 320]. Therefore, identifying a series of alcohols combined with organic acid may be an option for the specific detection of mold. In addition, the reversibility of the ionic liquid, $C_4$mimCl, for association and dissociation of alcohols and organic acid demonstrates that $C_4$mimCl is a good candidate sensor material.

Another challenge in using MVOCs as indicators of mold is the emission rate of MVOCs. The concentration of MVOCs at the initial mold growing stage is at ppb level. The method using $C_4$mimCl combined with the infrared technique in this work is able to selectively detect ppm level alcohols and organic acid. In

order to more sensitively detect MVOCs, increasing the IR beam path length may be an option to detect compounds in lower concentration. Alternatively, more sensitive techniques, such as a tuning fork[327], can be used in combination with a $C_4$mimCl film to provide selectivity towards gaseous mold indicators (alcohols and organic acid).

The challenge in using the ionic liquid, $C_4$mimCl, directly as a sensing material is the dewetting of the ionic liquid[298]. Therefore, finding a material to support the ionic liquid in a sensing platform is important, since the use of a trapped ionic liquid avoids the problem of dewetting. Alumina nanopores have been employed as an ionic liquid supporting material and the problem related to dewetting has been overcome by using the pores as a rigid matrix[328]. In addition, there are also studies using silica as the ionic liquid supporting matrix[329, 330]. Carbon nanotubes have been used as a potential support for ionic liquid because of their inherent advantageous properties such as mechanical strength, high chemical stability, and a large surface area-to-volume ratio[331]. Here, a graphene-based material for support of the $C_4$mimCl is proposed.

Graphene is a promising carbon material that has attracted considerable attention from the scientific communities in recent years[332]. Graphene is a monolayer of $sp^2$ hybridized carbon atoms packed into a dense honeycomb crystal structure[332]. Graphene has high chemical resistivity against most media[242]. In addition, graphene has high surface area[243, 333]. The high surface area may enhance the sensitivity of the graphene-ionic liquid composite towards targeted VOCs. Therefore, the preparation and application of a supported ionic liquid is of

great interest due to the combined advantages of selectivity and sensitivity that may be afforded by the ionic liquid and graphene- based support material.

The oxidized phase of graphene, which is graphite oxide (GO), contains many reactive epoxy groups[334, 335]. The nucleophilic ring-opening reaction between the epoxy groups of GO and the amine groups of an amine-terminated $C_4$mimCl should easily happen when KOH is used to catalyze the reaction[336]. During the reaction, GO is reduced to reduced graphite oxide (RGO). The sample was subsequently dried at room temperature. The synthesis of an ionic liquid-RGO (IL-RGO) composite is illustrated in Figure 4.7.

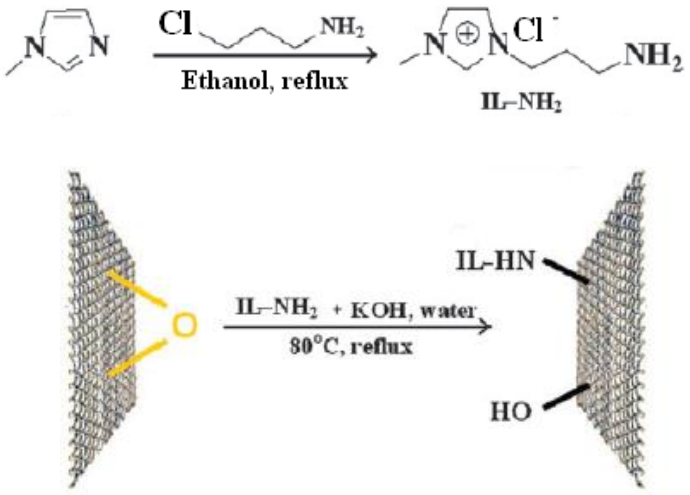


Figure 4.7. Synthesis of amine-terminated ionic liquid of $C_4$mimCl and synthesis of IL-RGO composite.

The synthesized IL-RGO was tested to determine whether it was able to interact with the alcohols or organic acid. Figure 4.8 shows the IR spectra of IL-RGO before and after exposure to gas-phase 2-methyl-1-propanol. The adsorbed

gas-phase 2-methyl-1-propanol is expected to show a new feature at 1000 to 1100 $cm^{-1}$. However, there is no new peak formed at this range in the IR spectrum of IL-RGO after exposure to the gas. In addition, there is no new feature in the IR spectrum after exposure to gas-phase 2-methyl-1-propanol in the entire IR range of 700 to 4000 $cm^{-1}$. The interaction between IL-RGO and gas-phase acetic acid was also investigated. However, no new peak in the IR spectrum was observed after exposure of IL-RGO to the gas-phase acetic acid.

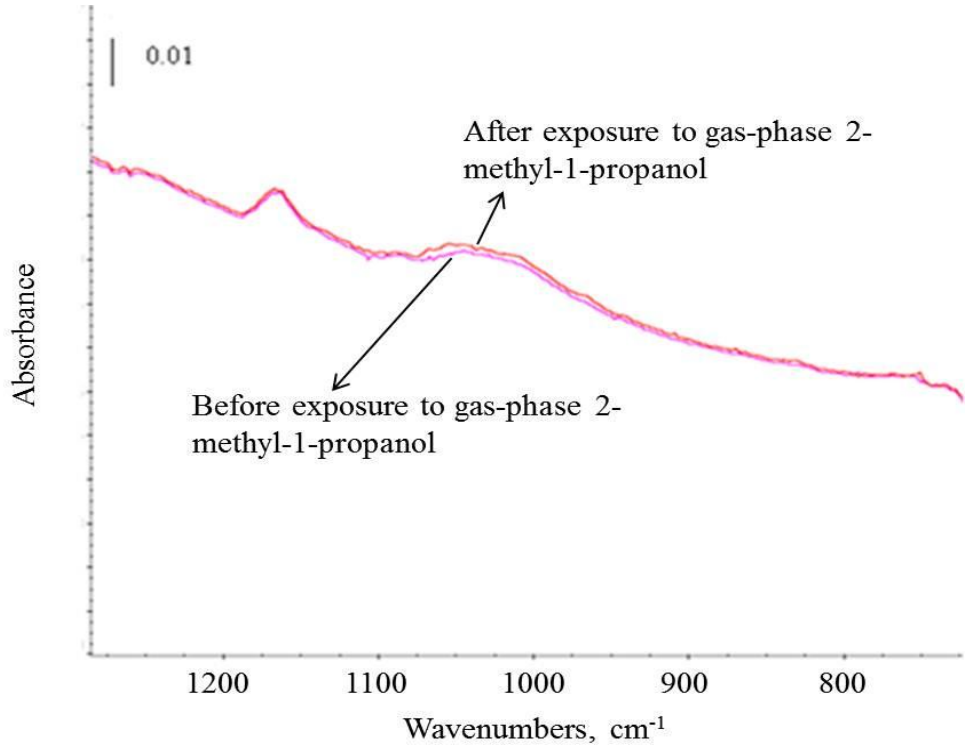


Figure 4.8. The IR spectra of IL-RGO before and after exposure to gas-phase 2-methyl-1-propanol.

As reported previously, the ionic liquid of $C_4$mimCl is able to selectively interact with gas-phase 2-methyl-1-propanol, 3-methyl-1-butanol and acetic acid

and form new peaks in the IR spectra. However, the ionic liquid of $C_4$mimCl functionalized on the RGO surface does not result in any new infrared spectral features after the alcohol or acetic acid is exposed to the surface. Therefore, the question was raised of whether the functionalization of the ionic liquid changes the properties of the ionic liquid that are needed to attract the gas-phase alcohols or organic acids. As a comparison, the interaction between reduced graphite oxide (RGO) - $C_4$mimCl paste and gas-phase alcohols was investigated. RGO was prepared using the same reaction for IL-RGO but without adding the ionic liquid. The RGO-$C_4$mimCl paste was prepared by a simple mixing of RGO and the ionic liquid of $C_4$mimCl.

The interaction of RGO-$C_4$mimCl paste with 2-methyl-1-proponal was also investigated. Figure 4.9 shows the IR spectra of the RGO-$C_4$mimCl paste before and after exposure to the gas-phase 2-methyl-1-propanol. A new peak at 1050 $cm^{-1}$ was formed after exposure of the material to the gas. The new peak is characteristic of gas-phase 2-methyl-1-propanol. Figure 4.10 shows the IR spectra of the RGO-$C_4$mimCl paste before and after exposure to a VOC mixture containing an alcohol, an aldehyde, a ketone, and an aromatic compound. A new peak at 1050 $cm^{-1}$ was formed in the IR spectrum after exposure to the VOC mixture. The new peak is only characteristic of the alcohol in the VOC mixture, which is 2-methyl-1-propanol.

In Chapter 3, the computational study suggested that ionic liquid molecules are more likely to stay in the stacked structure where a cavity is

formed. Previously published work has suggested that ionic liquids form cavities that are of a sufficient size to accommodate the interacting analyte[309].

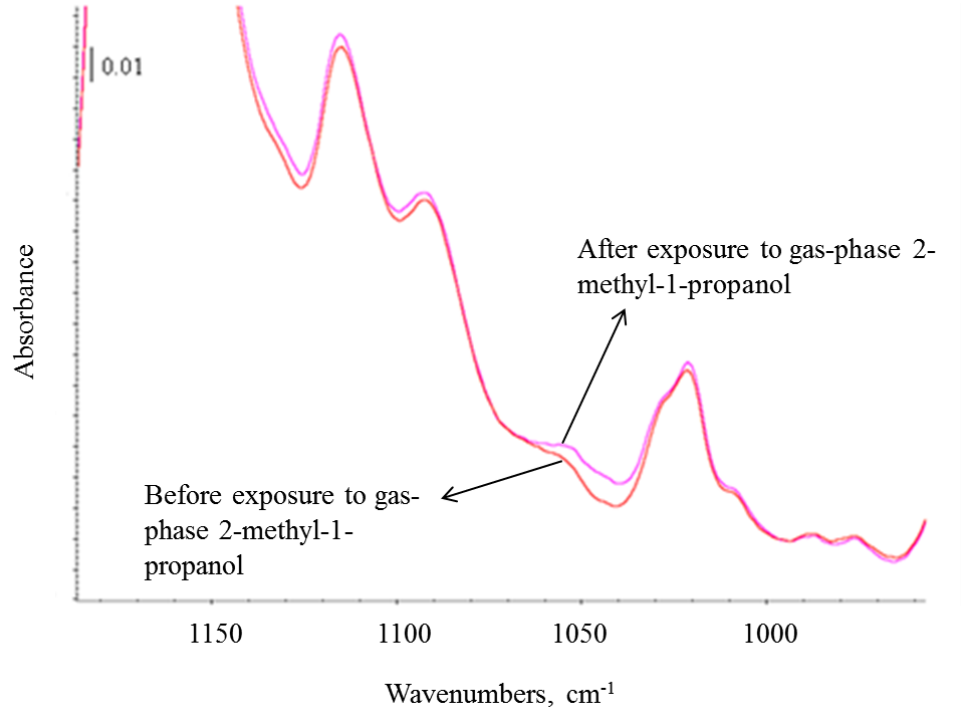


Figure 4.9. The IR spectra of RGO-$C_4$mimCl paste before and after exposure to gas-phase 2-methyl-1-propanol.

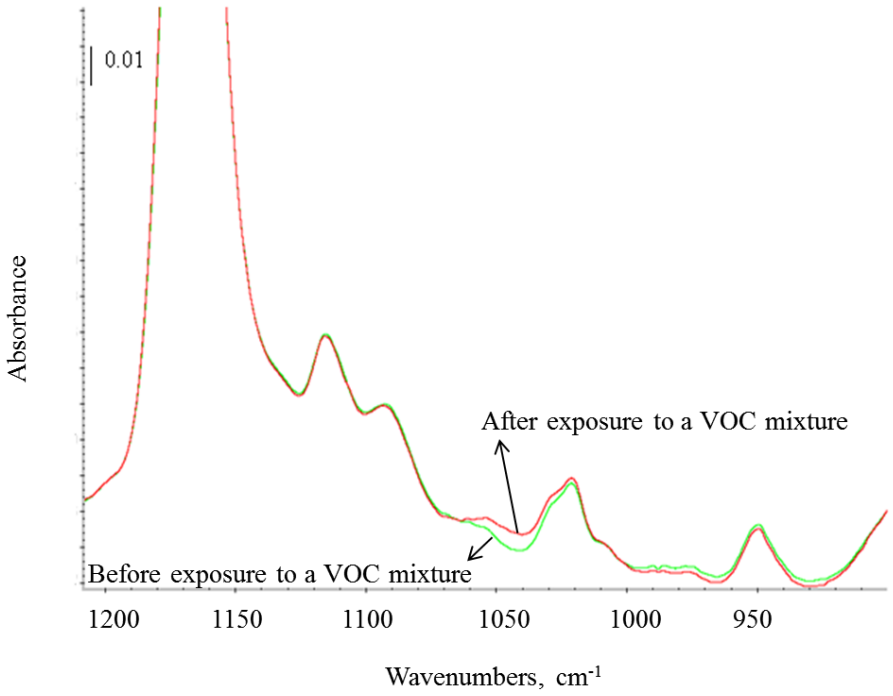


Figure 4.10. The IR spectra of RGO-$C_4$mimCl paste before and after exposure to a VOC mixture containing gas-phase 2-methyl-1-propanol, butanal, acetone, and toluene.

The computational study of the interactions of methanol with the stacked two $C_4$mimCl model shows that the hydrogen atom in the –OH group of methanol is much closer to the cavity region of the ionic liquids. Therefore, the computational study suggests that the cavity formation is critical for gas-phase alcohol to interact with ionic liquid. However, when the ionic liquid is functionalized on the surface of RGO, the orientation of the ionic liquid molecules may be changed based on the sites for functionalization on the GO surface, in this case the epoxy groups on the GO surface. The functionalization may minimize the formation of ionic liquid cavity structures, thus inhibiting the interaction of the alcohol with the surface. The lack of cavity structures may explain the absence of new IR features when 2-methyl-1-propanol is exposed to

the IL-RGO. However, the interaction between 2-methyl-1-propanol and RGO-$C_4$mimCl paste is detectable in the IR spectra since the ionic liquid was simply mixed with the RGO. The structure of the ionic liquid was not changed. Therefore, using a carbon material with high surface area and simply coating $C_4$mimCl onto the material surface may be useful for enhancing the sensitivity of $C_4$mimCl for the detection of alcohols or organic acid.

The IL-RGO material has many unique properties that are applicable to other areas of environmental concern. The IL-RGO material was used as part of a composite material and applied to the issue of energy generation through the reduction of $CO_2$ to fuels. The details of synthesizing IL-RGO and an IL-RGO/$TiO_2$ nanocomposite material, as well as application of the composite material for $CO_2$ photoreduction is described in the next chapter.

# CHAPTER 5

# IONIC LIQUID FUNCTIONALIZED REDUCED GRAPHITE OXIDE / $TiO_2$ FOR CONVERSION OF $CO_2$ TO $CH_4$

## 5.1 Introduction

Energy plays a critical role in the quality of life, economic prosperity, and environmental sustainability. Population increases and rapid economic development create the demand for energy that may more than double in the next mid-century[337]. Currently, among the available energy sources, fossil based fuel supply remains dominant[337]. Once combusted, fossil fuels lead to the formation of carbon dioxide ($CO_2$), which is one of the major contributors to global climate change. Both the limited supply of fossil based fuel and the presence of excess amounts of ambient $CO_2$ urge the development of more sustainable energy resources. The recycling of carbon dioxide to fuels over photocatalytic materials provides a potential solution.

Photocatalytic materials are drawing significant attention because of their potential for solving environmental and energy problems which are prevalent challenges in the 21st century[206, 207]. One of the most studied photocatalytic material is titanium dioxide ($TiO_2$) because it has provided the most efficient photocatalytic activity, highest stability, low cost as well as low toxicity[209, 210]. In the photocatalytic reaction, electrons and holes are produced from $TiO_2$ under UV irradiation. The electrons and holes subsequently interact with reactants and form products. One of the major challenges in using unmodified $TiO_2$ as a photocatalyst is that electron-hole recombination leads to low photoconversion

efficiency. The presence of a carbon material such as carbon nanotubes (CNTs) or graphene may reduce the electron-hole recombination via transport of electrons to the conductive carbon materials. The separation of charge may enhance the photoconversion efficiency of $TiO_2$. Indeed, nanocarbon (e.g. CNTs or graphene)/$TiO_2$ composites have shown improved photocatalytic activity over $TiO_2$ in various applications (e.g. the photooxidation of environmental pollutants) [231-234]. The role of carbonaceous nanomaterials in photocatalytic processes has drawn significant attention due to their unique properties and the potential to control their structural and electrical properties[230].

In this work, a new synthesis method for making graphene type carbon/$TiO_2$ composite material was used and the $CO_2$ photocatalytic reaction in the presence of water vapor was studied. The graphene type carbon and $TiO_2$ nanoparticles were well mixed in solution to form a nanocomposite material.

In this work, the graphite layers were separated by oxidizing natural graphite to form graphite oxide, and subsequently functionalizing graphite oxide with $NH_2$ terminated ionic liquid. At the same time graphite oxide was reduced to reduced graphite oxide (RGO) in a basic reaction environment. The high solubility of the ionic liquid in water makes it possible for an ionic liquid functionalized reduced graphite oxide (IL-RGO) to mix well with $TiO_2$ nanoparticles in water. Moreover, the ionic liquid, which is functionalized to the RGO surface, has charge. The charge repulsion may help to further separate the graphite layers. The high surface area of layer-separated graphite material may enhance the adsorption of the reactants, i.e. $CO_2$ and $H_2O$ vapor, thus creating

more reactive sites. In addition, it was reported that a $NH_2$- ionic liquid cation has significantly enhanced ability to uptake $CO_2$ via amine group-$CO_2$ interaction[338]. Therefore, a functionalized ionic liquid with an amine group may also enhance the adsorption of $CO_2$. The experimental results in the previous research illustrated in Chapter 3 show that the ionic liquid of $C_4$mimCl cannot interact with alkanes. Methane ($CH_4$) is a potential product of the $CO_2$ photoreduction using $TiO_2$ or modified $TiO_2$ catalyst. Therefore, the ionic liquid may be able to selectively adsorb the reactant, $CO_2$, but lead to the quick dissociation of the potential product, $CH_4$, thus promoting the photoreduction of $CO_2$.

The IL-RGO/$TiO_2$ nanocomposite was applied to reduce the $CO_2$ in the presence of $H_2O$ vapor. Moreover, the $CO_2$ photoreduction product formation over IL-RGO/$TiO_2$ was compared with the product formation over pristine $TiO_2$ (P25) and other published studies using modified $TiO_2$ in order to provide an initial examination of the selectivity towards products.

## 5.2 Experimental Methods

Synthesis of the ionic liquid reduced graphite oxide/$TiO_2$ (IL-RGO/$TiO_2$) composite involved three basic steps: synthesis of graphite oxide, functionalization and reduction of the graphite oxide in order to make the material more conductive, and addition of the $TiO_2$ to allow for photoactivity.

### 5.2.1 Synthesis of Graphite Oxide

Graphite Oxide (GO) was synthesized from natural graphite powder (325 mesh, Alfa Aesar) by the method of Hummers and Offeman[339]. It was reported that pre-oxidation of the graphite powder was necessary in order to minimize the

potential for incompletely oxidized graphene-core/GO-shell particles to be observed in the final product[340]. The pre-oxidation procedure followed the method of Kovtyukhova *et al.*[340]. Briefly, the pre-oxidation process used concentrated $H_2SO_4$, $K_2S_2O_8$ and $P_2O_5$ to oxidize the graphite powder. The resultant product was subsequently thermally isolated and allowed to cool to room temperature. After cooling, the product was diluted and washed with distilled water until the water's pH became neutral. The product was dried in air at ambient temperature overnight, and subjected to oxidation using Hummers and Offeman's method. The pre-oxidized graphite powder was further oxidized using 0 ℃ cold concentrated $H_2SO_4$ and $KMnO_4$. The reaction was terminated by the addition of a large amount of distilled water and 30% $H_2O_2$ solution. The mixture was centrifuged with 1:10 HCl solution to remove metal ions. Also, additional distilled water washing was done to the mixture until a neutral pH was achieved. The mixture was dark brown in color. The GO was added to distilled water and ultrasonicated for 15 minutes to separate the GO layers. The GO solution was used for the following synthesis. For the material characterization of GO, the GO solution was dried at the room temperature.

### 5.2.2 Ionic Liquid Functionalized Reduced Graphite Oxide (IL-RGO)

The overall reaction for the synthesis of IL-RGO is presented in Figure 5.1. A $NH_2$ terminated ionic liquid of 1-butyl-3-methylimidazolium chloride ($NH_2$-$C_4$mimCl) was synthesized using a process that has been reported previously for the synthesis of amine-terminated 1-butyl-3-methylimidazolium bromide ($NH_2$-$C_4$mimBr) [336, 341]. First, 3-chloropropylamine hydrochloride

(Sigma Aldrich, 98%) and 1-methylimidazole (Sigma Aldrich, ≥99%) were added to ethanol (Sigma Aldrich, ≥99.5%). Second, the mixture was refluxed under nitrogen for 24 hours. The resulting turbid mixture was purified by re-crystallization from ethanol and ethyl acetate as anti-solvent. Finally, the resulting ionic liquid was dried under $N_2$ at 60 ℃ overnight. The $C_4$mimCl functionalized RGO synthesis is based on an epoxide ring-opening reaction between GO and $NH_2$-$C_4$mimCl. $NH_2$-$C_4$mimCl was added into a GO dispersed solution. The salt effect of the GO sheet occurred due to the presence of the ionic liquid. It is well-known that the epoxide ring-opening reaction could be catalyzed by a base. Therefore, KOH was added into the turbid mixture solution. The solution was subjected to ultrasonication for 30 minutes. Lastly, the homogeneous solution was vigorously stirred at 80 ℃ for 24 hours. The resulting solution was subsequently centrifuged, washed with ethanol and water. Then the IL-RGO solution was ultrasonicated for 30 minutes, stirred for 1 hour, and subsequently subjected to the IL-RGO/$TiO_2$ nanocomposite material synthesis. The IL-RGO solution was dried at the room temperature for the IL-RGO material characterization. For comparison, RGO was synthesized using the same procedure, but without adding the $NH_2$-$C_4$mimCl.

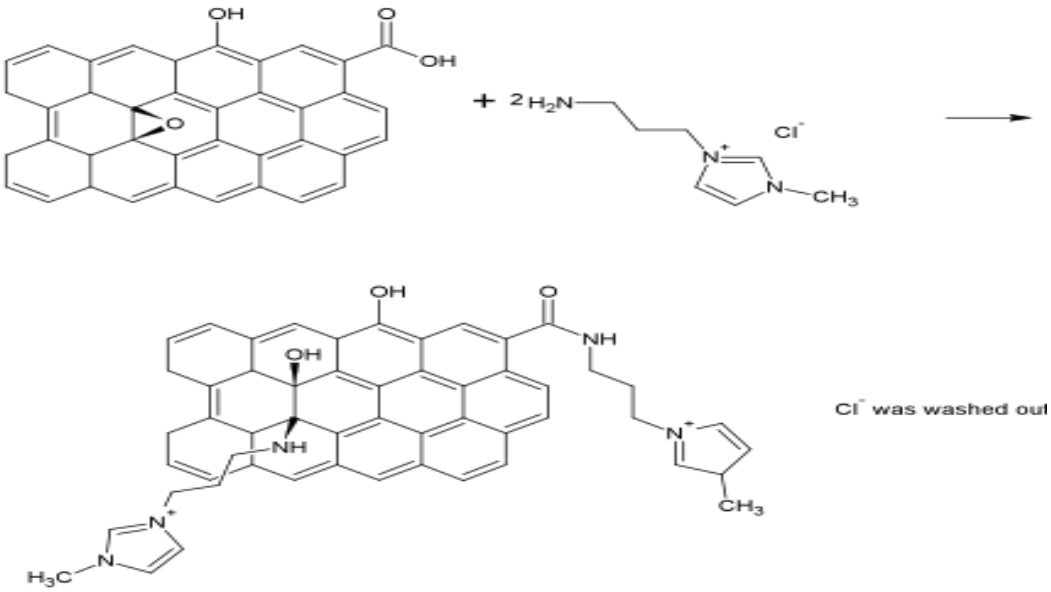


Figure 5.1. Overall synthesis of ionic liquid functionalized reduced graphite oxide (IL-RGO).

### 5.2.3 IL-RGO/$TiO_2$ Nanocomposite Synthesis

$TiO_2$ nanoparticles (Aeroxide Degussa P25) were mixed with distilled water and 1-Butyl-3-methylimidazolium tetrafluoroborate ($C_4mimBF_4$, Sigma Aldrich, ≥98%) ($H_2O$:$C_4mimBF_4$ =9:1 by volume) to make a $TiO_2$ suspension. Subsequently, the IL-RGO solution was added to the $TiO_2$ suspension and vigorously stirred for one hour. Then the IL-RGO/$TiO_2$ mixture was washed with distilled water until the pH is neutral. Then the IL-RGO/$TiO_2$ solution was ultrasonicated for 30 minutes, vigorously stirred for 30 minutes and dried at 90 ℃ overnight. Eventually, the sample was ground to powder for use in the $CO_2$ conversion experiments.

### 5.2.4 Material Characterization

Raman spectra of GO and IL-RGO were collected using a custom built Raman spectrometer in a 180° geometry. The sample was excited using a 100 mW compass 532 nm laser. The data were collected using an Acton 300i spectrograph and a back thinned Princeton Instruments liquid nitrogen cooled CCD detector. The spectral resolution is 3.5 $cm^{-1}$. X-ray Diffraction (XRD) data was obtained using a high resolution X-ray diffractometer (PANALYTICAL X'PERT PRO) using Cu-Kα radiation and an X'celerator detector. Scanning electron microscopy (SEM) was performed using an XL30 ESEM-FEG. X-ray photoelectron spectroscopy (XPS) was performed using a VG ESCALAB 220i-XL aluminum-Kα (1486.6 eV) X-ray source.

### 5.2.5 Photocatalytic Reduction of $CO_2$ with $H_2O$ Vapor

The photoreduction of $CO_2$ experiments were carried out using a Nicolet 6700 Fourier transform infrared (FTIR) spectrometer equipped with a Praying Mantis diffuse reflectance accessory (Harrick Sci. Corp.) and a 316 stainless steel high temperature reaction chamber (Harrick Sci. Corp.), a mercury cadmium telluride (MCT) detector and a KBr beam splitter. The chamber dome has two KBr windows and a quartz window. The quartz window was used for visual observation while the KBr windows were used for permitting entry and exit of the infrared beam. The IL-RGO/$TiO_2$ or pristine Degussa P25 powders were placed in the sample compartment of the reaction chamber, and the dome was mounted and sealed with an O-ring. The reaction chamber has an inlet for introducing gas to the sample and an outlet for gas exhaust. The chamber was purged with $N_2$

before introducing the reactant gases, i.e. $CO_2$ and $H_2O$ vapor. The $H_2O$ vapor was obtained by flowing $N_2$ through an impinge containing distilled water. $CO_2$ mixed with humidified $N_2$ was introduced to the reaction chamber. Mass flow controllers (Omega Engineering, Inc.,) were used to control the flow of $CO_2$ and $N_2$. An IR spectrum was obtained after the $CO_2$/ humidified $N_2$ mixture flowed over the photocatalyst, in order to check that $CO_2$ and $H_2O$ vapor were absorbed to the surface of the catalyst. The inlet and outlet of the chamber were sealed, and subsequent spectra were taken in a batch mode of operation.

A series of background experiments were conducted in order to characterize the system and to ensure the absence of product formation, even in the presence of the catalytic surface. The sample with $CO_2$ and humidified $N_2$ was kept in the dark for 30 minutes. IR spectra were obtained during the 30 minutes in the dark to check whether there was product even without light. In addition, a background experiment with the catalyst and humidified $N_2$ but without $CO_2$ was performed under UV-Visible light irradiation in order to determine whether there was product formation in the absence of $CO_2$. After performing the background experiments, the catalyst (IL-RGO/$TiO_2$ or P25) was placed in the chamber with $CO_2$ and humidified $N_2$. UV-Visible light was produced from a deuterium-halogen light source (Ocean Optics DH-2000-BAL, wavelength =210-1500 nm). An optical fiber cable was used to introduce the light to the sample surface through the quartz window of the chamber. Several IR spectra at different irradiation times were acquired over a total irradiation time of 55 minutes. Each spectrum was acquired using 4 $cm^{-1}$ resolution and 32 scans.

## 5.3 Results and Discussion

### 5.3.1 Material Characterization

The Raman spectra of GO and IL-RGO/$TiO_2$ are shown in Figure 5.2. In the Raman spectrum of GO (Figure 5.2 a), the G band at 1580 $cm^{-1}$ is related to the in-plane vibration of the $sp^2$ bonded carbon atoms[342]. The D band at 1339 $cm^{-1}$ is associated with the vibration of $sp^3$ bonded carbon atoms, which corresponds to the disordered structure of the GO[342]. The D/G band intensity ratio of GO is 1.03. In the Raman spectrum of IL-RGO/$TiO_2$, the D/G band intensity ratio is 0.94. A decrease of the D/G band intensity ratio of IL-RGO suggests that part of the disorder structures were restored to in-plane $sp^2$ structures. The restoration of $sp^2$ carbon structure indicates an increase in the conductivity of the material[343].

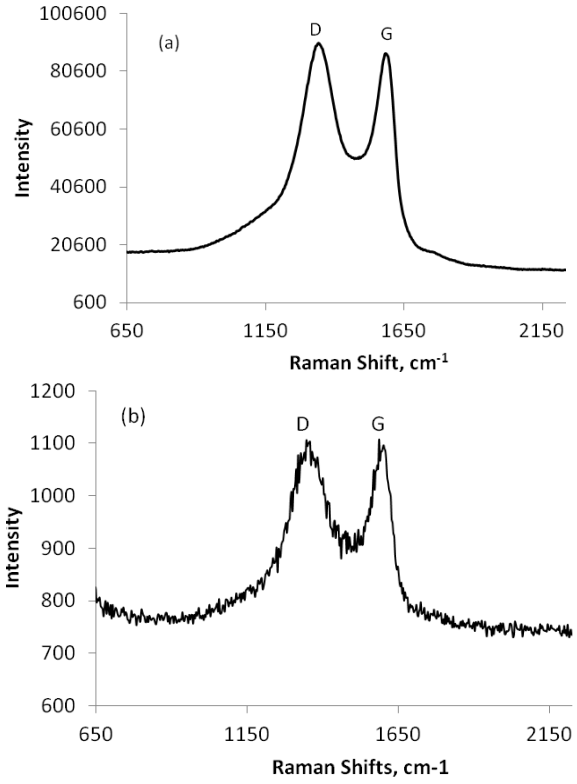


Figure 5.2. Raman spectra of (a) GO and (b) IL-RGO.

X-ray spectroscopy (XPS) was used to characterize the chemical composition of the material. The XPS spectra are presented in Figure 5.3. The wide scan survey (Figure 5.3 a) shows that all the expected elements, Ti, O, C and N, are present in the IL-RGO/$TiO_2$ sample. The anion of the ionic liquid, $Cl^-$, and the elements from the solvents used in the synthesis process (i.e. B and F from $C_4mimBF_4$) were double checked using high resolution XPS spectrum. No peak associated with Cl or the elements of B and F from $C_4mimBF_4$ was found. Therefore, $Cl^-$ and $C_4mimBF_4$ were completely washed out of the sample. The high resolution XPS spectrum of N1s in IL-RGO (Figure 5.3 b) shows that the N1s band appears at 401.7 eV, with a lower binding energy shoulder at 399.8 eV. This confirms the presence of the IL-$NH_2$ unit in IL-RGO[336]. In addition, the small peak of C-N at 286.3 eV in the high resolution XPS spectrum of C1s in IL-RGO (Figure 5.3 d) further confirms that the $NH_2$ terminated ionic liquid was present in the sample[336].

The atomic concentration ratio of carbon/oxygen (C/O) in GO determined using the XPS data is 0.8, while the atomic concentration ratio of C/O in IL-RGO determined using the XPS data is 1.4. The atomic concentration of the C-N peak shown in Figure 5.3 (d) contributes to 2.6% of the total carbon from the IL-RGO. According to the molecular structure of attached ionic liquid, the maximum percentage of carbon content that could be introduced to IL-RGO by simply attaching the ionic liquid is 6.1%. The calculations are presented in Table A-3 (Appendix). If we assume that the atomic concentration of oxygen does not change in the process of GO conversion to IL-RGO, the maximum C/O should be

0.9. However, the C/O in IL-RGO is 1.4. Therefore, a large number of oxygen groups disappeared in the synthesis of the IL-RGO sample and it is not simply due to the attachment of the ionic liquid; hence, GO was significantly reduced. High resolution XPS spectra of C1s in GO and IL-RGO are shown in Figure 5.3 (c) and (d), respectively. Carbon has multiple binding configurations, including graphite C=C, C=O, C-OH, and C in the epoxide/ether. Comparing the peaks for different binding configurations, the atomic concentration of the graphite peak (C=C) in GO is 18.6% of carbon in all binding configurations. The atomic concentration of graphite peak in IL-RGO accounts for 50.4% of that of the carbon in all binding configurations. This confirms that partial $sp^2$ graphite structures were restored. In addition, when the IL-RGO was synthesized from GO, the color of the sample changed from dark-brown to dark-gray. The change in color strongly suggests that GO was reduced.

The X-ray diffraction (XRD) data (Figure 5.4) show that the diffraction peak of GO appears at $2\theta=12.2°$. This corresponds to an average interlayer space of 0.72 nm. The XRD peak for RGO without functionalized IL appears at $2\theta=12.7°$, corresponding to the average interlayer spacing of 0.70 nm, whereas IL-RGO has a weak and broad diffraction peak at $2\theta=11°$. As compared to GO, the slightly reduced interlayer space of RGO is likely due to the decreased number of oxygen groups. The calculated interlayer spaces of GO and RGO demonstrate that the interlayer spaces are similar within the GO structure and RGO structure. Different from the sharp XRD peaks of GO (Figure 5.4 a) and RGO (Figure 5.4 b), the broad X-ray diffraction peak of IL-RGO with low

intensity may be because different interlayer spaces were obtained after the ionic liquid functionalization. It indicates that exfoliation of layered IL-RGO was obtained[336].

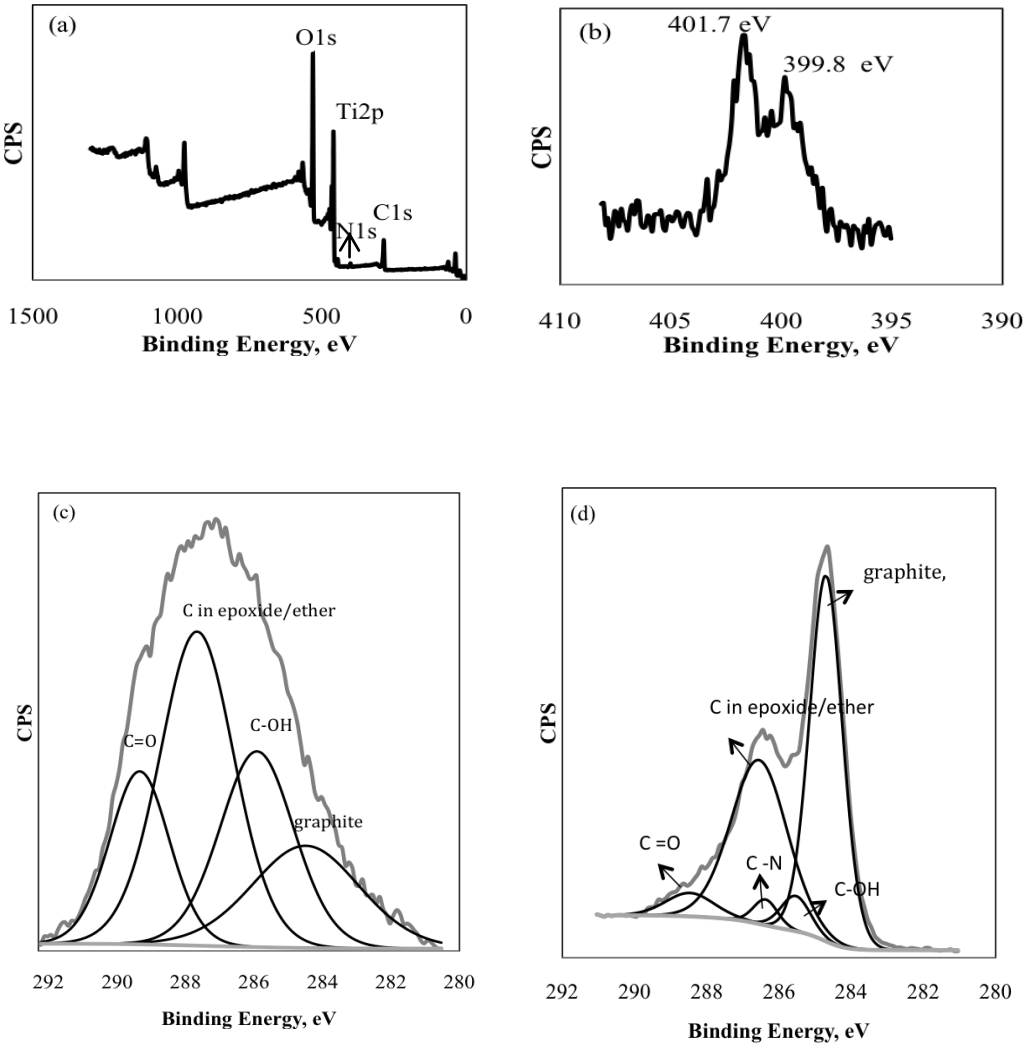


Figure 5.3. XPS spectra (a) wide scan survey of IL-RGO/$TiO_2$ (b) high resolution XPS spectrum of N1s in IL-RGO (c) high resolution XPS spectrum of C1s in GO (d) high resolution XPS spectrum of C1s in IL-RGO.

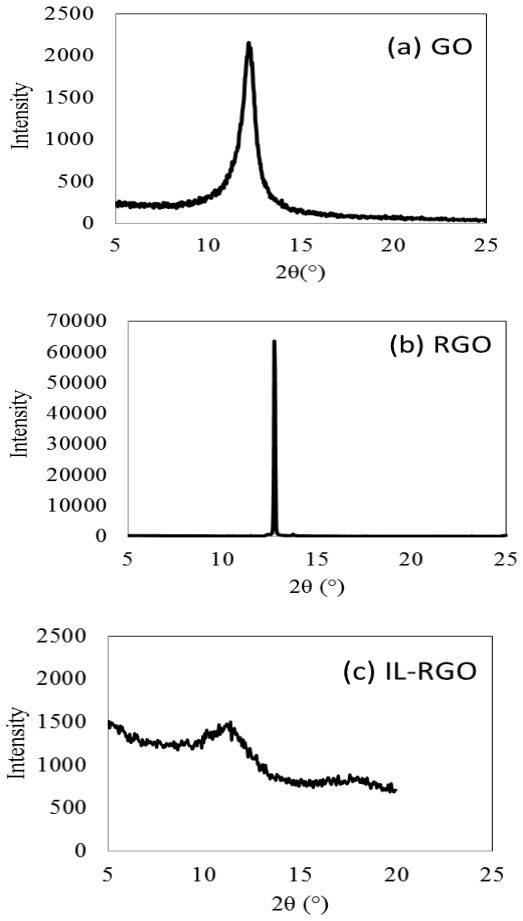


Figure 5.4. X-ray Diffraction (XRD) peaks of (a) GO, (b) RGO, and (c) IL-RGO.

The scanning electron micrographs (SEM) of IL-RGO/$TiO_2$ and RGO/$TiO_2$ with the same RGO carbon /$TiO_2$ ratio are shown in Figure 5.5. The separated RGO flakes can be clearly seen in the IL-RGO/$TiO_2$ sample. However, the RGO aggregates in the RGO/$TiO_2$ sample. Without the functionalized IL, the RGO particles are much larger and aggregate together. A few $TiO_2$ nanoparticles are above the RGO aggregates. The majority of $TiO_2$ nanoparticles are covered by the RGO. Due to the thickness of the muti-layer RGO, the $TiO_2$ nanoparticles below the RGO cannot be clearly seen in the SEM image. The SEM images

reveal that better separation of the graphite layers can be obtained in IL-RGO. The presence of the functionalized ionic liquid enhances the solubility of functionalized reduced graphite oxide in water[336]. Thus, a well-mixed IL-RGO and $TiO_2$ could be obtained in solution.

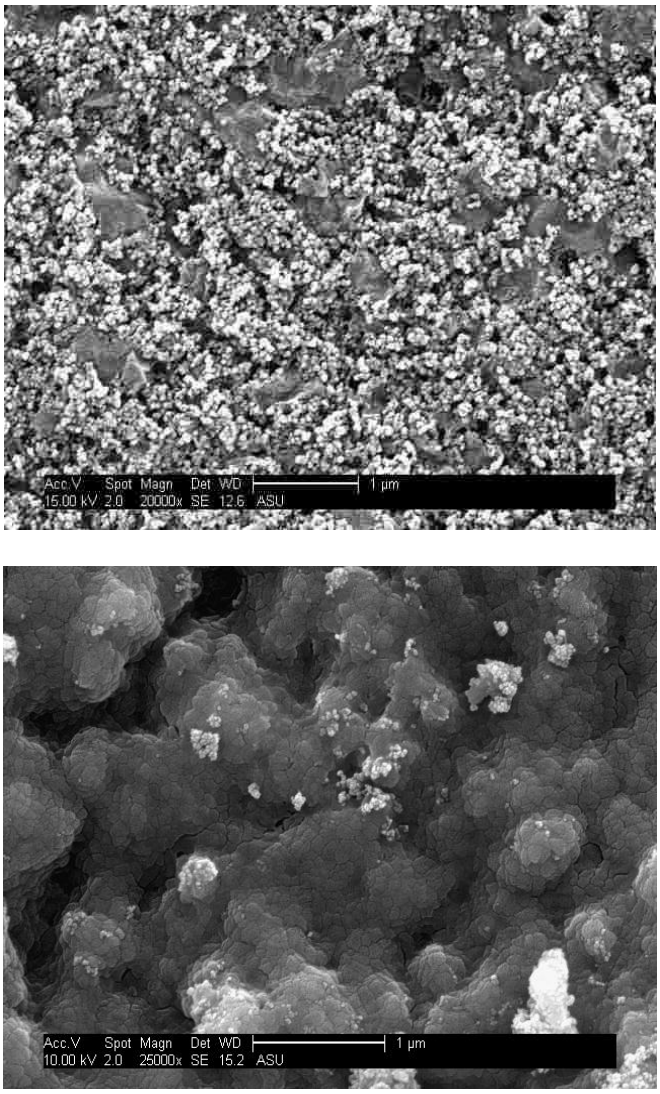


Figure 5.5. SEM images of (above) IL-RGO/$TiO_2$ and (below) RGO/$TiO_2$.

### 5.3.2 Photocatalytic Reduction of $CO_2$

In the background experiments, no new peaks were observed in the IR spectra of IL-RGO/$TiO_2$ with $CO_2$ and humidified $N_2$ in the dark for 30 minutes. When IL-RGO/$TiO_2$ and humidified $N_2$ (in the absence of $CO_2$) were irradiated for 30 minutes using UV-Vis light, no new peaks were detected in the IR spectra. Experiments were also performed for bare P25 with $CO_2$ and humidified $N_2$. Even after 60 minutes of UV-Vis irradiation, no new peak formation was detected in the IR spectra.

The IL-RGO/$TiO_2$ composite material was applied to the photoreduction of $CO_2$ in the presence of $H_2O$ vapor. IR spectra of the IL-RGO/$TiO_2$ surface before and after UV-Visible irradiation were obtained (see Figure 5.6). After only 40 seconds of irradiation, new IR features started to appear in the spectrum. In going from 40 seconds to 60 minutes of irradiation, a new peak at 3017 $cm^{-1}$ continued to grow in intensity. The new peak was initially identified by comparison to the literature [326] as being characteristic of $CH_4$. In addition, an IR spectrum of pure $CH_4$ over IL-RGO/$TiO_2$ was obtained in-house and compared with the product's IR spectrum (see Figure A-4 in Appendix). A comparison confirmed that $CH_4$ was indeed the product from reduction of $CO_2$. The background experiments of IL-RGO/$TiO_2$ with $H_2O$ vapor but without $CO_2$ showed that no peak formed after 30 minutes of UV-Vis irradiation (see Figure 5.7), thus confirming that $CH_4$ was indeed formed from $CO_2$ reduction in the presence of water vapor rather than from other carbon sources (i.e. RGO or the attached ionic liquid).

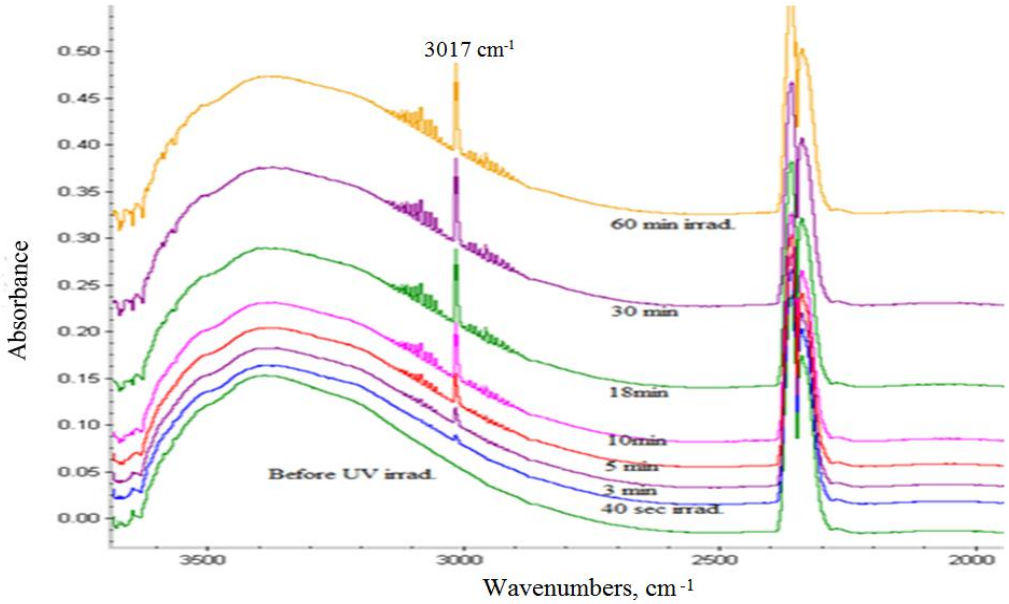


Figure 5.6. The IR spectra of IL-RGO/$TiO_2$ surface with $CO_2$ and $H_2O$ vapor before and after UV-Visible light irradiation. The IR spectrum of IL-RGO/$TiO_2$ was used as a background. The IR spectra were offset for clarification.

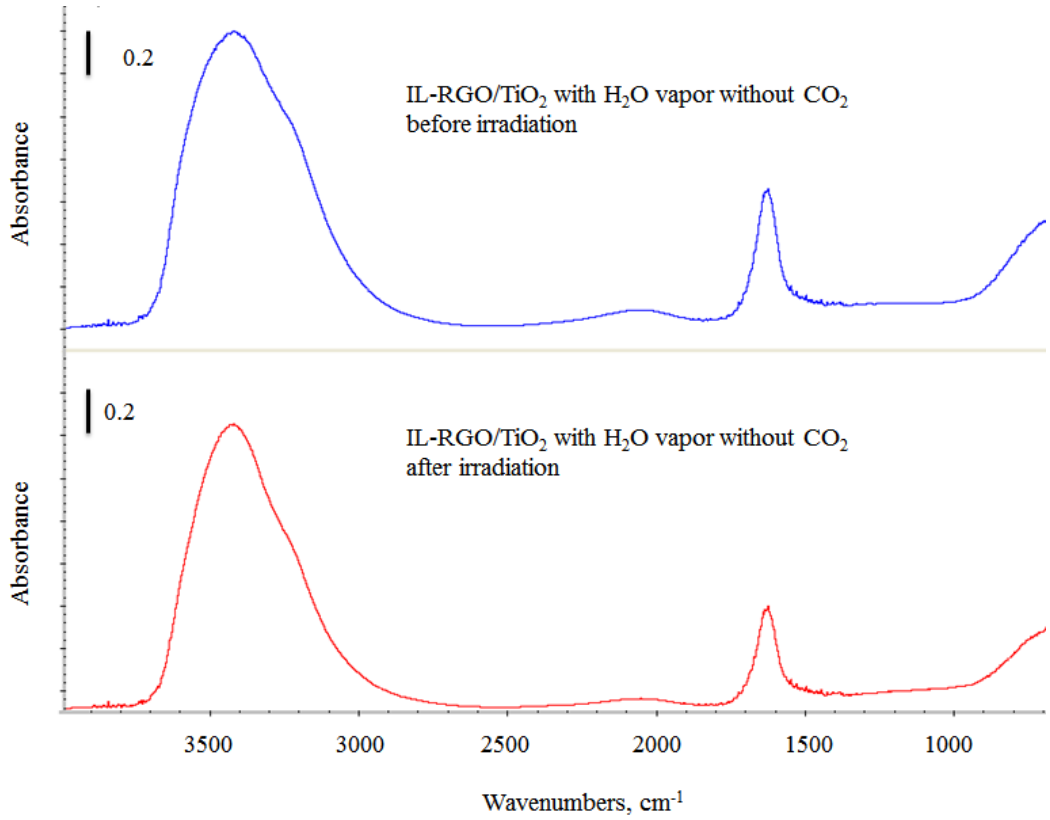


Figure 5.7. The IR spectra of IL-RGO/$TiO_2$ with $H_2O$ but without $CO_2$ before and after 30 minute UV-Visible irradiation.

The major challenge in $CO_2$ photoreduction is that the recombination of electron and hole generated from $TiO_2$ is very fast. Thus, there is a significant decrease in the photocatalytic efficiency of $TiO_2$. P25, which is the mixed phases of $TiO_2$ with ~75% anatase and ~25% rutile, is expected to have better electron and hole separation than single phase of $TiO_2$ due to the different positions of the conduction and valence bands of the anatase and rutile phases. Electron paramagnetic resonance (EPR) studies by Gray and co-workers indicated that photogenerated electrons actually migrated from rutile to lower energy anatase trapping sites, consequently, enhance the electron and hole separation[212, 344, 345].

However, no product was observed under the DRIFTS experimental conditions. Therefore, the commercial P25 is still not effective enough for photoreduction of $CO_2$ with $H_2O$ vapor. Nevertheless, the presence of IL-RGO significantly enhances the photoactivity of P25 which is very likely due to the improved electron-hole separation via electron transport to the IL-RGO.

The production of CO was frequently reported in the literature as the major product for $CO_2$ photoreduction studies using $TiO_2$ –based nanoparticles[346] [228]. The IR feature of CO is expected to appear in the 2000-2270 $cm^{-1}$ frequency range [326]. The lack of CO features in Figure 5.6 suggests that there is insignificant production of CO and $CH_4$ is the only product of $CO_2$ photoreduction in the presence of water vapor over IL-RGO/$TiO_2$.

In the literature, there are different proposed mechanisms for $CH_4$ formation in $CO_2$ photoreduction using $TiO_2$ based photocatalyst. One mechanism has CO formation as the first step while the other mechanism suggests $CO_2^-$ formation is the critical step. The reactions for the two mechanisms were shown in Chapter 1, Reaction 1.1-1.13. However, both of the reaction mechanisms suggest that eight electrons are required for $CH_4$ production. The selectivity of product, CO or $CH_4$, may be due to different numbers of electrons that are produced by the catalyst and separated from hole. The reaction mechanism for CO production requires four electrons[227], while more electrons (eight electrons) are needed for $CH_4$ production. The $CH_4$ selectivity in this work also indicates that more electrons are separated for the photocatalyst of IL-RGO/$TiO_2$ as compared to the catalysts in the literatures, which have CO as the major product

in $CO_2$ photoreduction. This further confirms that the presence of IL-RGO helps to separate electron and hole pairs. The selective production of $CH_4$ is very important for application of the catalyst in $CO_2$ photoreduction. It is because CO, as a synthesis gas, cannot be used as a fuel directly whereas $CH_4$ is an energy-rich fuel.

To attempt to quantify the amount of $CH_4$ formed, standard samples of $CH_4$ (diluted by $N_2$) were admitted to the DRIFTS reaction cell to generate a calibration curve. The gas was allowed to equilibrate with the surface, a spectrum was obtained, and the surface was subsequently purged with $N_2$ in between each admission of $CH_4$. Spectra were acquired during the $N_2$ purge to ensure that the $CH_4$ was completely desorbed from the surface and removed from the chamber. A surface adsorbed $CH_4$ calibration curve was generated and used to attempt to quantify the amount of $CH_4$ formed during the $CO_2$ photoreduction experiment over IL-RGO/$TiO_2$. The calibration curve of $CH_4$ is shown in Figure A-4 (Appendix).

The $CO_2$ photoreduction using IL-RGO/$TiO_2$ catalyst in the presence of $H_2O$ vapor was performed twice using fresh and regenerated catalyst samples. Initially, fresh IL-RGO/$TiO_2$ was used for $CO_2$ photoreduction. After 30 minute UV-Visible irradiation, the sample was regenerated by cleaning up the catalyst surface using pure $N_2$. IR spectrum of the catalyst was obtained to make sure that the reactants, $CO_2$ and $H_2O$ vapor, and the product of $CH_4$ formed in the previous reaction completely dissociate from the catalyst surface and removed from the reaction chamber. Then, the reactants with the same concentrations were admitted

to the reaction chamber and the photoreduction experiment was performed again. The concentration of $CH_4$ formed at different UV-Visible irradiation times by fresh IL-RGO/$TiO_2$ catalyst and regenerated IL-RGO/$TiO_2$ catalyst are shown in Figure 5.8. The results show that the regenerated sample can produce almost identical amount of $CH_4$ at the same irradiation times. Therefore, the IL-RGO/$TiO_2$ catalyst can be regenerated and effectively reused in $CO_2$ photoreduction. This result is very important regarding the application of this material in real-world $CO_2$ photoreduction. The $CH_4$ production rate of 279 μmol/g catalyst-hr over a 55 minute period was calculated. The calculation details can be found in the Appendix Table A-4. The $CH_4$ production rate is about 18 times higher as compared to the highest $CH_4$ production rate using other modified $TiO_2$ reported in the literature[253].

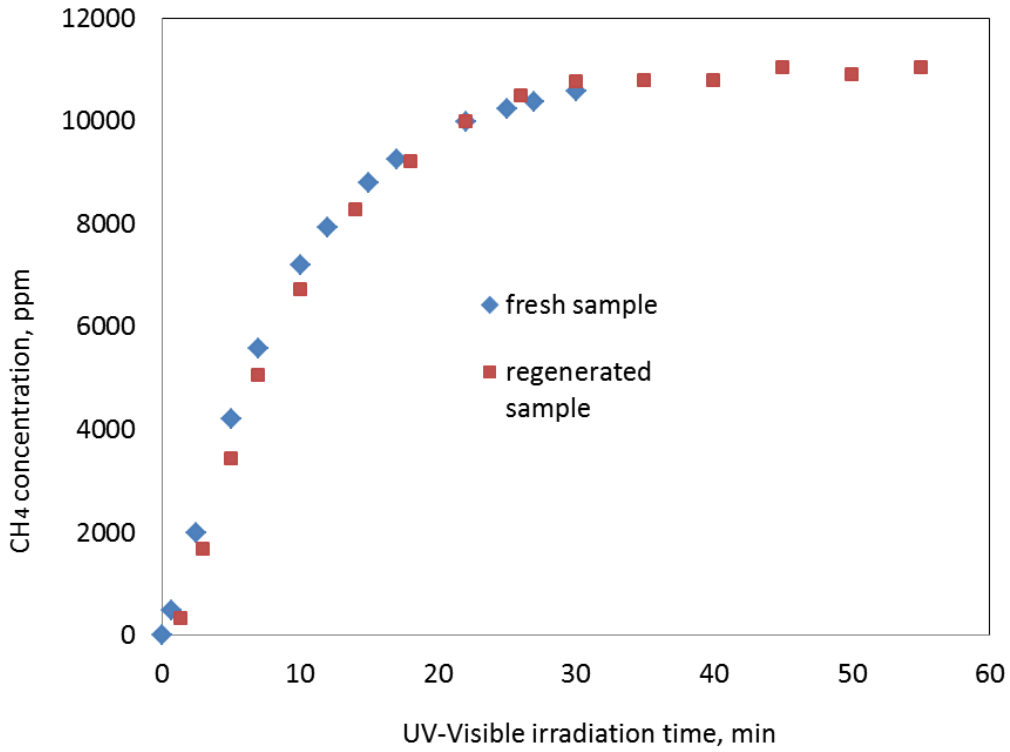


Figure 5.8. The concentration of methane over IL-RGO/$TiO_2$ and regenerated sample by cleaning the surface using $N_2$ at different UV-Visible irradiation times.

## 5.4 Conclusion

A new method was used to synthesize a carbon/semiconductor composite material via attaching ionic liquid to graphite oxide surface to obtain the ionic liquid functionalized reduced graphite oxide (IL-RGO), and mixing it with $TiO_2$ nanoparticles in solution. The successful synthesis of this material was confirmed by Raman spectroscopy, XRD, XPS and SEM. As compared to RGO without the functionalized ionic liquid, IL-RGO layers were separated and IL-RGO flakes could be clearly seen in the SEM images. In addition, the SEM images showed that $TiO_2$ nanoparticles were dispersed within the IL-RGO flakes. The photoreduction of $CO_2$ over IL-RGO/ $TiO_2$ in the presence of $H_2O$ vapor was

investigated using Diffuse Reflectance Infrared Fourier Transform Spectroscopy (DRIFTS). $CH_4$ was formed after just 40 seconds of UV-Vis irradiation over the catalyst of IL-RGO/ $TiO_2$, and the IR features of $CH_4$ increased as the irradiation time increased. However, no product was found for the photoreduction of commercial P25 under the same experimental conditions. Therefore, the presence of IL-RGO significantly enhanced the photocatalytic activity of P25 due to the enhanced electron-hole separation. In addition, $CH_4$ was found to be the only product for IL-RGO/$TiO_2$.

The regeneration and reuse of IL-RGO/$TiO_2$ catalyst for $CO_2$ photoreduction were investigated. The regenerated catalyst produced an almost identical amount of $CH_4$ at the same irradiation times. A $CH_4$ production rate of 279 μmol/g catalyst-hr over a 55 minute period was calculated. This calculated $CH_4$ production rate is much higher than those reported in the literature.

# CHAPTER 6

## FUTURE WORK FOR $CO_2$ PHOTOREDUCTION

The ultimate goal of using photocatalyst material for $CO_2$ photoreduction is to design an efficient photocatalyst and utilize sunlight as the only energy input. Besides the challenge of electron-hole recombination of unmodified $TiO_2$, another challenge of using $TiO_2$ is that $TiO_2$ can only be excited by UV light due to its wide band gap (~3.2 eV for anatase and 3.0 eV for rutile). However, UV light only accounts for less than 5% of the total solar energy. To design modified $TiO_2$ that is useful for $CO_2$ photoreduction under visible light is important.

To obtain visible light responsiveness, many researchers have doped $TiO_2$ with a variety of nonmetal ions, such as S, N, B and F[347-350]. These dopings create intra-band-gap states that are close to the conduction or valence band edges[351]. Visible light absorption can then be induced at sub-band-gap energies. Unlike metal ions, nonmetal ions are more efficient in enhancing visible light activity due to their lower likelihood to form electron and hole recombination centers[209]. However, little research has been conducted to date on $CO_2$ photoreduction using nonmetal doped $TiO_2$ under visible light.

Recently, iodine (I) has been doped into $TiO_2$ and improved visible light activity towards the decomposition of organic compounds has been seen[227, 352-354]. Compared to other nonmetal ions which substitute the lattice oxygen of $TiO_2$, iodine was reported to replace lattice Ti, due to the close ionic radii of $I^{5+}$ and $Ti^{4+}$ [351, 352]. The substitution of $Ti^{4+}$ with $I^{5+}$ may introduce charge imbalance, which leads to the formation of $Ti^{3+}$ surface states. It was reported that the generation of

$Ti^{3+}$ may trap the photoelectron and transfer them to the reactants on the surface of $TiO_2$[351]. Additionally, the XPS study conducted by Tojo *et al.*[355] indicated that doped $I^{5+}$ can effectively trap electrons via $I^{5+} \rightarrow I^-$, and thus reduce electron and hole recombination. Therefore, the I-doped $TiO_2$ is expected to not only absorb visible light but also enhance catalytic activity of $CO_2$ photoreduction due to the potential of iodine to reduce electron-hole recombination.

The future work can be extended to design I-doped $TiO_2$/IL-RGO nanocomposite material and apply it for $CO_2$ photoreduction in the presence of water vapor. In the past work, IL-RGO has shown its ability to enhance the electron and hole separation. IL-RGO/$TiO_2$ has demonstrated significantly enhanced photocatalytic activity as compared to bare $TiO_2$ (Degussa P25). The iodine doped $TiO_2$ is expected to extend its light absorption to visible light range. Therefore, I-doped $TiO_2$/IL-RGO nanocomposite material may be able to efficiently convert $CO_2$ to fuels under sunlight irradiation.

REFERENCES

1. Haagensmit, A. J., CHEMISTRY AND PHYSIOLOGY OF LOS-ANGELES SMOG. *Industrial and Engineering Chemistry* 1952, 44, 1342-1346.

2. Lelieveld, J.; Berresheim, H.; Borrmann, S.; Crutzen, P. J.; Dentener, F. J.; Fischer, H.; Feichter, J.; Flatau, P. J.; Heland, J.; Holzinger, R.; Korrmann, R.; Lawrence, M. G.; Levin, Z.; Markowicz, K. M.; Mihalopoulos, N.; Minikin, A.; Ramanathan, V.; de Reus, M.; Roelofs, G. J.; Scheeren, H. A.; Sciare, J.; Schlager, H.; Schultz, M.; Siegmund, P.; Steil, B.; Stephanou, E. G.; Stier, P.; Traub, M.; Warneke, C.; Williams, J.; Ziereis, H., Global air pollution crossroads over the Mediterranean. *Science* 2002, 298, 794-799.

3. Solomon, P.; Cowling, E.; Hidy, G.; Furiness, C., Comparison of scientific findings from major ozone field studies in North America and Europe. *Atmospheric Environment* 2000, 34, 1885-1920.

4. Went, F. W.; Slemmons, D. B.; Mozingo, H. N., ORGANIC NATURE OF ATMOSPHERIC CONDENSATION NUCLEI. *Science* 1967, 156, 543-&.

5. Jacobson, M. C.; Hansson, H. C.; Noone, K. J.; Charlson, R. J., Organic atmospheric aerosols: Review and state of the science. *Reviews of Geophysics* 2000, 38, 267-294.

6. Seinfeld, J. H.; Pankow, J. F., Organic atmospheric particulate material. *Annual Review of Physical Chemistry* 2003, 54, 121-140.

7. Watson, J. G., Visibility: Science and regulation. *Journal of the Air & Waste Management Association* 2002, 52, 628-713.

8. Tuazon, E. C.; Atkinson, R., A PRODUCT STUDY OF THE GAS-PHASE REACTION OF ISOPRENE WITH THE OH RADICAL IN THE PRESENCE OF NOX. *International Journal of Chemical Kinetics* 1990, 22, 1221-1236.

9. Bonn, B.; Moortgat, G. K., Sesquiterpene ozonolysis: Origin of atmospheric new particle formation from biogenic hydrocarbons. *Geophysical Research Letters* 2003, 30.

10. Claeys, M.; Graham, B.; Vas, G.; Wang, W.; Vermeylen, R.; Pashynska, V.; Cafmeyer, J.; Guyon, P.; Andreae, M. O.; Artaxo, P.; Maenhaut, W., Formation of secondary organic aerosols through photooxidation of isoprene. *Science* 2004, 303, 1173-1176.

11. Griffin, R. J.; Cocker, D. R.; Seinfeld, J. H.; Dabdub, D., Estimate of global atmospheric organic aerosol from oxidation of biogenic hydrocarbons. *Geophysical Research Letters* 1999, 26, 2721-2724.

12. Kulmala, M., How particles nucleate and grow. *Science* 2003, 302, 1000-1001.

13. Saathoff, H.; Naumann, K. H.; Schnaiter, M.; Schock, W.; Mohler, O.; Schurath, U.; Weingartner, E.; Gysel, M.; Baltensperger, U., Coating of soot and (NH4)(2)SO4 particles by ozonolysis products of alpha-pinene. *Journal of Aerosol Science* 2003, 34, 1297-1321.

14. US Environmental Protection Agency, An Introduction to Indoor Air Quality (IAQ), Volatile Organic Compounds (VOCs), http://www.epa.gov/iaq/voc.html.

15. Fraser, M. P.; Cass, G. R.; Simoneit, B. R. T., Gas-phase and particle-phase organic compounds emitted from motor vehicle traffic in a Los Angeles roadway tunnel. *Environmental Science & Technology* 1998, 32, 2051-2060.

16. Andreae, M. O.; Merlet, P., Emission of trace gases and aerosols from biomass burning. *Global Biogeochemical Cycles* 2001, 15, 955-966.

17. McDonald, J. D.; Zielinska, B.; Fujita, E. M.; Sagebiel, J. C.; Chow, J. C.; Watson, J. G., Emissions from charbroiling and grilling of chicken and beef. *Journal of the Air & Waste Management Association* 2003, 53, 185-194.

18. Fortmann, R.; Roache, N.; Chang, J. C. S.; Guo, Z., Characterization of emissions of volatile organic compounds from interior alkyd paint. *Journal of the Air & Waste Management Association* 1998, 48, 931-940.

19. Fall, R.; Karl, T.; Hansel, A.; Jordan, A.; Lindinger, W., Volatile organic compounds emitted after leaf wounding: On-line analysis by proton-transfer-reaction mass spectrometry. *Journal of Geophysical Research-Atmospheres* 1999, 104, 15963-15974.

20. Kirstine, W.; Galbally, I.; Ye, Y. R.; Hooper, M., Emissions of volatile organic compounds (primarily oxygenated species) from pasture. *Journal of Geophysical Research-Atmospheres* 1998, 103, 10605-10619.

21. Placet, B. M.; Rehsenfeld, R. E.; Bassett, G. W., Emissions involved in acidic deposition processes. Sate-of-Science/Technology Report 1. National acid precipitation assessment program. U.S. Government Printing Office, Washington, DC.

22. Middleton, P., *Sources of air pollutants, in Composition, Chemistry, and Climate of the Atmosphere, edited by H. B. Singh*. Van Nostrand Reinhold, New York: 1995.

23. Piccot, S. D.; Watson, J. J.; Jones, J. W., A GLOBAL INVENTORY OF VOLATILE ORGANIC-COMPOUND EMISSIONS FROM

ANTHROPOGENIC SOURCES. *Journal of Geophysical Research-Atmospheres* 1992, 97, 9897-9912.

24. Guenther, A.; Hewitt, C. N.; Erickson, D.; Fall, R.; Geron, C.; Graedel, T.; Harley, P.; Klinger, L.; Lerdau, M.; McKay, W. A.; Pierce, T.; Scholes, B.; Steinbrecher, R.; Tallamraju, R.; Taylor, J.; Zimmerman, P., A GLOBAL-MODEL OF NATURAL VOLATILE ORGANIC-COMPOUND EMISSIONS. *Journal of Geophysical Research-Atmospheres* 1995, 100, 8873-8892.

25. Went, F. W., ORGANIC MATTER IN THE ATMOSPHERE, AND ITS POSSIBLE RELATION TO PETROLEUM FORMATION. *Proceedings of the National Academy of Sciences of the United States of America* 1960, 46, 212-221.

26. Arneth, A.; Monson, R. K.; Schurgers, G.; Niinemets, U.; Palmer, P. I., Why are estimates of global terrestrial isoprene emissions so similar (and why is this not so for monoterpenes)? *Atmospheric Chemistry and Physics* 2008, 8, 4605-4620.

27. Bao, H.; Kondo, A.; Kaga, A.; Tada, M.; Sakaguti, K.; Inoue, Y.; Shimoda, Y.; Narumi, D.; Machimura, T., Biogenic volatile organic compound emission potential of forests and paddy fields in the Kinki region of Japan. *Environmental Research* 2008, 106, 156-169.

28. Bao, H.; Shrestha, K. L.; Kondo, A.; Kaga, A.; Inoue, Y., Modeling the influence of biogenic volatile organic compound emissions on ozone concentration during summer season in the Kinki region of Japan. *Atmospheric Environment* 2010, 44, 421-431.

29. Chiriac, R.; Carre, J.; Perrodin, Y.; Fine, L.; Letoffe, J. M., Characterisation of VOCs emitted by open cells receiving municipal solid waste. *Journal of Hazardous Materials* 2007, 149, 249-263.

30. Chiriac, R.; Carre, J.; Perrodin, Y.; Vaillant, H.; Gasso, S.; Miele, P., Study of the dispersion of VOCs emitted by a municipal solid waste landfill. *Atmospheric Environment* 2009, 43, 1926-1931.

31. Ekberg, A.; Arneth, A.; Hakola, H.; Hayward, S.; Holst, T., Isoprene emission from wetland sedges. *Biogeosciences* 2009, 6, 601-613.

32. Faubert, P.; Tiiva, P.; Rinnan, A.; Michelsen, A.; Holopainen, J. K.; Rinnan, R., Doubled volatile organic compound emissions from subarctic tundra under simulated climate warming. *New Phytologist* 2010, 187, 199-208.

33. Geron, C. D.; Arnts, R. R., Seasonal monoterpene and sesquiterpene emissions from Pinus taeda and Pinus virginiana. *Atmospheric Environment* 2010, 44, 4240-4251.

34. Karl, T.; Harren, F.; Warneke, C.; de Gouw, J.; Grayless, C.; Fall, R., Senescing grass crops as regional sources of reactive volatile organic compounds. *Journal of Geophysical Research-Atmospheres* 2005, 110.

35. Kegge, W.; Pierik, R., Biogenic volatile organic compounds and plant competition. *Trends in Plant Science* 2010, 15, 126-132.

36. Ortega, J.; Helmig, D.; Daly, R. W.; Tanner, D. M.; Guenther, A. B.; Herrick, J. D., Approaches for quantifying reactive and low-volatility biogenic organic compound emissions by vegetation enclosure techniques - Part B: Applications. *Chemosphere* 2008, 72, 365-380.

37. Janson, R.; De Serves, C.; Romero, R., Emission of isoprene and carbonyl compounds from a boreal forest and wetland in Sweden. *Agricultural and Forest Meteorology* 1999, 98-9, 671-681.

38. Janson, R.; de Serves, C., Acetone and monoterpene emissions from the boreal forest in northern Europe. *Atmospheric Environment* 2001, 35, 4629-4637.

39. Li, D. W.; Shi, Y.; He, X. Y.; Chen, W.; Chen, X., Volatile organic compound emissions from urban trees in Shenyang, China. *Botanical Studies* 2008, 49, 67-72.

40. Ortega, J.; Helmig, D.; Guenther, A.; Harley, P.; Pressley, S.; Vogel, C., Flux estimates and OH reaction potential of reactive biogenic volatile organic compounds (BVOCs) from a mixed northern hardwood forest. *Atmospheric Environment* 2007, 41, 5479-5495.

41. Otter, L. B.; Guenther, A.; Greenberg, J., Seasonal and spatial variations in biogenic hydrocarbon emissions from southern African savannas and woodlands. *Atmospheric Environment* 2002, 36, 4265-4275.

42. Ruuskanen, T. M.; Kolari, P.; Back, J.; Kulmala, M.; Rinne, J.; Hakola, H.; Taipale, R.; Raivonen, M.; Altimir, N.; Hari, P., On-line field measurements of monoterpene emissions from Scots pine by proton-transfer-reaction mass spectrometry. *Boreal Environment Research* 2005, 10, 553-567.

43. Sakulyanontvittaya, T.; Duhl, T.; Wiedinmyer, C.; Helmig, D.; Matsunaga, S.; Potosnak, M.; Milford, J.; Guenther, A., Monoterpene and sesquiterpene emission estimates for the United States. *Environmental Science & Technology* 2008, 42, 1623-1629.

44. Saxton, J. E.; Lewis, A. C.; Kettlewell, J. H.; Ozel, M. Z.; Gogus, F.; Boni, Y.; Korogone, S. O. U.; Serca, D., Isoprene and monoterpene measurements in a secondary forest in northern Benin. *Atmospheric Chemistry and Physics* 2007, 7, 4095-4106.

45. Schnitzler, J. P.; Bauknecht, N.; Bruggemann, N.; Einig, W.; Forkel, R.; Hampp, R.; Heiden, A. C.; Heizmann, U.; Hoffmann, T.; Holzke, C.; Jaeger, L.; Klauer, M.; Komenda, M.; Koppmann, R.; Kreuzwieser, J.; Mayer, H.; Rennenberg, H.; Smiatek, G.; Steinbrecher, R.; Wildt, J.; Zimmer, W., Emission of biogenic volatile organic compounds: An overview of field, laboratory and modelling studies performed during the 'Tropospheric Research Program' (TFS) 1997-2000. *Journal of Atmospheric Chemistry* 2002, 42, 159-177.

46. Scott, K. I.; Benjamin, M. T., Development of a biogenic volatile organic compounds emission inventory for the SCOS97-NARSTO domain. *Atmospheric Environment* 2003, 37, S39-S49.

47. Spanke, J.; Rannik, U.; Forkel, R.; Nigge, W.; Hoffmann, T., Emission fluxes and atmospheric degradation of monoterpenes above a boreal forest: field measurements and modelling. *Tellus Series B-Chemical and Physical Meteorology* 2001, 53, 406-422.

48. Aschmann, S. M.; Arey, J.; Atkinson, R., Atmospheric chemistry of three C-10 alkanes. *Journal of Physical Chemistry A* 2001, 105, 7598-7606.

49. Atkinson, R.; Aschmann, S. M.; Carter, W. P. L.; Winer, A. M.; Pitts, J. N., KINETICS OF THE REACTIONS OF OH RADICALS WITH NORMAL-ALKANES AT 299-K+/-2-K. *International Journal of Chemical Kinetics* 1982, 14, 781-788.

50. Atkinson, R.; Aschmann, S. M.; Pitts, J. N., KINETICS OF THE GAS-PHASE REACTIONS OF OH RADICALS WITH A SERIES OF ALPHA,BETA-UNSATURATED CARBONYLS AT 299 +/- 2 K. *International Journal of Chemical Kinetics* 1983, 15, 75-81.

51. Atkinson, R.; Arey, J.; Aschmann, S. M.; Corchnoy, S. B.; Shu, Y. H., RATE CONSTANTS FOR THE GAS-PHASE REACTIONS OF CIS-3-HEXEN-1-OL, CIS-3-HEXENYLACETATE, TRANS-2-HEXENAL, AND LINALOOL WITH OH AND NO3 RADICALS AND O-3 AT 296+/-2 K, AND OH RADICAL FORMATION YIELDS FROM THE O-3 REACTIONS. *International Journal of Chemical Kinetics* 1995, 27, 941-955.

52. Atkinson, R., Gas-phase tropospheric chemistry of volatile organic compounds .1. Alkanes and alkenes. *Journal of Physical and Chemical Reference Data* 1997, 26, 215-290.

53. Atkinson, R.; Arey, J., Gas-phase tropospheric chemistry of biogenic volatile organic compounds: a review. *Atmospheric Environment* 2003, 37, S197-S219.

54. Baxley, J. S.; Wells, J. R., The hydroxyl radical reaction rate constant and atmospheric transformation products of 2-butanol and 2-pentanol. *International Journal of Chemical Kinetics* 1998, 30, 745-752.

55. Kerr, J. A.; Sheppard, D. W., KINETICS OF THE REACTIONS OF HYDROXYL RADICALS WITH ALDEHYDES STUDIED UNDER ATMOSPHERIC CONDITIONS. *Environmental Science & Technology* 1981, 15, 960-963.

56. Li, Z. J.; Singh, S.; Woodward, W.; Dang, L., Kinetics study of OH radical reactions with n-octane, n-nonane, and n-decane at 240-340 K using the relative rate/discharge flow/mass spectrometry technique. *Journal of Physical Chemistry A* 2006, 110, 12150-12157.

57. Papagni, C.; Arey, J.; Atkinson, R., Rate constants for the gas-phase reactions of a series of C-3-C-6 aldehydes with OH and NO3 radicals. *International Journal of Chemical Kinetics* 2000, 32, 79-84.

58. Atkinson, R.; Tuazon, E. C.; Aschmann, S. M., Products of the gas-phase reaction of the OH radical with 3-methyl-1-butene in the presence of NO. *International Journal of Chemical Kinetics* 1998, 30, 577-587.

59. Jenkin, M. E.; Boyd, A. A.; Lesclaux, R., Peroxy radical kinetics resulting from the OH-Initiated oxidation of 1,3-butadiene, 2,3-dimethyl-1,3-butadiene and isoprene. *Journal of Atmospheric Chemistry* 1998, 29, 267-298.

60. Magneron, I.; Thevenet, R.; Mellouki, A.; Le Bras, G.; Moortgat, G. K.; Wirtz, K., A study of the photolysis and OH-initiated oxidation of acrolein and trans-crotonaldehyde. *Journal of Physical Chemistry A* 2002, 106, 2526-2537.

61. Capouet, M.; Mueller, J. F.; Ceulemans, K.; Compernolle, S.; Vereecken, L.; Peeters, J., Modeling aerosol formation in alpha-pinene photo-oxidation experiments. *Journal of Geophysical Research-Atmospheres* 2008, 113.

62. Hamilton, J. F.; Lewis, A. C.; Carey, T. J.; Wenger, J. C.; Garcia, E. B. I.; Munoz, A., Reactive oxidation products promote secondary organic aerosol formation from green leaf volatiles. *Atmospheric Chemistry and Physics* 2009, 9, 3815-3823.

63. Helmig, D.; Greenberg, J.; Guenther, A.; Zimmerman, P.; Geron, C., Volatile organic compounds and isoprene oxidation products at a temperate deciduous forest site. *Journal of Geophysical Research-Atmospheres* 1998, 103, 22397-22414.

64. Presto, A. A.; Hartz, K. E. H.; Donahue, N. M., Secondary organic aerosol production from terpene ozonolysis. 2. Effect of NOx concentration. *Environmental Science & Technology* 2005, 39, 7046-7054.

65. Karl, M.; Tsigaridis, K.; Vignati, E.; Dentener, F., Formation of secondary organic aerosol from isoprene oxidation over Europe. *Atmospheric Chemistry and Physics* 2009, 9, 7003-7030.

66. Atkinson, R., GAS-PHASE TROPOSPHERIC CHEMISTRY OF ORGANIC-COMPOUNDS. *Journal of Physical and Chemical Reference Data* 1994, R1-&.

67. Seinfeld, J. H.; Pandis, S. N., *Atmospheric Chemistry and Physicics: From air pollution to climate change*. John Wiley & Sons, INC: 1997.

68. Koppmann, R., *Volatile Organic Compounds in the Atmosphere*. Blackwell: 2007.

69. Albaladejo, J.; Ballesteros, B.; Jimenez, E.; Martin, P.; Martinez, E., A PLP-LIF kinetic study of the atmospheric reactivity of a series of C-4-C-7 saturated and unsaturated aliphatic aldehydes with OH. *Atmospheric Environment* 2002, 36, 3231-3239.

70. Ananthula, R.; Yamada, T.; Taylor, P. H., Kinetics of OH radical reaction with anthracene and anthracene-d(10). *Journal of Physical Chemistry A* 2006, 110, 3559-3566.

71. Ananthula, R.; Yamada, T.; Taylor, P. H., Kinetics of OH radical reaction with phenanthrene: New absolute rate measurements and comparison with other PAHs. *International Journal of Chemical Kinetics* 2007, 39, 629-637.

72. Aschmann, S. M.; Atkinson, R., Rate constants for the gas-phase reactions of OH radicals with E-7-tetradecene, 2-methyl-1-tridecene and the C-7-C-14 1-alkenes at 295 +/- 1 K. *Physical Chemistry Chemical Physics* 2008, 10, 4159-4164.

73. Atkinson, R.; Aschmann, S. M., OH RADICAL REACTION-RATE CONSTANTS FOR POLYCYCLIC ALKANES - EFFECTS OF RING STRAIN AND CONSEQUENCES FOR ESTIMATION METHODS. *International Journal of Chemical Kinetics* 1992, 24, 983-989.

74. Bejan, I.; Barnes, I.; Olariu, R.; Zhou, S. M.; Wiesen, P.; Benter, T., Investigations on the gas-phase photolysis and OH radical kinetics of methyl-2-nitrophenols. *Physical Chemistry Chemical Physics* 2007, 9, 5686-5692.

75. Bethel, H. L.; Atkinson, R.; Arey, J., Kinetics and products of the reactions of selected diols with the OH radical. *International Journal of Chemical Kinetics* 2001, 33, 310-316.

76. Carrasco, N.; Picquet-Varrault, B.; Doussin, J. F., Kinetic and product study of the gas-phase reaction of sabinaketone with OH radical. *International Journal of Chemical Kinetics* 2007, 39, 415-421.

77. Cavalli, F.; Barnes, I.; Becker, K. H., FT-IR kinetic and product study of the OH radical-initiated oxidation of 1-pentanol. *Environmental Science & Technology* 2000, 34, 4111-4116.

78. Cavalli, F.; Barnes, I.; Becker, K. H., FT-IR kinetic and product study of the OH radical and Cl-atom - Initiated oxidation of dibasic esters. *International Journal of Chemical Kinetics* 2001, 33, 431-439.

79. Colomb, A.; Jacob, V.; Kaluzny, R.; Baussand, R., Kinetic investigation of gas-phase reactions between the OH-radical and o-, m-, p-ethyltoluene and n-nonane in air. *International Journal of Chemical Kinetics* 2004, 36, 367-378.

80. D'Anna, B.; Andresen, W.; Gefen, Z.; Nielsen, C. J., Kinetic study of OH and NO3 radical reactions with 14 aliphatic aldehydes. *Physical Chemistry Chemical Physics* 2001, 3, 3057-3063.

81. Davis, M. E.; Stevens, P. S., Measurements of the kinetics of the OH-initiated oxidation of alpha-pinene: Radical propagation in the OH plus alpha-pinene +O-2+NO reaction system. *Atmospheric Environment* 2005, 39, 1765-1774.

82. Davis, M. E.; Tapscott, C.; Stevens, P. S., Measurements of the kinetics of the OH-initiated oxidation of beta-pinene: Radical propagation in the OH plus beta-pinene plus O-2 plus NO reaction system. *International Journal of Chemical Kinetics* 2005, 37, 522-531.

83. Davis, M. E.; Gilles, M. K.; Ravishankara, A. R.; Burkholder, J. B., Rate coeffcients for the reaction of OH with (E)-2-pentenal, (E)-2-hexenal, and (E)-2-heptenal. *Physical Chemistry Chemical Physics* 2007, 9, 2240-2248.

84. Devi, K. J.; Parveen, S.; Chandra, A. K., Theoretical studies on the kinetics and thermochemistry of the gas-phase addition and H-abstraction reactions of 4-picoline with OH radical. *Chemical Physics Letters* 2009, 480, 161-167.

85. Forester, C. D.; Ham, J. E.; Wells, J. R., Gas-phase chemistry of dihydromyrcenol with ozone and OH radical: Rate constants and products. *International Journal of Chemical Kinetics* 2006, 38, 451-463.

86. Forester, C. D.; Ham, J. E.; Wells, J. R., beta-Ionone reactions with ozone and OH radical: Rate constants and gas-phase products. *Atmospheric Environment* 2007, 41, 8758-8771.

87. Forester, C. D.; Ham, J. E.; Wells, J. R., Geraniol (2,6-dimethyl-2,6-octadien-8-ol) reactions with ozone and OH radical: Rate constants and gas-phase products. *Atmospheric Environment* 2007, 41, 1188-1199.

88. Gao, T. T.; Andino, J. M.; Rivera, C. C.; Marquez, M. F., Rate Constants of the Gas-Phase Reactions of OH Radicals with trans-2-Hexenal, trans-2-Octenal, and trans-2-Nonenal. *International Journal of Chemical Kinetics* 2009, 41, 483-489.

89. Gierczak, T.; Gilles, M. K.; Bauerle, S.; Ravishankara, A. R., Reaction of hydroxyl radical with acetone. 1. Kinetics of the reactions of OH, OD, and (OH)-O-18 with acetone and acetone-d(6). *Journal of Physical Chemistry A* 2003, 107, 5014-5020.

90. Ham, J. E.; Proper, S. P.; Wells, J. R., Gas-phase chemistry of citronellol with ozone and OH radical: Rate constants and products. *Atmospheric Environment* 2006, 40, 726-735.

91. Harrison, J. C.; Wells, J. R., Gas-phase chemistry of benzyl alcohol: Reaction rate constants and products with OH radical and ozone. *Atmospheric Environment* 2009, 43, 798-804.

92. Hurley, M. D.; Ball, J. C.; Wallington, T. J.; Toft, A.; Nielsen, O. J.; Bertman, S.; Perkovic, M., Atmospheric chemistry of a model biodiesel fuel, CH3C(O)O(CH2)(2)OC(O)CH3: Kinetics, mechanisms, and products of Cl atom and OH radical initiated oxidation in the presence and absence of NOx. *Journal of Physical Chemistry A* 2007, 111, 2547-2554.

93. Hurley, M. D.; Wallington, T. J.; Bjarrum, M.; Javadi, M. S.; Nielsen, O. J., Atmospheric chemistry of 3-pentanol: Kinetics, mechanisms, and products of Cl atom and OH radical initiated oxidation in the presence and absence of NOX. *Journal of Physical Chemistry A* 2008, 112, 8053-8060.

94. Hurley, M. D.; Wallington, T. J.; Lauirsen, L.; Javadi, M. S.; Nielsen, O. J.; Yamanaka, T.; Kawasaki, M., Atmospheric Chemistry of n-Butanol: Kinetics, Mechanisms, and Products of Cl Atom and OH Radical Initiated Oxidation in the Presence and Absence of NOx. *Journal of Physical Chemistry A* 2009, 113, 7011-7020.

95. Klotz, B.; Barnes, I.; Becker, K. H., Kinetic study of the gas-phase photolysis and OH radical reaction of E,Z- and E,E-2,4-hexadienedial. *International Journal of Chemical Kinetics* 1999, 31, 689-697.

96. Kwok, E. S. C.; Atkinson, R., ESTIMATION OF HYDROXYL RADICAL REACTION-RATE CONSTANTS FOR GAS-PHASE ORGANIC-COMPOUNDS USING A STRUCTURE-REACTIVITY RELATIONSHIP - AN UPDATE. *Atmospheric Environment* 1995, 29, 1685-1695.

97. Kwok, E. S. C.; Atkinson, R.; Arey, J., RATE CONSTANTS FOR THE GAS-PHASE REACTIONS OF THE OH RADICAL WITH DICHLOROBIPHENYLS, 1-CHLORODIBENZO-P-DIOXIN, 1,2-DIMETHOXYBENZENE, AND DIPHENYL ETHER - ESTIMATION OF OH RADICAL REACTION-RATE CONSTANTS FOR PCBS, PCDDS, AND PCDFS. *Environmental Science & Technology* 1995, 29, 1591-1598.

98. Kwok, E. S. C.; Aschmann, S. M.; Atkinson, R., Rate constants for the gas-phase reactions of the OH radical with selected carbamates and lactates. *Environmental Science & Technology* 1996, 30, 329-334.

99. Loison, J. C.; Ley, L.; Lesclaux, R., Kinetic study of OH radical reactions with chlorobutane isomers at 298 K. *Chemical Physics Letters* 1998, 296, 350-356.

100. Mason, S. A.; Arey, J.; Atkinson, R., Kinetics and Products of the OH Radical-Initiated Reaction of 1,4-Butanediol and Rate Constants for the Reactions of OH Radicals with 4-Hydroxybutanal and 3-Hydroxypropanal. *Environmental Science & Technology* 2010, 44, 707-713.

101. Maurer, T.; Geiger, H.; Barnes, I.; Becker, K. H.; Thuner, L. P., Kinetic, mechanistic, and modeling study of the OH-radical-initiated oxidation of di-n-butoxymethane (DNBM). *Journal of Physical Chemistry A* 2000, 104, 11087-11094.

102. Mellouki, A.; Teton, S.; Lebras, G., KINETICS OF OH RADICAL REACTIONS WITH A SERIES OF ETHERS. *International Journal of Chemical Kinetics* 1995, 27, 791-805.

103. Mellouki, A.; Oussar, F.; Lun, X.; Chakir, A., Kinetics of the reactions of the OH radical with 2-methyl-1-propanol, 3-methyl-1-butanol and 3-methyl-2-butanol between 241 and 373 K. *Physical Chemistry Chemical Physics* 2004, 6, 2951-2955.

104. Phousongphouang, P. T.; Arey, J., Rate constants for the gas-phase reactions of a series of alkylnaphthalenes with the OH radical. *Environmental Science & Technology* 2002, 36, 1947-1952.

105. Pimentel, A. S.; Arbilla, G., Kinetic analysis of the gas-phase reactions of methyl tert-butyl ether with the OH radical in the presence of NOx. *Journal of the Brazilian Chemical Society* 1998, 9, 539-550.

106. Pimentel, A. S.; Arbilla, G., Kinetic analysis of the gas-phase reactions of methyl vinyl ketone with the OH radical in the presence of NOx. *Journal of the Brazilian Chemical Society* 1998, 9, 551-562.

107. Pimentel, A. S.; Arbilla, G., Kinetic analysis of the gas-phase reactions of methacrolein with the OH radical in the presence of NOx. *Journal of the Brazilian Chemical Society* 1999, 10, 483-491.

108. Sauer, C. G.; Barnes, I.; Becker, K. H.; Geiger, H.; Wallington, T. J.; Christensen, L. K.; Platz, J.; Nielsen, O. J., Atmospheric chemistry of 1,3-dioxolane: Kinetic, mechanistic, and modeling study of OH radical initiated oxidation. *Journal of Physical Chemistry A* 1999, 103, 5959-5966.

109. Upadhyaya, H. P.; Kumar, A.; Naik, P. D.; Sapre, A. V.; Mittal, J. P., Kinetics of OH radical reaction with allyl alcohol (H2C=CHCH2OH) and propargyl alcohol (HC CCH2OH) studied by LIF. *Chemical Physics Letters* 2001, 349, 279-285.

110. Wells, J. R., Gas-phase chemistry of alpha-terpineol with ozone and OH radical: Rate constants and products. *Environmental Science & Technology* 2005, 39, 6937-6943.

111. Arey, J.; Kwok, E. S. C.; Bridier, I.; Aschmann, S. M., PRODUCTS OF THE GAS-PHASE OH AND NO3 RADICAL-INITIATED REACTIONS OF NAPHTHALENE. *Abstracts of Papers of the American Chemical Society* 1995, 209, 90-ENVR.

112. Arey, J.; Obermeyer, G.; Aschmann, S. M.; Chattopadhyay, S.; Cusick, R. D.; Atkinson, R., Dicarbonyl Products of the OH Radical-Initiated Reaction of a Series of Aromatic Hydrocarbons. *Environmental Science & Technology* 2009, 43, 683-689.

113. Aschmann, S. M.; Chew, A. A.; Arey, J.; Atkinson, R., Products of the gas-phase reaction of OH radicals with cyclohexane: Reactions of the cyclohexoxy radical. *Journal of Physical Chemistry A* 1997, 101, 8042-8048.

114. Aschmann, S. M.; Reissell, A.; Atkinson, R.; Arey, J., Products of the gas phase reactions of the OH radical with alpha- and beta-pinene in the presence of NO. *Journal of Geophysical Research-Atmospheres* 1998, 103, 25553-25561.

115. Aschmann, S. M.; Atkinson, R., Products of the gas-phase reactions of the OH radical with n-butyl methyl ether and 2-isopropoxyethanol: Reactions of ROC(O)< radicals. *International Journal of Chemical Kinetics* 1999, 31, 501-513.

116. Atkinson, R.; Arey, J.; Tuazon, E. C.; Aschmann, S. M.; Hakola, H., PRODUCTS OF THE OH RADICAL AND O3 REACTIONS WITH ISOPRENE AND MONOTERPENES. *Abstracts of Papers of the American Chemical Society* 1994, 207, 160-ENVR.

117. Atkinson, R.; Aschmann, S. M., ALKOXY RADICAL ISOMERIZATION PRODUCTS FROM THE GAS-PHASE OH RADICAL-

INITIATED REACTIONS OF 2,4-DIMETHYL-2-PENTANOL AND 3,5-DIMETHYL-3-HEXANOL. *Environmental Science & Technology* 1995, 29, 528-536.

118. Atkinson, R.; Aschmann, S. M., PRODUCTS OF THE GAS-PHASE OH RADICAL-INITIATED REACTIONS OF 4-METHYL-2-PENTANONE AND 2,6-DIMETHYL-4-HEPTANONE. *International Journal of Chemical Kinetics* 1995, 27, 261-275.

119. Atkinson, R.; Tuazon, E. C.; Aschmann, S. M., PRODUCTS OF THE GAS-PHASE REACTIONS OF A SERIES OF 1-ALKENES AND 1-METHYLCYCLOHEXENE WITH THE OH RADICAL IN THE PRESENCE OF NO. *Environmental Science & Technology* 1995, 29, 1674-1680.

120. Benkelberg, H. J.; Boge, O.; Seuwen, R.; Warneck, P., Product distributions from the OH radical-induced oxidation of but-1-ene, methyl-substituted but-1-enes and isoprene in NOx-free air. *Physical Chemistry Chemical Physics* 2000, 2, 4029-4039.

121. Bethel, H. L.; Atkinson, R.; Arey, J., Products of the OH radical-initiated reactions of p-xylene and 1,2,3-and 1,2,4-trimethylbenzene. *Abstracts of Papers of the American Chemical Society* 2000, 220, 185-ENVR.

122. Bethel, H. L.; Arey, J.; Atkinson, R., Products of the OH radical-initiated reaction of 3-hexene-2,5-dione. *Environmental Science & Technology* 2001, 35, 4477-4480.

123. Butt, C. M.; Young, C. J.; Mabury, S. A.; Hurley, M. D.; Wallington, T. J., Atmospheric Chemistry of 4:2 Fluorotelomer Acrylate C4F9CH2CH2OC(O)CH=CH2 : Kinetics, Mechanisms, and Products of Chlorine-Atom- and OH-Radical-Initiated Oxidation. *Journal of Physical Chemistry A* 2009, 113, 3155-3161.

124. Carrasco, N.; Rayez, M. T.; Rayez, J. C.; Doussin, J. F., Experimental and theoretical study of the reaction of OH radical with sabinene. *Physical Chemistry Chemical Physics* 2006, 8, 3211-3217.

125. Cartas-Rosado, R.; Castro, M., Theoretical study of reaction mechanisms of OH radical with toluene 1,2-epoxide/2-methyloxepin. *Journal of Physical Chemistry A* 2007, 111, 13088-13098.

126. D'Anna, B.; Bakken, V.; Beukes, J. A.; Nielsen, C. J.; Brudnik, K.; Jodkowski, J. T., Experimental and theoretical studies of gas phase NO3 and OH radical reactions with formaldehyde, acetaldehyde and their isotopomers. *Physical Chemistry Chemical Physics* 2003, 5, 1790-1805.

127. Forester, C. D.; Wells, J. R., Yields of Carbonyl Products from Gas-Phase Reactions of Fragrance Compounds with OH Radical and Ozone. *Environmental Science & Technology* 2009, 43, 3561-3568.

128. Heimann, G.; Warneck, P., OH RADICAL INDUCED OXIDATION OF 2,3-DIMETHYLBUTANE IN AIR. *Journal of Physical Chemistry* 1992, 96, 8403-8409.

129. Heimann, G.; Warneck, P., Product distributions from the OH radical-induced oxidation of n-pentane and isopentane (2-methylbutane) in air. *International Journal of Chemical Kinetics* 2006, 38, 677-688.

130. Helmig, D.; Harger, W. P., OH RADICAL-INITIATED GAS-PHASE REACTION-PRODUCTS OF PHENANTHRENE. *Science of the Total Environment* 1994, 148, 11-21.

131. Kwok, E. S. C.; Aschmann, S. M.; Atkinson, R.; Arey, J., Products of the gas-phase reactions of o-, m- and p-xylene with the OH radical in the presence and absence of NOx. *Journal of the Chemical Society-Faraday Transactions* 1997, 93, 2847-2854.

132. Kwok, E. S. C.; Aschmann, S. M.; Atkinson, R.; Arey, J., Products of the reactions of xylenes with the OH radical. *Abstracts of Papers of the American Chemical Society* 1997, 214, 25-COLL.

133. Lane, D. A.; Bunce, N. J.; Liu, L.; Zhu, J., Products of the reaction of naphthalene with the OH radical in air. *Abstracts of Papers of the American Chemical Society* 1997, 213, 218-ENVR.

134. Lim, Y. B.; Ziemann, P. J., Chemistry of Secondary Organic Aerosol Formation from OH Radical-Initiated Reactions of Linear, Branched, and Cyclic Alkanes in the Presence of NOx. *Aerosol Science and Technology* 2009, 43, 604-619.

135. Lim, Y. B.; Ziemann, P. J., Effects of Molecular Structure on Aerosol Yields from OH Radical-Initiated Reactions of Linear, Branched, and Cyclic Alkanes in the Presence of NOx. *Environmental Science & Technology* 2009, 43, 2328-2334.

136. Loison, J. C.; Daranlot, J.; Bergeat, A.; Caralp, F.; Mereau, R.; Hickson, K. M., Gas-Phase Kinetics of Hydroxyl Radical Reactions with C3H6 and C4H8: Product Branching Ratios and OH Addition Site-Specificity. *Journal of Physical Chemistry A* 2010, 114, 13326-13336.

137. Martin, J. W.; Ellis, D. A.; Mabury, S. A.; Hurley, M. D.; Wallington, T. J., Atmospheric chemistry of perfluoroalkanesulfonamides: Kinetic and product studies of the OH radical and Cl atom initiated oxidation of N-ethyl

perfluorobutanesulfonamide. *Environmental Science & Technology* 2006, 40, 864-872.

138. Moriarty, J.; Wenger, J. C.; Sidebottom, H. W., Product Study of the OH Radical and Cl Atom Initiated Oxidation of 1,3-Dioxane. *Chemphyschem* 2010, 11, 3980-3986.

139. Nishino, N.; Atkinson, R.; Arey, J., Formation of Nitro Products from the Gas-Phase OH Radical-Initiated Reactions of Toluene, Naphthalene, and Biphenyl: Effect of NO2 Concentration. *Environmental Science & Technology* 2008, 42, 9203-9209.

140. Wang, S. B.; Ang, H. M.; Tade, M. O., Volatile organic compounds in indoor environment and photocatalytic oxidation: State of the art. *Environment International* 2007, 33, 694-705.

141. Brown, S. K.; Sim, M. R.; Abramson, M. J.; Gray, C. N., CONCENTRATIONS OF VOLATILE ORGANIC-COMPOUNDS IN INDOOR AIR - A REVIEW. *Indoor Air-International Journal of Indoor Air Quality and Climate* 1994, 4, 123-134.

142. Namiesnik, J.; Gorecki, T.; Kozdronzabiegala, B.; Lukasiak, J., INDOOR AIR-QUALITY (IAQ), POLLUTANTS, THEIR SOURCES AND CONCENTRATION LEVELS. *Building and Environment* 1992, 27, 339-356.

143. Schleibinger, H.; Laussmann, D.; Brattig, C.; Mangler, M.; Eis, D.; Ruden, H., Emission patterns and emission rates of MVOC and the possibility for predicting hidden mold damage? *Indoor Air* 2005, 15, 98-104.

144. Araki, A.; Kawai, T.; Eitaki, Y.; Kanazawa, A.; Morimoto, K.; Nakayama, K.; Shibata, E.; Tanaka, M.; Takigawa, T.; Yoshimura, T.; Chikara, H.; Saijo, Y.; Kishi, R., Prevalence of Asthma, Atopic Dermatitis, and Rhinitis and MVOC Exposure in Single Family Homes-A Survey in 6 Cities of Japan. *Epidemiology* 2011, 22, S40-S41.

145. Bjurman, J.; Nordstrand, E.; Kristensson, J., Growth-phase-related production of potential volatile-organic tracer compounds by moulds on wood. *Indoor Air-International Journal of Indoor Air Quality and Climate* 1997, 7, 2-7.

146. Fischer, G.; Schwalbe, R.; Moller, M.; Ostrowski, R.; Dott, M., Species-specific production of microbial volatile organic compounds (MVOC) by airborne fungi from a compost facility. *Chemosphere* 1999, 39, 795-810.

147. Fischer, G.; Muller, T.; Schwalbe, R.; Ostrowski, R.; Dott, W., Exposure to airborne fungi, MVOC and mycotoxins in biowaste-handling facilities. *International Journal of Hygiene and Environmental Health* 2000, 203, 97-104.

148. Fischer, G.; Albrecht, A.; Jackel, U.; Kampfer, P., Analysis of airborne microorganisms, MVOC and odour in the surrounding of composting facilities and implications for future investigations. *International Journal of Hygiene and Environmental Health* 2008, 211, 132-142.

149. Herr, C.; Schenke, S.; Harpel, S.; Fischer, G.; Rethage, T.; Ulu, F.; Bergmarm, A.; Stilianakis, N.; Lindemann, H.; Eikmann, T., Exposure assessment of microbial volatile organic compounds (MVOC) and organic contaminants in normal bedrooms of children with airway disease. *Epidemiology* 2004, 15, S68-S68.

150. Keller, R.; Senkpiel, K.; Butte, W., Moulds and their secondary metabolites (MVOC) in air samples of uncontaminated dwellings. *Gefahrstoffe Reinhaltung Der Luft* 2007, 67, 77-84.

151. Norback, D.; Wieslander, G.; Strom, G.; Edling, C., EXPOSURE TO VOLATILE ORGANIC-COMPOUNDS OF MICROBIAL ORIGIN (MVOC) DURING INDOOR APPLICATION OF WATER-BASED PAINTS. *Indoor Air-International Journal of Indoor Air Quality and Climate* 1995, 5, 166-170.

152. Parkinson, D. R.; Churchill, T. J.; Wady, L.; Pawliszyn, J., Investigation of Mold Growth in Indoor School Buildings by Monitoring Outgassed Methyl Benzoate as a MVOC Biomarker. *Indoor and Built Environment* 2009, 18, 257-264.

153. Pasanen, A. L.; Korpi, A.; Kasanen, J. P.; Pasanen, P., Critical aspects on the significance of microbial volatile metabolites as indoor air pollutants. *Environment International* 1998, 24, 703-712.

154. Persoons, R.; Stoklov, M.; Parat, S.; Maitre, A., Professional exposure to microorganisms and microbial volatile organic compounds (MVOC) in a composting facility. *Epidemiology* 2006, 17, S463-S463.

155. Persoons, R.; Parat, S.; Stoklov, M.; Perdrix, A.; Maitre, A., Critical working tasks and determinants of exposure to bioaerosols and MVOC at composting facilities. *International Journal of Hygiene and Environmental Health* 2010, 213, 338-347.

156. Schleibinger, H. W.; Wurm, D.; Moritz, M.; Bock, R.; Ruden, H., The sick building syndrome and HVAC systems: MVOC from air filters. *Zentralblatt Fur Hygiene Und Umweltmedizin* 1997, 200, 137-151.

157. Schuchardt, S.; Kruse, H., Quantitative volatile metabolite profiling of common indoor fungi: relevancy for indoor air analysis. *Journal of Basic Microbiology* 2009, 49, 350-362.

158. Walinder, R.; Ernstgard, L.; Norback, D.; Wieslander, G.; Johanson, G., Acute effects of 1-octen-3-ol, a microbial volatile organic compound (MVOC)-An experimental study. *Toxicology Letters* 2008, 181, 141-147.

159. Wilkins, K.; Larsen, K.; Simkus, M., Volatile metabolites from mold growth on building materials and synthetic media. *Chemosphere* 2000, 41, 437-446.

160. Wilkins, C. K.; Scholl, S., VOLATILE METABOLITES OF SOME BARLEY STORAGE MOLDS. *International Journal of Food Microbiology* 1989, 8, 11-17.

161. Bjurman, J.; Kristensson, J., PRODUCTION OF VOLATILE METABOLITES BY THE SOFT ROT FUNGUS CHAETOMIUM-GLOBOSUM ON BUILDING-MATERIALS AND DEFINED MEDIA. *Microbios* 1992, 72, 47-54.

162. Bjurman, J.; Kristensson, J., VOLATILE PRODUCTION BY ASPERGILLUS-VERSICOLOR AS A POSSIBLE CAUSE OF ODOR IN HOUSES AFFECTED BY FUNGI. *Mycopathologia* 1992, 118, 173-178.

163. Wilkins, K.; Nielsen, E. M.; Wolkoff, P., Patterns in volatile organic compounds in dust from moldy buildings. *Indoor Air* 1997, 7, 128-134.

164. Korpi, A.; Pasanen, A. L.; Pasanen, P., Volatile compounds originating from mixed microbial cultures on building materials under various humidity conditions. *Applied and Environmental Microbiology* 1998, 64, 2914-2919.

165. Claeson, A. S.; Levin, J. O.; Blomquist, G.; Sunesson, A. L., Volatile metabolites from microorganisms grown on humid building materials and synthetic media. *Journal of Environmental Monitoring* 2002, 4, 667-672.

166. Reddy, C. V. G.; Cao, W.; Tan, O. K.; Zhu, W., Preparation of Fe2O3(0.9)-SnO2(0.1) by hydrazine method: application as an alcohol sensor. *Sensors and Actuators B-Chemical* 2002, 81, 170-175.

167. Neaves, P. I.; Hatfield, J. V. In *A NEW-GENERATION OF INTEGRATED ELECTRONIC NOSES*, 1995; pp 223-231.

168. Reddy, C. V. G.; Seela, K. K.; Manorama, S. V., Preparation of gamma-Fe2O3 by the hydrazine method - Application as an alcohol sensor. *International Journal of Inorganic Materials* 2000, 2, 301-307.

169. Tan, O. K.; Cao, W.; Zhu, W., Alcohol sensor based on a non-equilibrium nanostructured xZrO(2)-(1-x)alpha-Fe2O3 solid solution system. *Sensors and Actuators B-Chemical* 2000, 63, 129-134.

170. Pokhrel, S.; Huo, L. H.; Zhao, H.; Gao, S., Triangular network of crystalline submicron rutile TiO2 block assembly: An alcohol sensor. *Sensors and Actuators B-Chemical* 2008, 129, 18-23.

171. Garzella, C.; Comini, E.; Tempesti, E.; Frigeri, C.; Sberveglieri, G. In *TiO2 thin films by a novel sol-gel processing for gas sensor applications*, 2000; pp 189-196.

172. Taurino, A. M.; Capone, S.; Siciliano, P.; Toccoli, T.; Boschetti, A.; Guerini, L.; Iannotta, S., Nanostructured TiO2 thin films prepared by supersonic beams and their application in a sensor array for the discrimination of VOC. *Sensors and Actuators B-Chemical* 2003, 92, 292-302.

173. Huo, L. H.; Li, Q.; Zhao, H.; Yu, L. J.; Gao, S.; Zhao, J. G., Sol-gel route to pseudocubic shaped alpha-Fe2O3 alcohol sensor: preparation and characterization. *Sensors and Actuators B-Chemical* 2005, 107, 915-920.

174. Xu, C.; Tamaki, J.; Miura, N.; Yamazoe, N., GRAIN-SIZE EFFECTS ON GAS SENSITIVITY OF POROUS SNO2-BASED ELEMENTS. *Sensors and Actuators B-Chemical* 1991, 3, 147-155.

175. Gopel, W.; Schierbaum, K. D. In *SNO2 SENSORS - CURRENT STATUS AND FUTURE-PROSPECTS*, 1995; pp 1-12.

176. Fang, Y. K.; Lee, J. J., A TIN OXIDE THIN-FILM SENSOR WITH HIGH ETHANOL SENSITIVITY. *Thin Solid Films* 1989, 169, 51-56.

177. Tsang, S. C.; Bulpitt, C., Rare earth oxide sensors for ethanol analysis. *Sensors and Actuators B-Chemical* 1998, 52, 226-235.

178. Tan, O. K.; Zhu, W.; Yan, Q.; Kong, L. B. In *Size effect and gas sensing characteristics of nanocrystalline xSnO(2)-(1-x)alpha-Fe2O3 ethanol sensors*, 2000; pp 361-365.

179. Rao, B. B., Zinc oxide ceramic semi-conductor gas sensor for ethanol vapour. *Materials Chemistry and Physics* 2000, 64, 62-65.

180. Kim, S. J.; Jeon, B. H.; Choi, K. S.; Min, N. K. In *Capacitive porous silicon sensors for measurement of low alcohol gas concentration at room temperature*, 2000; pp 363-366.

181. Albert, K. J.; Lewis, N. S.; Schauer, C. L.; Sotzing, G. A.; Stitzel, S. E.; Vaid, T. P.; Walt, D. R., Cross-reactive chemical sensor arrays. *Chemical Reviews* 2000, 100, 2595-2626.

182. Shi, J. J.; Li, J. J.; Zhu, Y. F.; Wei, F.; Zhang, X. R., Nanosized SrCO3-based chemiluminescence sensor for ethanol. *Analytica Chimica Acta* 2002, 466, 69-78.

183. Zhu, Y. F.; Shi, J. J.; Zhang, Z. Y.; Zhang, C.; Zhang, X. R., Development of a gas sensor utilizing chemiluminescence on nanosized titanium dioxide. *Analytical Chemistry* 2002, 74, 120-124.

184. Zhang, Z. Y.; Zhang, C.; Zhang, X. R., Development of a chemiluminescence ethanol sensor based on nanosized ZrO2. *Analyst* 2002, 127, 792-796.

185. Yu, C.; Liu, G. H.; Zuo, B. L.; Tang, Y. J.; Zhang, T., A novel gaseous pinacolyl alcohol sensor utilizing cataluminescence on alumina nanowires prepared by supercritical fluid drying. *Analytica Chimica Acta* 2008, 618, 204-209.

186. Sasahara, T.; Kido, A.; Sunayama, T.; Uematsu, S.; Egashira, M., Identification and quantification of alcohol by a micro gas sensor based on adsorption and combustion. *Sensors and Actuators B-Chemical* 2004, 99, 532-538.

187. Lee, D. S.; Kim, Y. T.; Huh, J. S.; Lee, D. D., Fabrication and characteristics of SnO2 gas sensor array for volatile organic compounds recognition. *Thin Solid Films* 2002, 416, 271-278.

188. Penza, M.; Cassano, G.; Tortorella, F., Gas recognition by activated WO3 thin-film sensors array. *Sensors and Actuators B-Chemical* 2001, 81, 115-121.

189. Maekawa, T.; Suzuki, K.; Takada, T.; Kobayashi, T.; Egashira, M., Odor identification using a SnO2-based sensor array. *Sensors and Actuators B-Chemical* 2001, 80, 51-58.

190. Burl, M. C.; Sisk, B. C.; Vaid, T. P.; Lewis, N. S., Classification performance of carbon black-polymer composite vapor detector arrays as a function of array size and detector composition. *Sensors and Actuators B-Chemical* 2002, 87, 130-149.

191. Barisci, J. N.; Wallace, G. G.; Andrews, M. K.; Partridge, A. C.; Harris, P. D., Conducting polymer sensors for monitoring aromatic hydrocarbons using an electronic nose. *Sensors and Actuators B-Chemical* 2002, 84, 252-257.

192. Bender, F.; Barie, N.; Romoudis, G.; Voigt, A.; Rapp, A., Development of a preconcentration unit for a SAW sensor micro array and its use for indoor air quality monitoring. *Sensors and Actuators B-Chemical* 2003, 93, 135-141.

193. Anisimkin, V. I.; Verona, E.; Zemlyakov, V. E.; Kryshtal, R. G.; Medved, A. V., Integrated sensor array for analysis of multicomponent gas mixtures. *Technical Physics Letters* 1998, 24, 640-642.

194. Nanto, H.; Kawai, T.; Sokooshi, H.; Usuda, T., AROMA IDENTIFICATION USING A QUARTZ-RESONATOR SENSOR IN CONJUNCTION WITH PATTERN-RECOGNITION. *Sensors and Actuators B-Chemical* 1993, 14, 718-720.

195. Kasai, N.; Sugimoto, I.; Nakamura, M., Discrimination of odorants of definite concentrations by using plasma-organic-film-coated QCR sensors. *Sensors and Actuators B-Chemical* 2000, 65, 114-119.

196. Srivastava, A. K., Detection of volatile organic compounds (VOCs) using SnO2 gas-sensor array and artificial neural network. *Sensors and Actuators B-Chemical* 2003, 96, 24-37.

197. Kida, T.; Minami, T.; Yuasa, M.; Shimanoe, K.; Yamazoe, N., Organic gas sensor using BiCuVOx solid electrolyte. *Electrochemistry Communications* 2008, 10, 311-314.

198. Bearzotti, A.; Macagnano, A.; Pantalei, S.; Zampetti, E.; Venditti, I.; Fratoddi, I.; Russo, M. V. In *Alcohol vapor sensory properties of nanostructured conjugated polymers*, 2008.

199. Jahnke, S. A.; Niemann, J.; Kautek, W.; Bischoff, R.; Pfeiffer, C.; Kossmehl, G. In *Sensor system for alcohol and chlorinated hydrocarbon vapours on the basis of semiconducting polymers*, 1997; pp 223-236.

200. Morisawa, M.; Amemiya, Y.; Kohzu, H.; Liang, C. X.; Muto, S. In *Plastic optical fibre sensor for detecting vapour phase alcohol*, 2001; pp 877-881.

201. Spadavecchia, J.; Ciccarella, G.; Siciliano, P.; Capone, S.; Rella, R., Spin-coated thin films of metal porphyrin-phthalocyanine blend for an optochemical sensor of alcohol vapours. *Sensors and Actuators B-Chemical* 2004, 100, 88-93.

202. Williams, A. K.; Hupp, J. T., Sol-gel-encapsulated alcohol dehydrogenase as a versatile, environmentally stabilized sensor for alcohols and aldehydes. *Journal of the American Chemical Society* 1998, 120, 4366-4371.

203. Mills, C. A.; Beeley, J.; Wyse, C.; Cumming, D. R. S.; Glidle, A.; Cooper, J. M., Polymer-based micro-sensor paired arrays for the determination of primary alcohol vapors. *Sensors and Actuators B-Chemical* 2007, 125, 85-91.

204. Hamilton, S.; Hepher, M.; Sommerville, J., Polypyrrole materials for detection and discrimination of volatile organic compounds. *Sensors and Actuators B-Chemical* 2005, 107, 424-432.

205. Jensenius, H.; Thaysen, J.; Rasmussen, A. A.; Veje, L. H.; Hansen, O.; Boisen, A., A microcantilever-based alcohol vapor sensor-application and response model. *Applied Physics Letters* 2000, 76, 2615-2617.

206. Roy, S. C.; Varghese, O. K.; Paulose, M.; Grimes, C. A., Toward Solar Fuels: Photocatalytic Conversion of Carbon Dioxide to Hydrocarbons. *Acs Nano* 2010, 4, 1259-1278.

207. Osterloh, F. E., Inorganic materials as catalysts for photochemical splitting of water. *Chemistry of Materials* 2008, 20, 35-54.

208. Abu-Khader, M. M., Recent progress in CO2 capture/sequestration: A review. *Energy Sources Part a-Recovery Utilization and Environmental Effects* 2006, 28, 1261-1279.

209. Ni, M.; Leung, M. K. H.; Leung, D. Y. C.; Sumathy, K., A review and recent developments in photocatalytic water-splitting using TiO2 for hydrogen production. *Renewable & Sustainable Energy Reviews* 2007, 11, 401-425.

210. Hashimoto, K.; Irie, H.; Fujishima, A., TiO(2) photocatalysis: A historical overview and future prospects. *Japanese Journal of Applied Physics Part 1-Regular Papers Brief Communications & Review Papers* 2005, 44, 8269-8285.

211. Bickley, R. I.; Gonzalezcarreno, T.; Lees, J. S.; Palmisano, L.; Tilley, R. J. D., A STRUCTURAL INVESTIGATION OF TITANIUM-DIOXIDE PHOTOCATALYSTS. *Journal of Solid State Chemistry* 1991, 92, 178-190.

212. Hurum, D. C.; Agrios, A. G.; Gray, K. A.; Rajh, T.; Thurnauer, M. C., Explaining the enhanced photocatalytic activity of Degussa P25 mixed-phase TiO2 using EPR. *Journal of Physical Chemistry B* 2003, 107, 4545-4549.

213. Tanaka, K.; Capule, M. F. V.; Hisanaga, T., EFFECT OF CRYSTALLINITY OF TIO2 ON ITS PHOTOCATALYTIC ACTION. *Chemical Physics Letters* 1991, 187, 73-76.

214. Ohno, T.; Sarukawa, K.; Tokieda, K.; Matsumura, M., Morphology of a TiO2 photocatalyst (Degussa, P-25) consisting of anatase and rutile crystalline phases. *Journal of Catalysis* 2001, 203, 82-86.

215. Kawahara, T.; Konishi, Y.; Tada, H.; Tohge, N.; Nishii, J.; Ito, S., A patterned TiO2(anatase)/TiO2(rutile) bilayer-type photocatalyst: Effect of the anatase/rutile junction on the photocatalytic activity. *Angewandte Chemie-International Edition* 2002, 41, 2811-+.

216. Li, G. H.; Ciston, S.; Saponjic, Z. V.; Chen, L.; Dimitrijevic, N. M.; Rajh, T.; Gray, K. A., Synthesizing mixed-phase TiO2 nanocomposites using a

hydrothermal method for photo-oxidation and photoreduction applications. *Journal of Catalysis* 2008, 253, 105-110.

217. Nakajima, H.; Mori, T.; Shen, Q.; Toyoda, T., Photoluminescence study of mixtures of anatase and rutile TiO2 nanoparticles: Influence of charge transfer between the nanoparticles on their photo luminescence excitation bands. *Chemical Physics Letters* 2005, 409, 81-84.

218. Yan, M. C.; Chen, F.; Zhang, J. L.; Anpo, M., Preparation of controllable crystalline titania and study on the photocatalytic properties. *Journal of Physical Chemistry B* 2005, 109, 8673-8678.

219. Leytner, S.; Hupp, J. T., Evaluation of the energetics of electron trap states at the nanocrystalline titanium dioxide/aqueous solution interface via time-resolved photoacoustic spectroscopy. *Chemical Physics Letters* 2000, 330, 231-236.

220. Emeline, A. V.; Smirnova, L. G.; Kuzmin, G. N.; Basov, L. L.; Serpone, N., Spectral dependence of quantum yields in gas-solid heterogeneous photosystems - Influence of anatase/rutile content on the photostimulated adsorption of dioxygen and dihydrogen on titania. *Journal of Photochemistry and Photobiology a-Chemistry* 2002, 148, 97-102.

221. Ohno, T.; Tokieda, K.; Higashida, S.; Matsumura, M., Synergism between rutile and anatase TiO2 particles in photocatalytic oxidation of naphthalene. *Applied Catalysis a-General* 2003, 244, 383-391.

222. Tan, S. S.; Zou, L.; Hu, E., Photocatalytic reduction of carbon dioxide into gaseous hydrocarbon using TiO2 pellets. *Catalysis Today* 2006, 115, 269-273.

223. Lo, C. C.; Hung, C. H.; Yuan, C. S.; Wu, J. F., Photoreduction of carbon dioxide with H-2 and H2O over TiO2 and ZrO2 in a circulated photocatalytic reactor. *Solar Energy Materials and Solar Cells* 2007, 91, 1765-1774.

224. Linsebigler, A. L.; Lu, G. Q.; Yates, J. T., PHOTOCATALYSIS ON TIO2 SURFACES - PRINCIPLES, MECHANISMS, AND SELECTED RESULTS. *Chemical Reviews* 1995, 95, 735-758.

225. Varghese, O. K.; Paulose, M.; LaTempa, T. J.; Grimes, C. A., High-Rate Solar Photocatalytic Conversion of CO(2) and Water Vapor to Hydrocarbon Fuels (vol 9, pg 731, 2009). *Nano Letters* 2010, 10, 750-750.

226. Tseng, I. H.; Chang, W. C.; Wu, J. C. S., Photoreduction of CO2 using sol-gel derived titania and titania-supported copper catalysts. *Applied Catalysis B-Environmental* 2002, 37, 37-48.

227. Zhang, Q. Y.; Gao, T. T.; Andino, J. M.; Li, Y., Copper and iodine co-modified $TiO_2$ nanoparticles for improved activity of $CO_2$ photoreduction with water vapor. *Applied Catalysis B: Environmental* 2012, 123-124, 257-264.

228. Li, Y.; Wang, W. N.; Zhan, Z. L.; Woo, M. H.; Wu, C. Y.; Biswas, P., Photocatalytic reduction of CO(2) with H(2)O on mesoporous silica supported Cu/TiO(2) catalysts. *Applied Catalysis B-Environmental* 2010, 100, 386-392.

229. Chuang, H. Y.; Chen, D. H., Fabrication and photocatalytic activities in visible and UV light regions of Ag@TiO2 and NiAg@TiO2 nanoparticles. *Nanotechnology* 2009, 20.

230. Leary, R.; Westwood, A., Carbonaceous nanomaterials for the enhancement of TiO(2) photocatalysis. *Carbon* 2011, 49, 741-772.

231. Yao, Y.; Li, G.; Ciston, S.; Lueptow, R. M.; Gray, K. A., Photoreactive TiO2/carbon nanotube composites: Synthesis and reactivity. *Environmental Science & Technology* 2008, 42, 4952-4957.

232. Zhang, H.; Lv, X. J.; Li, Y. M.; Wang, Y.; Li, J. H., P25-Graphene Composite as a High Performance Photocatalyst. *Acs Nano* 2010, 4, 380-386.

233. Woan, K.; Pyrgiotakis, G.; Sigmund, W., Photocatalytic Carbon-Nanotube-TiO(2) Composites. *Advanced Materials* 2009, 21, 2233-2239.

234. Ng, Y. H.; Lightcap, I. V.; Goodwin, K.; Matsumura, M.; Kamat, P. V., To What Extent Do Graphene Scaffolds Improve the Photovoltaic and Photocatalytic Response of TiO2 Nanostructured Films? *Journal of Physical Chemistry Letters* 2010, 1, 2222-2227.

235. Ishigami, M.; Chen, J. H.; Cullen, W. G.; Fuhrer, M. S.; Williams, E. D., Atomic structure of graphene on SiO2. *Nano Letters* 2007, 7, 1643-1648.

236. Novoselov, K. S.; Geim, A. K.; Morozov, S. V.; Jiang, D.; Zhang, Y.; Dubonos, S. V.; Grigorieva, I. V.; Firsov, A. A., Electric field effect in atomically thin carbon films. *Science* 2004, 306, 666-669.

237. Novoselov, K. S.; Geim, A. K.; Morozov, S. V.; Jiang, D.; Katsnelson, M. I.; Grigorieva, I. V.; Dubonos, S. V.; Firsov, A. A., Two-dimensional gas of massless Dirac fermions in graphene. *Nature* 2005, 438, 197-200.

238. Zhang, Y. B.; Tan, Y. W.; Stormer, H. L.; Kim, P., Experimental observation of the quantum Hall effect and Berry's phase in graphene. *Nature* 2005, 438, 201-204.

239. Zhang, Y. B.; Small, J. P.; Amori, M. E. S.; Kim, P., Electric field modulation of galvanomagnetic properties of mesoscopic graphite. *Physical Review Letters* 2005, 94.

240. Berger, C.; Song, Z. M.; Li, T. B.; Li, X. B.; Ogbazghi, A. Y.; Feng, R.; Dai, Z. T.; Marchenkov, A. N.; Conrad, E. H.; First, P. N.; de Heer, W. A., Ultrathin epitaxial graphite: 2D electron gas properties and a route toward graphene-based nanoelectronics. *Journal of Physical Chemistry B* 2004, 108, 19912-19916.

241. Yang, N. L.; Zhai, J.; Wang, D.; Chen, Y. S.; Jiang, L., Two-Dimensional Graphene Bridges Enhanced Photoinduced Charge Transport in Dye-Sensitized Solar Cells. *Acs Nano* 2010, 4, 887-894.

242. Dikin, D. A.; Stankovich, S.; Zimney, E. J.; Piner, R. D.; Dommett, G. H. B.; Evmenenko, G.; Nguyen, S. T.; Ruoff, R. S., Preparation and characterization of graphene oxide paper. *Nature* 2007, 448, 457-460.

243. Stankovich, S.; Dikin, D. A.; Dommett, G. H. B.; Kohlhaas, K. M.; Zimney, E. J.; Stach, E. A.; Piner, R. D.; Nguyen, S. T.; Ruoff, R. S., Graphene-based composite materials. *Nature* 2006, 442, 282-286.

244. Nair, R. R.; Blake, P.; Grigorenko, A. N.; Novoselov, K. S.; Booth, T. J.; Stauber, T.; Peres, N. M. R.; Geim, A. K., Fine structure constant defines visual transparency of graphene. *Science* 2008, 320, 1308-1308.

245. Wang, W. D.; Serp, P.; Kalck, P.; Faria, J. L., Visible light photodegradation of phenol on MWNT-TiO2 composite catalysts prepared by a modified sol-gel method. *Journal of Molecular Catalysis a-Chemical* 2005, 235, 194-199.

246. Lin, J.; Zong, R. L.; Zhou, M.; Zhu, Y. F., Photoelectric catalytic degradation of methylene blue by C(60)-modified TiO(2) nanotube array. *Applied Catalysis B-Environmental* 2009, 89, 425-431.

247. Kamat, P. V., Meeting the clean energy demand: Nanostructure architectures for solar energy conversion. *Journal of Physical Chemistry C* 2007, 111, 2834-2860.

248. Mohapatra, S. K.; Misra, M.; Mahajan, V. K.; Raja, K. S., Design of a highly efficient photoelectrolytic cell for hydrogen generation by water splitting: Application of TiO(2-)xC(x) nanotubes as a photoanode and Pt/TiO2 nanotubes as a cathode. *Journal of Physical Chemistry C* 2007, 111, 8677-8685.

249. Murphy, A. B., Does carbon doping of TiO2 allow water splitting in visible light? Comments on "Nanotube enhanced photoresponse of carbon

modified (CM)-n-TiO2 for efficient water splitting". *Solar Energy Materials and Solar Cells* 2008, 92, 363-367.

250. Park, J. H.; Kim, S.; Bard, A. J., Novel carbon-doped TiO2 nanotube arrays with high aspect ratios for efficient solar water splitting. *Nano Letters* 2006, 6, 24-28.

251. Xu, C. K.; Shaban, Y. A.; Ingler, W. B.; Khan, S. U. M., Nanotube enhanced photoresponse of carbon modified (CM)-n-TiO2 for efficient water splitting. *Solar Energy Materials and Solar Cells* 2007, 91, 938-943.

252. Kuo, C. S.; Tseng, Y. H.; Huang, C. H.; Li, Y. Y., Carbon-containing nano-titania prepared by chemical vapor deposition and its visible-light-responsive photocatalytic activity. *Journal of Molecular Catalysis a-Chemical* 2007, 270, 93-100.

253. Xia, X. H.; Jia, Z. H.; Yu, Y.; Liang, Y.; Wang, Z.; Ma, L. L., Preparation of multi-walled carbon nanotube supported TiO2 and its photocatalytic activity in the reduction of CO2 with H2O. *Carbon* 2007, 45, 717-721.

254. Yamashita, H.; Fujii, Y.; Ichihashi, Y.; Zhang, S. G.; Ikeue, K.; Park, D. R.; Koyano, K.; Tatsumi, T.; Anpo, M., Selective formation of CH3OH in the photocatalytic reduction of CO2 with H2O on titanium oxides highly dispersed within zeolites and mesoporous molecular sieves. *Catalysis Today* 1998, 45, 221-227.

255. Yamashita, H.; Shiga, A.; Kawasaki, S.; Ichihashi, Y.; Ehara, S.; Anpo, M., PHOTOCATALYTIC SYNTHESIS OF CH4 AND CH3OH FROM CO2 AND H2O ON HIGHLY DISPERSED ACTIVE TITANIUM-OXIDE CATALYSTS. *Energy Conversion and Management* 1995, 36, 617-620.

256. Anpo, M.; Yamashita, H.; Ichihashi, Y.; Ehara, S., PHOTOCATALYTIC REDUCTION OF CO2 WITH H2O ON VARIOUS TITANIUM-OXIDE CATALYSTS. *Journal of Electroanalytical Chemistry* 1995, 396, 21-26.

257. Anpo, M.; Yamashita, H.; Ikeue, K.; Fujii, Y.; Zhang, S. G.; Ichihashi, Y.; Park, D. R.; Suzuki, Y.; Koyano, K.; Tatsumi, T., Photocatalytic reduction of CO2 with H2O on Ti-MCM-41 and Ti-MCM-48 mesoporous zeolite catalysts. *Catalysis Today* 1998, 44, 327-332.

258. Keita, I.; Nozaki, S.; Ogawa, M.; Anpo, M., Characterization of self-standing Ti-containing porous silica thin films and their reactivity for the photocatalytic reduction of CO2 with H2O. *Catalysis Today* 2002, 74, 241-248.

259. Wu, J. C. S.; Lin, H. M.; Lai, C. L., Photo reduction of CO2 to methanol using optical-fiber photoreactor. *Applied Catalysis a-General* 2005, 296, 194-200.

260. Nguyen, T. V.; Wu, J. C. S., Photoreduction of CO2 in an optical-fiber photoreactor: Effects of metals addition and catalyst carrier. *Applied Catalysis a-General* 2008, 335, 112-120.

261. Vijayan, B.; Dimitrijevic, N. M.; Rajh, T.; Gray, K., Effect of Calcination Temperature on the Photocatalytic Reduction and Oxidation Processes of Hydrothermally Synthesized Titania Nanotubes. *Journal of Physical Chemistry C* 2010, 114, 12994-13002.

262. Liang, Y. T.; Vijayan, B. K.; Gray, K. A.; Hersam, M. C., Minimizing Graphene Defects Enhances Titania Nanocomposite-Based Photocatalytic Reduction of CO(2) for Improved Solar Fuel Production. *Nano Letters* 2011, 11, 2865-2870.

263. Chen, L.; Graham, M. E.; Li, G. H.; Gentner, D. R.; Dimitrijevic, N. M.; Gray, K. A., Photoreduction of CO2 by TiO2 nanocomposites synthesized through reactive direct current magnetron sputter deposition. *Thin Solid Films* 2009, 517, 5641-5645.

264. Sasirekha, N.; Basha, S. J. S.; Shanthi, K., Photocatalytic performance of Ru doped anatase mounted on silica for reduction of carbon dioxide. *Applied Catalysis B-Environmental* 2006, 62, 169-180.

265. Gao, T. T.; Andino, J. M.; Alvarez-Idaboy, J. R., Computational and experimental study of the interactions between ionic liquids and volatile organic compounds. *Physical Chemistry Chemical Physics* 2010, 12, 9830-9838.

266. Atkinson, R., GAS-PHASE TROPOSPHERIC CHEMISTRY OF ORGANIC-COMPOUNDS - A REVIEW. *Atmospheric Environment Part a-General Topics* 1990, 24, 1-41.

267. Malik, F.; Sajbidor, J.; Lesko, J.; Minarik, E., Investigation of the trans 2-hexenal content in leaves of grapevines during the vegetation period. *Vitis* 1996, 35, 129-132.

268. Hatanaka, A., THE BIOGENERATION OF GREEN ODOR BY GREEN LEAVES. *Phytochemistry* 1993, 34, 1201-1218.

269. Springett, M. B.; Williams, B. M.; Barnes, R. J., THE EFFECT OF PACKAGING CONDITIONS AND STORAGE TIME ON THE VOLATILE COMPOSITION OF ASSAM BLACK TEA LEAF. *Food Chemistry* 1994, 49, 393-398.

270. Wood, W. F.; Brandes, M. L.; Watson, R. L.; Jones, R. L.; Largent, D. L., TRANS-2-NONENAL, THE CUCUMBER ODOR OF MUSHROOMS. *Mycologia* 1994, 86, 561-563.

271. Jimenez, E.; Lanza, B.; Martinez, E.; Albaladejo, J., Daytime tropospheric loss of hexanal and trans-2-hexenal: OH kinetics and UV photolysis. *Atmospheric Chemistry and Physics* 2007, 7, 1565-1574.

272. Taylor, W. D.; Allston, T. D.; Moscato, M. J.; Fazekas, G. B.; Kozlowski, R.; Takacs, G. A., ATMOSPHERIC PHOTO-DISSOCIATION LIFETIMES FOR NITROMETHANE, METHYL NITRITE, AND METHYL NITRATE. *International Journal of Chemical Kinetics* 1980, 12, 231-240.

273. Orlando, J. J.; Tyndall, G. S., Mechanisms for the reactions of OH with two unsaturated aldehydes: Crotonaldehyde and acrolein. *Journal of Physical Chemistry A* 2002, 106, 12252-12259.

274. Prinn, R.; Cunnold, D.; Simmonds, P.; Alyea, F.; Boldi, R.; Crawford, A.; Fraser, P.; Gutzler, D.; Hartley, D.; Rosen, R.; Rasmussen, R., GLOBAL AVERAGE CONCENTRATION AND TREND FOR HYDROXYL RADICALS DEDUCED FROM ALE GAUGE TRICHLOROETHANE (METHYL CHLOROFORM) DATA FOR 1978-1990. *Journal of Geophysical Research-Atmospheres* 1992, 97, 2445-2461.

275. Rivera, L.; Izquierdo, D.; Garces, I.; Salinas, I.; Alonso, J.; Puyol, M., Simple dip-probe fluorescence setup sensor for in situ environmental determinations. *Sensors and Actuators B-Chemical* 2009, 137, 420-425.

276. Jurdak, R.; Nafaa, A.; Barbirato, A., Large Scale Environmental Monitoring through Integration of Sensor and Mesh Networks. *Sensors* 2008, 8, 7493-7517.

277. Bohnert, K.; Brandle, H.; Brunzel, M. G.; Gabus, P.; Guggenbach, P. In *Highly accurate fiber-optic DC current sensor for the electrowinning industry*, Ieee-Inst Electrical Electronics Engineers Inc: 2007; pp 180-187.

278. Rupp, S.; von Schickfus, M.; Hunklinger, S.; Eipel, H.; Priebe, A.; Enders, D.; Pucci, A., A shear horizontal surface acoustic wave sensor for the detection of antigen-antibody reactions for medical diagnosis. *Sensors and Actuators B-Chemical* 2008, 134, 225-229.

279. Evans, R. C.; Douglas, P.; Williams, J. A. G.; Rochester, D. L. In *A novel luminescence-based colorimetric oxygen sensor with a "traffic light" response*, Springer/Plenum Publishers: 2006; pp 201-206.

280. Petrova, S.; Kostov, Y.; Jeffris, K.; Rao, G., Optical ratiometric sensor for alcohol measurements. *Analytical Letters* 2007, 40, 715-727.

281. Dubas, S. T.; Iamsamai, C.; Potiyaraj, P., Optical alcohol sensor based on dye-Chitosan polyelectrolyte multilayers. *Sensors and Actuators B-Chemical* 2006, 113, 370-375.

282. Xu, X. M.; Li, C. Z.; Pei, K. M.; Zhao, K.; Zhao, Z. B. K.; Li, H. Y., Ionic liquids used as QCM coating materials for the detection of alcohols. *Sensors and Actuators B-Chemical* 2008, 134, 258-265.

283. Wei, D.; Ivaska, A., Applications of ionic liquids in electrochemical sensors. *Analytica Chimica Acta* 2008, 607, 126-135.

284. Pandey, S., Analytical applications of room-temperature ionic liquids: A review of recent efforts. *Analytica Chimica Acta* 2006, 556, 38-45.

285. Cole, A. C.; Jensen, J. L.; Ntai, I.; Tran, K. L. T.; Weaver, K. J.; Forbes, D. C.; Davis, J. H., Novel bronsted acidic ionic liquids and their use as dual solvent-catalysts. *Journal of the American Chemical Society* 2002, 124, 5962-5963.

286. Handy, S. T.; Okello, M., Homogeneous supported synthesis using ionic liquid supports: Tunable separation properties. *Journal of Organic Chemistry* 2005, 70, 2874-2877.

287. Fung, Y. S.; Zhu, D. R., Electrodeposited tin coating as negative electrode material for lithium-ion battery in room temperature molten salt. *Journal of the Electrochemical Society* 2002, 149, A319-A324.

288. Shobukawa, H.; Tokuda, H.; Susan, M. A. H.; Watanabe, M. In *Ion transport properties of lithium ionic liquids and their ion gels*, 2005; pp 3872-3877.

289. Sato, T.; Masuda, G.; Takagi, K., Electrochemical properties of novel ionic liquids for electric double layer capacitor applications. *Electrochimica Acta* 2004, 49, 3603-3611.

290. Noda, A.; Susan, A. B.; Kudo, K.; Mitsushima, S.; Hayamizu, K.; Watanabe, M., Bronsted acid-base ionic liquids as proton-conducting nonaqueous electrolytes. *Journal of Physical Chemistry B* 2003, 107, 4024-4033.

291. Kubo, W.; Kitamura, T.; Hanabusa, K.; Wada, Y.; Yanagida, S., Quasi-solid-state dye-sensitized solar cells using room temperature molten salts and a low molecular weight gelator. *Chemical Communications* 2002, 374-375.

292. Zhou, D. Z.; Spinks, G. M.; Wallace, G. G.; Tiyapiboonchaiya, C.; MacFarlane, D. R.; Forsyth, M.; Sun, J. Z. In *Solid state actuators based on polypyrrole and polymer-in-ionic liquid electrolytes*, 2003; pp 2355-2359.

293. Anderson, J. L.; Armstrong, D. W., High-stability ionic liquids. A new class of stationary phases for gas chromatography. *Analytical Chemistry* 2003, 75, 4851-4858.

294. Peng, J. F.; Liu, J. F.; Hu, X. L.; Jiang, G. B., Direct determination of chlorophenols in environmental water samples by hollow fiber supported ionic liquid membrane extraction coupled with high-performance liquid chromatography. *Journal of Chromatography A* 2007, 1139, 165-170.

295. Qi, S. D.; Cui, S. Y.; Cheng, Y. Q.; Chen, X. G.; Hu, Z. D., Rapid separation and determination of aconitine alkaloids in traditional Chinese herbs by capillary electrophoresis using 1-butyl-3-methylimidazoium-based ionic liquid as running electrolyte. *Biomedical Chromatography* 2006, 20, 294-300.

296. Tian, K.; Qi, S. D.; Cheng, Y. Q.; Chen, X. G.; Hu, Z. D., Separation and determination of lignans from seeds of Schisandra species by micellar electrokinetic capillary chromatography using ionic liquid as modifier. *Journal of Chromatography A* 2005, 1078, 181-187.

297. Baker, G. A.; Baker, S. N.; Pandey, S.; Bright, F. V., An analytical view of ionic liquids. *Analyst* 2005, 130, 800-808.

298. Liang, C. D.; Yuan, C. Y.; Warmack, R. J.; Barnes, C. E.; Dai, S., Ionic liquids: A new class of sensing materials for detection of organic vapors based on the use of a quartz crystal microbalance. *Analytical Chemistry* 2002, 74, 2172-2176.

299. Schafer, T.; Di Francesco, F.; Fuoco, R. In *Ionic liquids as selective depositions on quartz crystal microbalances for artificial olfactory systems- a feasibility study*, 2007; pp 52-56.

300. Lee, Y. G.; Chou, T. C. In *Ionic liquid ethanol sensor*, 2004; pp 33-40.

301. Seyama, M.; Iwasaki, Y.; Tate, A.; Sugimoto, I., Room-temperature ionic-liquid-incorporated plasma-deposited thin films for discriminative alcohol-vapor sensing. *Chemistry of Materials* 2006, 18, 2656-2662.

302. Liao, Q.; Hussey, C. L., Densities, viscosities, and conductivities of mixtures of benzene with the Lewis acidic aluminum chloride plus 1-methyl-3-ethylimidazolium chloride molten salt. *Journal of Chemical and Engineering Data* 1996, 41, 1126-1130.

303. Wasserscheid, P.; Keim, W., Ionic liquids - New "solutions" for transition metal catalysis. *Angewandte Chemie-International Edition* 2000, 39, 3773-3789.

304. Jin, X. X.; Yu, L.; Garcia, D.; Ren, R. X.; Zeng, X. Q., Ionic liquid high-temperature gas sensor array. *Analytical Chemistry* 2006, 78, 6980-6989.

305. Lynden-Bell, R. M.; Atamas, N. A.; Vasilyuk, A.; Hanke, C. G., Chemical potentials of water and organic solutes in imidazolium ionic liquids: a simulation study. *Molecular Physics* 2002, 100, 3225-3229.

306. Hanke, C. G.; Atamas, N. A.; Lynden-Bell, R. M., Solvation of small molecules in imidazolium ionic liquids: a simulation study. *Green Chemistry* 2002, 4, 107-111.

307. Lynden-Bell, R. M.; Del Popolo, M. G.; Youngs, T. G. A.; Kohanoff, J.; Hanke, C. G.; Harper, J. B.; Pinilla, C. C., Simulations of ionic liquids, solutions, and surfaces. *Accounts of Chemical Research* 2007, 40, 1138-1145.

308. Zhao, Y.; Schultz, N. E.; Truhlar, D. G., Design of density functionals by combining the method of constraint satisfaction with parametrization for thermochemistry, thermochemical kinetics, and noncovalent interactions. *Journal of Chemical Theory and Computation* 2006, 2, 364-382.

309. Chiappe, C.; Malvaldi, M.; Pomelli, C. S., Ionic liquids: Solvation ability and polarity. *Pure and Applied Chemistry* 2009, 81, 767-776.

310. Rudberg, J.; Foster, M., Adsorption of methanol on the MgO(100) surface: An infrared study at room temperature. *Journal of Physical Chemistry B* 2004, 108, 18311-18317.

311. Merrick, J. P.; Moran, D.; Radom, L., An evaluation of harmonic vibrational frequency scale factors. *Journal of Physical Chemistry A* 2007, 111, 11683-11700.

312. Galloway, J. N.; Likens, G. E.; Keene, W. C.; Miller, J. M., THE COMPOSITION OF PRECIPITATION IN REMOTE AREAS OF THE WORLD. *Journal of Geophysical Research-Oceans and Atmospheres* 1982, 87, 8771-8786.

313. Madronich, S.; Chatfield, R. B.; Calvert, J. G.; Moortgat, G. K.; Veyret, B.; Lesclaux, R., A PHOTOCHEMICAL ORIGIN OF ACETIC-ACID IN THE TROPOSPHERE. *Geophysical Research Letters* 1990, 17, 2361-2364.

314. Kawamura, K.; Ng, L. L.; Kaplan, I. R., DETERMINATION OF ORGANIC-ACIDS (C1-C10) IN THE ATMOSPHERE, MOTOR EXHAUSTS, AND ENGINE OILS. *Environmental Science & Technology* 1985, 19, 1082-1086.

315. Talbot, R. W.; Beecher, K. M.; Harriss, R. C.; Cofer, W. R., ATMOSPHERIC GEOCHEMISTRY OF FORMIC AND ACETIC-ACIDS AT A MID-LATITUDE TEMPERATE SITE. *Journal of Geophysical Research-Atmospheres* 1988, 93, 1638-1652.

316. Andreae, M. O.; Talbot, R. W.; Andreae, T. W.; Harriss, R. C., FORMIC AND ACETIC-ACID OVER THE CENTRAL AMAZON REGION, BRAZIL .1. DRY SEASON. *Journal of Geophysical Research-Atmospheres* 1988, 93, 1616-1624.

317. Orzechowska, G. E.; Paulson, S. E., Photochemical sources of organic acids. 1. Reaction of ozone with isoprene, propene, and 2-butenes under dry and humid conditions using SPME. *Journal of Physical Chemistry A* 2005, 109, 5358-5365.

318. Bohnert, K.; Brandle, H.; Brunzel, M. G.; Gabus, P.; Guggenbach, P., Highly accurate fiber-optic DC current sensor for the electrowinning industry. *IEEE Transactions on Industry Applications* 2007, 43, 180-187.

319. Evans, R. C.; Douglas, P.; Williams, J. A. G.; Rochester, D. L., A novel luminescence-based colorimetric oxygen sensor with a "traffic light" response. *Journal of Fluorescence* 2006, 16, 201-206.

320. Wilkins, K.; Larsen, K., VARIATION OF VOLATILE ORGANIC-COMPOUND PATTERNS OF MOLD SPECIES FROM DAMP BUILDINGS. *Chemosphere* 1995, 31, 3225-3236.

321. Goodrich, J. A.; Kugel, J. F., Rate constants for binding and dissociation. In *Binding and Kinetics for molecular biologists*, Cold Spring Habor: 2007; pp 69-97.

322. Goodrich, J. A.; Kugel, J. F., Equation Derivations, Appendix 1. In *Binding and Kinetics for molecular biologists*, Cold Spring Habor: 2007; pp 155-166.

323. Goodrich, J. A.; Kugel, J. F., Affinity constants. In *Binding and Kinetics for molecular biologists*, Cold Spring Habor: 2007; pp 19-33.

324. Frisch, M. J., Gaussian 03, Revision B-0.4. Gaussian, Inc., Pittsburgh PA.: 2003.

325. Myszka, D. *Scrubber 2*, 2.0a; University of Utah: 2005.

326. Linstrom, P. J.; Mallard, W. G.; Eds., NIST Chemistry WebBook, NIST Standard Reference Database Number 69, National Institute of Standards and Technology,Gaithersburg MD, 20899.

327. Ren, M. H.; Forzani, E. S.; Tao, N. J., Chemical sensor based on microfabricated wristwatch tuning forks. *Analytical Chemistry* 2005, 77, 2700-2707.

328. Goubaidoulline, I.; Vidrich, G.; Johannsmann, D., Organic vapor sensing with ionic liquids entrapped in alumina nanopores on quartz crystal resonators. *Analytical Chemistry* 2005, 77, 615-619.

329. Chrobok, A.; Baj, S.; Pudlo, W.; Jarzebski, A., Supported ionic liquid phase catalysis for aerobic oxidation of primary alcohols. *Applied Catalysis a-General* 2010, 389, 179-185.

330. Liu, L.; Ma, J. J.; Xia, J. Y.; Li, L. D.; Li, C. L.; Zhang, X. B.; Gong, J. Y.; Tong, Z. W., Confining task-specific ionic liquid in silica-gel matrix by sol-gel technique: A highly efficient catalyst for oxidation of alcohol with molecular oxygen. *Catalysis Communications* 2011, 12, 323-326.

331. Rodriguez-Perez, L.; Teuma, E.; Falqui, A.; Gomez, M.; Serp, P., Supported ionic liquid phase catalysis on functionalized carbon nanotubes. *Chemical Communications* 2008, 4201-4203.

332. Geim, A. K.; Novoselov, K. S., The rise of graphene. *Nature Materials* 2007, 6, 183-191.

333. Stankovich, S.; Dikin, D. A.; Piner, R. D.; Kohlhaas, K. A.; Kleinhammes, A.; Jia, Y.; Wu, Y.; Nguyen, S. T.; Ruoff, R. S., Synthesis of graphene-based nanosheets via chemical reduction of exfoliated graphite oxide. *Carbon* 2007, 45, 1558-1565.

334. He, H. Y.; Klinowski, J.; Forster, M.; Lerf, A., A new structural model for graphite oxide. *Chemical Physics Letters* 1998, 287, 53-56.

335. Lerf, A.; He, H. Y.; Forster, M.; Klinowski, J., Structure of graphite oxide revisited. *Journal of Physical Chemistry B* 1998, 102, 4477-4482.

336. Yang, H. F.; Shan, C. S.; Li, F. H.; Han, D. X.; Zhang, Q. X.; Niu, L., Covalent functionalization of polydisperse chemically-converted graphene sheets with amine-terminated ionic liquid. *Chemical Communications* 2009, 3880-3882.

337. Arunachalam, V. S.; Fleischer, E. L., The global energy landscape and materials innovation. *Mrs Bulletin* 2008, 33, 264-276.

338. Ramdin, M.; de Loos, T. W.; Vlugt, T. J. H., State-of-the-Art of CO2 Capture with Ionic Liquids. *Industrial & Engineering Chemistry Research* 2012, 51, 8149-8177.

339. Hummers, W. S.; Offeman, R. E., PREPARATION OF GRAPHITIC OXIDE. *Journal of the American Chemical Society* 1958, 80, 1339-1339.

340. Kovtyukhova, N. I.; Ollivier, P. J.; Martin, B. R.; Mallouk, T. E.; Chizhik, S. A.; Buzaneva, E. V.; Gorchinskiy, A. D., Layer-by-layer assembly of ultrathin composite films from micron-sized graphite oxide sheets and polycations. *Chemistry of Materials* 1999, 11, 771-778.

341. Zhang, Y. J.; Shen, Y. F.; Yuan, J. H.; Han, D. X.; Wang, Z. J.; Zhang, Q. X.; Niu, L., Design and synthesis of multifunctional materials based on an ionic-liquid backbone. *Angewandte Chemie-International Edition* 2006, 45, 5867-5870.

342. Shen, J. F.; Shi, M.; Yan, B.; Ma, H. W.; Li, N.; Ye, M. X., Ionic liquid-assisted one-step hydrothermal synthesis of TiO(2)-reduced graphene oxide composites. *Nano Research* 2011, 4, 795-806.

343. Dai, B. Y.; Fu, L.; Liao, L.; Liu, N.; Yan, K.; Chen, Y. S.; Liu, Z. F., High-Quality Single-Layer Graphene via Reparative Reduction of Graphene Oxide. *Nano Research* 2011, 4, 434-439.

344. Hurum, D. C.; Gray, K. A.; Rajh, T.; Thurnauer, M. C., Recombination pathways in the Degussa P25 formulation of TiO2: Surface versus lattice mechanisms. *Journal of Physical Chemistry B* 2005, 109, 977-980.

345. Hurum, D. C.; Agrios, A. G.; Crist, S. E.; Gray, K. A.; Rajh, T.; Thurnauer, M. C., Probing reaction mechanisms in mixed phase TiO2 by EPR. *Journal of Electron Spectroscopy and Related Phenomena* 2006, 150, 155-163.

346. Koci, K.; Obalova, L.; Matejova, L.; Placha, D.; Lacny, Z.; Jirkovsky, J.; Solcova, O., Effect of TiO2 particle size on the photocatalytic reduction of CO2. *Applied Catalysis B-Environmental* 2009, 89, 494-502.

347. Asahi, R.; Morikawa, T.; Ohwaki, T.; Aoki, K.; Taga, Y., Visible-light photocatalysis in nitrogen-doped titanium oxides. *Science* 2001, 293, 269-271.

348. Umebayashi, T.; Yamaki, T.; Itoh, H.; Asai, K., Band gap narrowing of titanium dioxide by sulfur doping. *Applied Physics Letters* 2002, 81, 454-456.

349. Yu, J. C.; Yu, J. G.; Ho, W. K.; Jiang, Z. T.; Zhang, L. Z., Effects of F-doping on the photocatalytic activity and microstructures of nanocrystalline TiO2 powders. *Chemistry of Materials* 2002, 14, 3808-3816.

350. In, S.; Orlov, A.; Berg, R.; Garcia, F.; Pedrosa-Jimenez, S.; Tikhov, M. S.; Wright, D. S.; Lambert, R. M., Effective visible light-activated B-Doped and B,N-Codoped TiO2 photocatalysts. *Journal of the American Chemical Society* 2007, 129, 13790-+.

351. He, Z. Q.; Xu, X.; Song, S.; Xie, L.; Tu, J. J.; Chen, J. M.; Yan, B., A Visible Light-Driven Titanium Dioxide Photocatalyst Codoped with Lanthanum and Iodine: An Application in the Degradation of Oxalic Acid. *Journal of Physical Chemistry C* 2008, 112, 16431-16437.

352. Hong, X. T.; Wang, Z. P.; Cai, W. M.; Lu, F.; Zhang, J.; Yang, Y. Z.; Ma, N.; Liu, Y. J., Visible-light-activated nanoparticle photocatalyst of iodine-doped titanium dioxide. *Chemistry of Materials* 2005, 17, 1548-1552.

353. Liu, G.; Sun, C. H.; Yan, X. X.; Cheng, L.; Chen, Z. G.; Wang, X. W.; Wang, L. Z.; Smith, S. C.; Lu, G. Q.; Cheng, H. M., Iodine doped anatase TiO(2) photocatalyst with ultra-long visible light response: correlation between geometric/electronic structures and mechanisms. *Journal of Materials Chemistry* 2009, 19, 2822-2829.

354. Su, W. Y.; Zhang, Y. F.; Li, Z. H.; Wu, L.; Wang, X. X.; Li, J. Q.; Fu, X. Z., Multivalency iodine doped TiO2: Preparation, characterization, theoretical studies, and visible-light photocatalysis. *Langmuir* 2008, 24, 3422-3428.

355. Tojo, S.; Tachikawa, T.; Fujitsuka, M.; Majima, T., Iodine-doped TiO2 photocatalysts: Correlation between band structure and mechanism. *Journal of Physical Chemistry C* 2008, 112, 14948-14954.

# APPENDIX A

# SUPPLEMENTAL FIGURES AND TABLES

Figure A-1 are the computational results of optimized $C_4$mimCl molecule interacted with different VOCs, including methanol, ethanol, formaldehyde, ethane and ethylene. The shortest interaction lengths were identified for each interaction. It indicates the possible interaction positions.

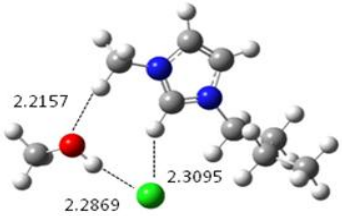


(a)

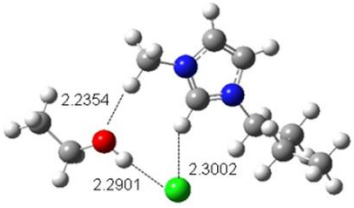


(b)

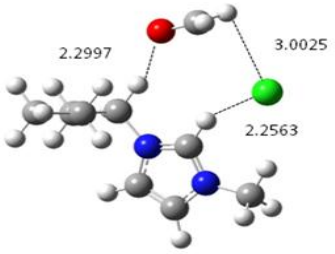


(c)

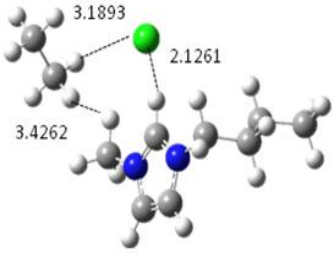


(d)

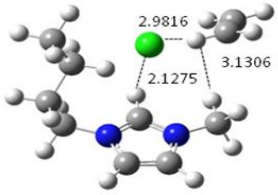


(e)

Figure A-1. Optimized geometries, including interaction lengths ( in Å) of $C_4$mimCl and different types of VOCs. (a) Optimized geometry of $C_4$mimCl and methanol. (b) Optimized geometry of $C_4$mimCl and ethanol. (c) Optimized geometry of $C_4$mimCl and formaldehyde. (d) Optimized geometry of $C_4$mimCl and ethane. (e) Optimized geometry of $C_4$mimCl and ethylene. The numbers represent the interaction lengths in units of Angstroms.

Table A-1 summarized the possible interaction positions and the interaction lengths for the interactions between $C_4$mimCl and VOCs studied in the computational work in Chapter 3. By comparing the interaction lengths, the interactions between $C_4$mimCl and alcohols have the least interaction lengths among the interactions of $C_4$mimCl with alcohols, aldehydes, ketone, alkanes, alkye, alkenes and aromatic compounds. Table A-1 indicates that $C_4$mimCl is more likely to interact with alcohols as compared to other classes of VOCs.

Table A-1. Interaction Lengths between $C_4$mimCl and Different VOCs Using the Hartree-Fock Calculations

| **Interacting compounds** | **Interaction lengths at different positions,Å** | | | |
|---|---|---|---|---|
| | **H•••Cl[a]** | **O•••H[a]** | **H•••H[a]** | **C•••H[a]** |
| methanol + $C_4$mimCl | 2.2869 | 2.2157 | b | b |
| ethanol + $C_4$mimCl | 2.2901 | 2.2354 | b | b |
| isopropanol + $C_4$mimCl | 2.3186 | 2.2166 | b | b |
| 2-methyl-1-propanol + $C_4$mimCl | 2.2847 | 2.2153 | b | b |
| 3-methyl-1-butanol + $C_4$mimCl | 2.2950 | 2.2184 | b | b |
| formaldehyde + $C_4$mimCl | 3.0025 | 2.2997 | b | b |
| acetaldehyde + $C_4$mimCl | 2.6316 | 2.3003 | b | b |
| butanal + $C_4$mimCl | 3.0078 | 2.2428 | b | b |
| acetone + $C_4$mimCl | 2.9246 | 2.2930 | b | b |
| ethane + $C_4$mimCl | 3.1893 | NA[c] | 3.4262 [b] | b |
| propane + $C_4$mimCl | 3.2544 | NA[c] | 3.2426 [b] | b |
| ethylene + $C_4$mimCl | 2.9816 | NA[c] | 3.1306 [b] | b |
| *cis*-2-butene + $C_4$mimCl | 3.2179 | NA[c] | 3.2270 [b] | b |
| acetylene + $C_4$mimCl | 2.5978 | NA[c] | 2.7916 [b] | b |
| toluene + $C_4$mimCl | 3.0425 | NA[c] | b | 2.9234 |

[a] The first atom represents the atom in the VOC while the second atom represents the atom in $C_4$mimCl.

[b] These calculated interactions are not significant (since they are larger) as compared to the other interaction lengths listed in the Table. The numbers presented are the shortest interaction lengths. However, these lengths are still quite large as compared to those of the oxygenated compounds..

[c] Not available since there is no oxygen atom in alkanes, alkenes, alkynes, or aromatic hydrocarbon.

Figure A-2 and A-3 show the molecular structure of methanol interaction with different ionic liquids (A-2) $C_4$mimBr and (A-3) $C_4$mim$BF_4$ after computational optimizations. The possible interaction positions and the interaction lengths are presented in the Figures.

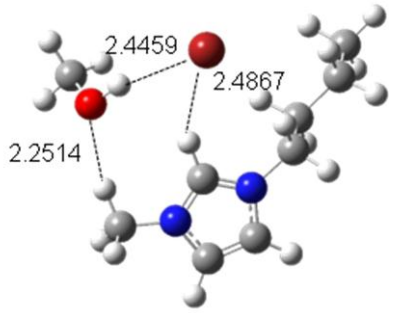


Figure A-2. Optimized geometry of $C_4$mimBr and methanol. The numbers represent the interaction lengths in units of Angstroms.

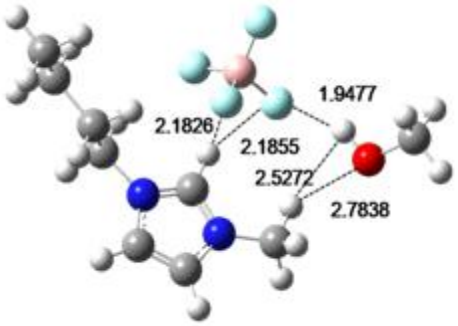


Figure A-3. Optimized geometry of $C_4$mim$BF_4$ and methanol. The numbers represent the interaction lengths in units of Angstroms.

Table A-2 summarizes the interaction positions and interaction lengths of the interactions between methanol and different ionic liquids studied in Chapter 3. The interaction lengths for methanol + $C_4$mimCl are smaller than those for the interaction between methanol and $C_4$mimBr. However, only based on the comparison of the interaction lengths, no conclusion can be made to predict whether the interaction of methanol with $C_4$mimCl is more favorable than the interaction of methanol with $C_4$mim$BF_4$ since the interaction between methanol and $C_4$mim$BF_4$ has a shorter interaction length for H-Halogen atom interaction and at the same time it has longer interaction length for O-H interaction. The additinal thermochemical data from the computational study presented in Chapter 3 helps to make the prediction that the interaction between methanol and $C_4$mimCl is more favorable. The shorter H-F interaction lengh may be due to the smaller diameter of F atom as compared to Cl atom.

Table A-2. Interaction Atoms and Lengths for Methanol with Different Types of Ionic Liquids

| **Interaction compounds** | **Interaction lengths** | |
|---|---|---|
| | **H••• Halogen atom [a,b]** | **O•••H [b]** |
| methanol + $C_4$mimCl | 2.2869 | 2.2157 |
| methanol + $C_4$mimBr | 2.4459 | 2.2514 |
| methanol + $C_4$mim$BF_4$ | 1.9477 | 2.7838 |

a. Halogen atom represents Cl, Br and F in $C_4$mimCl, $C_4$mimBr and $C_4$mim$BF_4$, respectively.

b. The first atom represents the atom in methanol while the second atom represents the atom in the ionic liquid.

Table A-3 presents the calculations for the increase of carbon content of the ionic liquid-reduced graphite oxide (IL-RGO) from graphite oxide (GO) by simply attaching the $NH_2$ terminated ionic liquid but without reducing oxygen. This information was used to compare with the percentage of carbon in the synthesized GO and that in the IL-RGO obtained from the XPS data in Chapter 5 to demonstrate whether GO was indeed reduced.

Table A-3. The Calculations of Carbon Content added to the RGO Surface by Simply Attaching the Ionic Liquid

| | **C-N**[a] | **C atom** |
|---|---|---|
| Number in 1 molecule of attached ionic liquid | 3 | 7 |
| Percentage in XPS data of the IL-RGO | 2.6% | 6.1% |

[a.] C-N only considers N bonded with C, which is not in the ring structure.

Figure A-4 shows the IR spectrum of pure $CH_4$ and $H_2O$ vapor over IL-RGO/$TiO_2$ catalyst. The IR spectrum of IL-RGO/$TiO_2$ catalyst is the background spectrum. The IR features of $CH_4$ in this spectrum were used to compare with the IR features of the product of the $CO_2$ photoreduction using IL-RGO/$TiO_2$ catalyst In the presence of $H_2O$ vapor. It confirms that the product is $CH_4$.

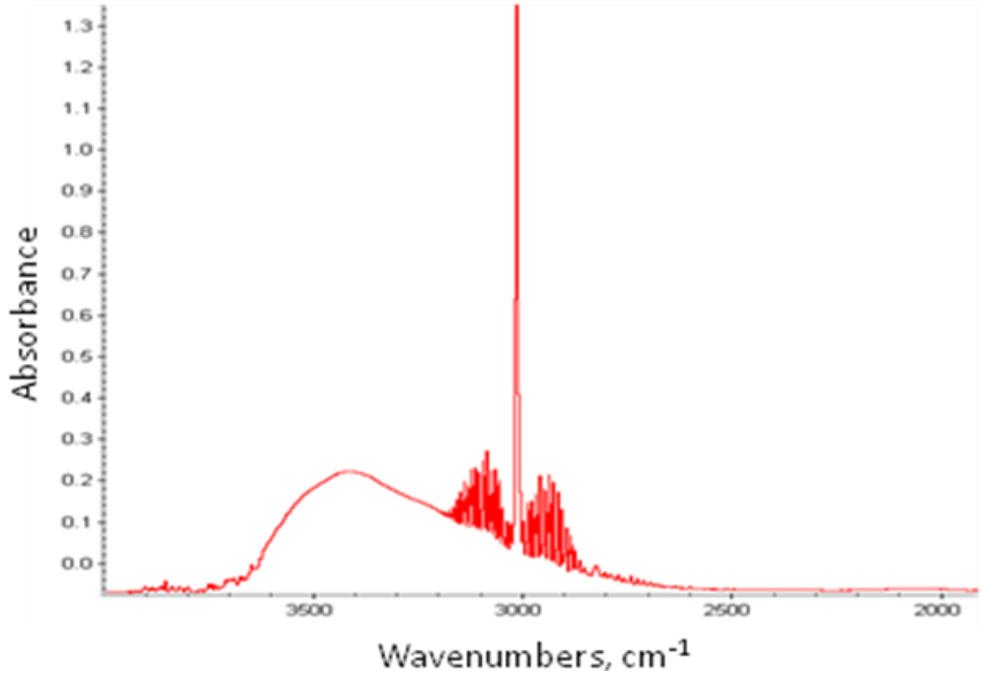


Figure A-4. The IR spectrum of pure $CH_4$ and $H_2O$ vapor over IL-RGO/$TiO_2$ sample.

Figure A-5 shows the calibration curve of $CH_4$ over IL-RGO/$TiO_2$ sample in Chapter 5. Different concentrations of $CH_4$ were obtained by mixing different flow rates of pure $N_2$ and pure $CH_4$. The IL-RGO/$TiO_2$ sample was exposed to different concentrations of $CH_4$. For each concentration, several IR spectra were obtained until a steady state of absorption of $CH_4$ to the catalyst was achieved. The absolute peak height of $CH_4$ in absorbance under steady state was obtained. Subsequently, pure $N_2$ was admitted to the reaction chamber. The dissociation of $CH_4$ from the catalyst started. When the IR spectrum showed that $CH_4$ was completely dissociated from the catalyst surface, another concentration of $CH_4$ was admitted to the reaction chamber. The peak height of $CH_4$ in absorbance for each concentration of $CH_4$ was obtained.

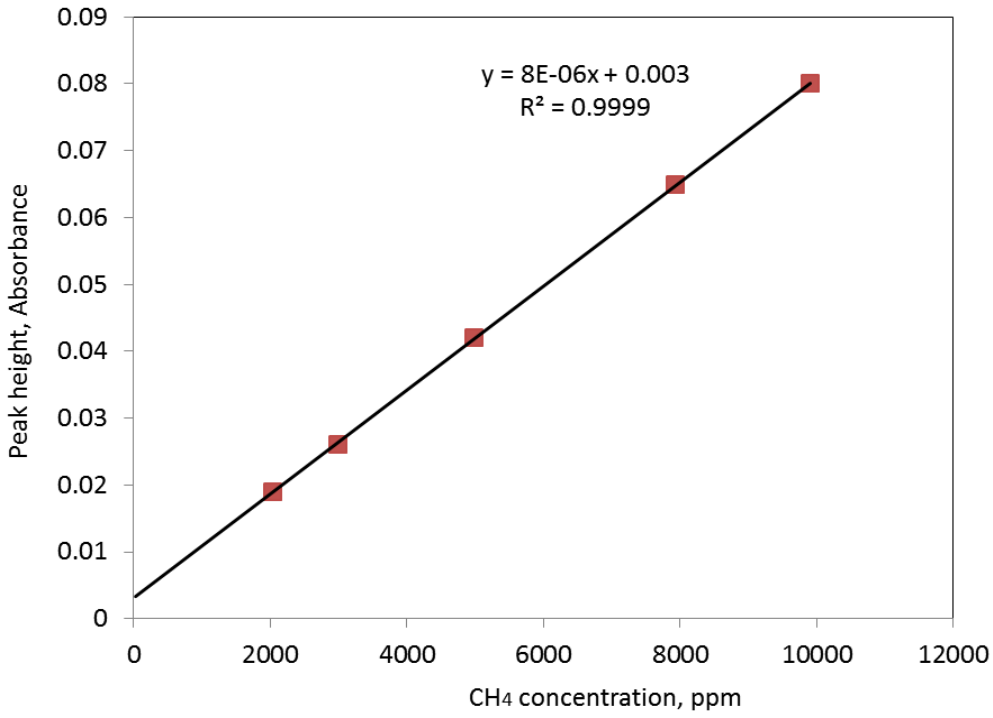


Figure A-5. Calibration curve of $CH_4$ over IL-RGO/$TiO_2$ catalyst.

Table A-4 presents the parameter values used for $CH_4$ production rate calculations in Chapter 5. The calculation details are shown in the equations following Tale A-4.

Table A-4. The Parameter Values Used in $CH_4$ Production Rate Calculations

| **Parameter** | **Value** |
|---|---|
| The concentration of $CH_4$ at 55 minute (t=0.92 minutes) UV-Visible irradiation | 11025 $ppm_v$ |
| Volume of the chamber, V | 17 mL |
| Mass of the IL-RGO/$TiO_2$ catalyst, m | 0.03 g |
| Pressure, P | 1 atm |
| Temperature, T | 298 K |
| Ideal gas constant, R | 0.082 L atm $K^{-1}mol^{-1}$ |

Calculations:

Volume of $CH_4$ at 55 minute UV-Visible irradiation=11025 $ppm_v \times 17$ mL=$1.87 \times 10^{-4}$ L.

PV=nRT

n=PV/RT=1 atm $\times 1.87 \times 10^{-4}$ L /(0.082 L atm $K^{-1}mol^{-1}$ $\times$ 298 K)= 7.7 $\times^{10\text{-}6}$ mol= 7.7 μmol.

$CH_4$ production rate=n/(m × t)= 7.7 μmol/(0.03g ×0.92 min)=279 μmol/g catalyst-hr.